HU ISSN 2063-6997

GEOSCIENCES AND ENGINEERING

A Publication of the University of Miskolc

Volume 12, Number 2 (2024)

Miskolc, University Press

GEOSCIENCES AND ENGINEERING
A Publication of the University of Miskolc
Volume 12, Number 2
Miskolc, University Press
UNIVERSITY OF MISKOLC
FACULTY OF EARTH AND ENVIRONMENTAL SCIENCES & ENGINEERING
HU ISSN 2063-6997

TABLE OF CONTENTS

Geosciences and Engineering, Vol. 12, No. 2 (2024), pp. 5–24.
https://doi.org/10.33030/geosciences.2024.02.001

SYMBOLS USED ON ETHNIC MAPS IN THE EARLY DECADES OF THE 20TH CENTURY

JÁNOS JENEY[1]*, KÁROLY KOCSIS[2]
[1]**Institute of Hungarian Research; jeney.janos@mki.gov.hu*
[2]*Institute of Geography and Geoinformatics, MFK, University of Miskolc*
karoly.kocsis@uni-miskolc.hu
[2]*Geographical Institute, CSFK, HUN-REN; kocsis.karoly@csfk.org*
[1]*https://orcid.org/0000-0003-0205-6756*
[2]*https://orcid.org/0009-0003-5212-4670*

Abstract: While most maps are a representation of the surface of the earth at a reduced scale, some maps known as thematic maps are a representation of data distributed on the face of the earth. Within thematic maps, ethnic maps make up a special group since they have played a large role in defining state borders, especially during and after the First World War when territorial demands were made which were justified using ethnic maps. Many different mapping methods have been tried and while many can give a very accurate picture their interpretation is time-consuming hence they cannot be presented to decision-makers. This paper presents those mapping methods together with their scale which are ideal to be used for decisions on borders and analyzes their accuracy.

Keywords: *ethnic maps, population mapping, qualitative data, quantitative data, mapping methods, objective depiction*

1. INTRODUCTION

A map is a representation of the surface of the earth or of data distributed on the surface using a predefined symbology at a constant scale. The amount of information a map can hold is limited (Klinghammer & Papp-Váry, 1983). While a topographic map is made with the purpose of representing the surface of the Earth, thematic maps are "not exclusively topographic, but represent on a topographic, hydrographic choreographic or geographic base localizable phenomena of any nature" (Cauvin et al., 2010a). Within the group of thematic maps the sub-group of ethnic maps show the ethnic affiliation (mother tongue) of the population. Generalization on any thematic map is challenging since it affects both the topographic data and the thematic data. Generalizing on ethnic maps is even more challenging due to the fact that to convey an accurate picture one does not only have to present qualitative data about the population (in this case ethnic affiliation) but also quantitative information (the number of inhabitants). Two maps using the same mapping method allows comparison of the statistics used to create the map while comparing maps made using the same statistical data allows analyses and comparisons to be performed on the mapping methods. One example is if the map shows the number of inhabitants one can get a more accurate picture of the

ethnic structure of the area than if it does not. In the first part of this study the reasons for and the consequences of showing or not showing the number of inhabitants is discussed. The use of different map symbols is also discussed as these are the basis of giving the map user an accurate picture. In the second part examples of maps are presented showing why these are important in practice. The maps used in the examples are maps used in the peace talks ending the Great War, where the time needed to interpret the maps was an important factor. Interpreting large scale maps (scale above 1 : 1 000 000 for the Carpathian Basin) is very time consuming making such maps unusable at the peace conference.

Maps can be seen as a form of graphical communication medium where the information communicated is not restricted to topographical information but can be anything having a special factor. Maps show a picture of reality that is reduced in size when compared to the earth's surface making generalization necessary which, under all circumstances, causes loss of information. The loss of information caused by generalization does not only happen with regards to topographic data but also with regards to the thematic data displayed on it. This data can be qualitative or quantitative, and while in both cases this can be a factor, the problem in general is much greater in the case of qualitative data.

Maps use symbols to depict geographic objects or, in the case of thematic maps, the geographical distribution of information in a certain data set. This can be anything from air pressure to temperature or any information gathered about the population be that quantitative (number of inhabitants, density of the population), or qualitative (ethnic affiliation, religion, age, ability to read and write, etc.). Symbols can be colored geometric shapes, pictograms, or simply just colored surfaces. The characteristics of the symbols can convey either qualitative or quantitative information to the reader. In order to convey both at least two characteristics need to be defined. Depending on the symbol these can be shape, size, color or shade (Klinghammer & Török, 1995). Ethnic maps usually use colored surfaces as symbols representing ethnic groups.

This study was done through analyzing maps that were used during the Paris Peace Conference in 1919 ending the First World War. This analysis could be done on any set of maps but due to the sensitivity of ethnic mapping and the availability of ethnic maps it is easier to show the differences between the different mapping methods. The maps selected all depict areas of the Carpathian Basin with some maps also depicting neighboring regions; however on these maps only the areas in the Carpathian Basin were considered. In the first part of the study the criteria for mapping ethnic groups in an objective manner are set. This was derived from the analysis of the maps which are presented in the second part of the study. The order of the two parts was selected to make the study easier to understand so that the reader understands the basic concepts before introducing results derived from the studied maps. The main source of information for this study are the maps cited in the study. In order to be able to analyze the maps it is important that we have an understanding about the basic concepts of ethnic cartography. It is important to understand what criteria the mapping methods used have to fulfill, what strengths and weaknesses a given mapping method has, and do certain

methods over- or under-represent minorities. One must also investigate if certain methods depict small minorities at all, and which ones over- or under-represent the minorities or the majorities (Jordan, 1999). The most important question is if the method used on a given map give an accurate picture of the full ethnic structure of the area.

The effects of using different colors are not discussed in this study. The sensitivity of the human eye to various colors is known (most sensitive to red, followed by green, yellow, blue and purple) but no data is available on the ranking of the aforementioned colors as to how they attract the eye when presented together (Robinson, 1967). However, the distinction the colors given to the different surfaces is much more important than to which extent they attract the eye. The mapping method used can distort the picture to a far greater extent than the colors used. By studying a given map for some time, the eye will get used to the composition and the possible distortion caused by the colors can be mitigated. If the mapping method however communicates false data, the distortion caused by the colors cannot be mitigated.

While it is important to note that ethnic maps are thematic maps and the same concepts should be applied to them as to other thematic maps so that the data is depicted in an objective manner; however when these maps were made the making of the maps had a political motive. At the end of the Great War these maps were intended to influence decision makers who were redrawing the borders within Europe. Every mapmaker chose mapping methods according to their own interest, often using mapping methods that could create a very distorted picture form even the most accurate data.

2. BASIC CONCEPTS OF ETHNIC MAPPING

Usually thematic maps present single characteristics of a certain data set (Muehrcke, 1972) which in the case of ethnic maps means that they show qualitative data – the ethnic affiliation of the population. In twentieth century, Europe the practice was to derive ethnic affiliation from the mother tongue of the population. This means that these maps are in actual fact not really ethnic maps, but maps showing mother tongue of the population. Today there would be much larger differences between the two types of data than there were back then. Usually the primary language spoken at home was considered the mother tongue of any given person (Kocsis, 1989). While depicting the population according to mother tongue seems straight forward one has to keep in mind that the geographical distribution of the population is not homogeneous and if one only shows the qualitative data on the map (ethnic affiliation or mother tongue of the population) then we will get a picture of the dominant language spoken in a given area, but we will not have an idea of the number of people living there. Since all areas, including uninhabited ones, belong to one or another municipality it may occur that the entire area of a municipality will seem to be inhabited by the majority ethnic group giving the impression that large uninhabited areas are in fact inhabited. This distorts the picture of the ethnic landscape of the depicted area since the map communicates a picture that would be true if the population would be homogeneous, and no uninhabited areas would exist. While this problem exists in all territories the inequality in the density of the population is far greater in mountainous areas. This means that while the ethnic affiliation of the population is qualitative

information, quantitative information needs to be displayed on the map in order to get an accurate picture of the ethnic landscape of the depicted area.

On maps showing the density of the population only quantitative information is shown. This can either be the number of inhabitants, or the map can also show the ratio of people per square kilometer in an area. However, since no qualitative information is shown, all characteristics of the symbols can be used to depict this information: color (or pattern), size, and/or shade. In theory is true the use of color is selective, separative, and associative thus it should only be used to depict qualitative information (Cauvin et al., 2010a). When used to depict population density the reader might assume qualitative data on the map while in actual fact it is not present and could be misled reading the map. This means that usually one would use a choropleth to depict data with value per unit area (Muehrcke, 1972) which is the type of data we have when depicting population density. In this case different shades of the same color can be used. In general, the more intense the color of the symbol the greater its value (Robinson, 1967). This in practice means that the darker the shade the greater the density of the population in the areas.

If qualitative information is shown (in this case the ethnic affiliation of the population) one of the symbol's characteristics must be used to depict this information. Since the size and shade of the symbol is more suited for depicting quantitative information the color or pattern of the symbol's surface needs to be used to depict qualitative information (ethnic affiliation). If the symbol uses colors, using patterns in general should be avoided unless two categories of information are closely related. In such cases using two different patterns of the same or similar color can help to group these categories. This does however have the effect that the map reader automatically groups these categories and if the color used by the two symbols is the same the map reader can even join these categories. Patterns should by no means be used for displaying any unrelated data if colors are used as this could make the map unreadable. Using colors or patterns for displaying quantitative data on maps where no other data is shown can make the map hard to read, but if qualitative data is also shown the map would become unreadable. This means that quantitative data should be shown by using shade or size. If the map uses colored symbols, then using more than two shades of a particular color will also make the map unreadable since someone who is not trained in this area cannot distinguish too many shades. This is reduced even further by variations in its surroundings making the connection between map legend and features on the map difficult or even impossible (Robinson, 1967). Furthermore, certain shades are often interpreted by humans as a different color. For example, a light shade of red is pink, a light shade of black is gray. These are often used on maps as another color, making this method unusable to show the density of the population on maps showing ethnic affiliation.

As a conclusion to the above one can state that if a map is made in such a way that both ethnic affiliation and population density is shown on a map it is best to depict the ethnic affiliation using the color or pattern of the symbol while the density of the population or number of inhabitants is to be shown by the size of the symbol. This might seem at first glance to have solved the problem, one must still make a

map that is easy to read by the map reader in practice. If symbols cover each other, which can easily happen, the map becomes unreadable. It is also very important that the map reader should see the picture in a spatial context, meaning that the frame given by the map projection should not be distorted beyond the point that the true geographical distribution of the population is not recognizable. This means that using traditional cartograms should be avoided since these tend to create such large distortions that in smaller regions the geographical area becomes unrecognizable in absence of major features (e.g. coastlines).

Another important question is the area represented by a given symbol. If the area is too large, the map becomes overgeneralized and this causes large data loss. When looking at the map the pattern that would otherwise appear, which in this case would show minorities, becomes smoothed due to the data loss. This procedure is very similar to smoothing of quantitative data which might not result in serious data loss if the general tendencies are visible on the map. When discrete values are smoothed the result becomes unscientific since the picture conveyed to the map reader will be a false one (Robinson, 1961). For this reason, population maps are usually not made using an isarithmic surface. In the case of qualitative data on ethnic maps (ethnic affiliation) the values are always discrete thus this kind of smoothing should be avoided. One very extreme example of when an area represented by a symbol is too large was the map made by the Romanian statistical bureau depicting the results of the 1930 census of Romania. The colored surface shows the majority population of the county. In Mureş county (Judeţs Mureş) the Romanians made up 45.8% of the population and Hungarians made up 42.6%. The rest of the population is represented by other ethnic groups. The whole county is colored purple showing that the majority of the population is Romanian and a yellow rhombus is placed in the map to show that the greatest minority are the Hungarians. This is severely misleading. The result is that it is incorrect for one symbol to represent such a large area unless the symbol reveals the true ethnic structure of the population which in this case it does not (Krallert, 1961). In fact, according to the publication made by the Institute of Political Sciences in Hungary (Államtudományi Intézet) if the Romanian author would have used a less distorted source for his statistics the whole county would have been colored Hungarian on that map (Staatwissenshcaftliches Institut, 1942). Another map is provided using pie charts and provides more accurate data, but pie charts are much more difficult to read than colored surfaces. If the area represented by the symbol is too small, it will not be visible on the map. The question of what is too large and what is too small is determined by the scale of the map, since the smaller the scale, the smaller the area on the map that represents a given area on the surface. This type of overgeneralization is very common on ethnic maps. In many cases this happens in such a way that the base map is far less generalized than the thematic contents. In thematic cartography a very basic concept is that the base map needs to be heavily generalized since its sole purpose is for the map reader to be able to place the data into a geographical context while being able to see the detailed thematic data without disturbance (Klinghammer & Papp-Váry, 1991). If the base map is not generalized to the extent of only having the minimal contents the map can become illegible. If

one generalizes the thematic contents instead, then the contents the map needs to communicate to the user becomes extremely distorted usually in a way that it homogenizes the picture of the thematic contents, in this case the ethnic affiliation of the population. This is a huge error since the map reader gets a false picture of the ethnic structure of the population.

The last theoretical problem is defining the categories or classes of qualitative and quantitative data on the map. This form of generalizing is done by generalizing the thematic variable and not the geometry (Cauvin et al., 2010b). This at first seems straight forward since these categories are defined by the statistics provided. Since the cartographer's job is not to collect or analyze the statistics in detail but to depict them as objectively as possible one can say that this does not have any relevance. However, one can see from the above that the map reader cannot distinguish an infinite number of colors and thus it can be a problem if the statistics define too many categories in a small area. In actual fact we have more data than what we can depict on a map (Muehrcke, 1972). In this case categories need to be combined, but this must be limited. Firstly, when combining categories these must have very similar or shared characteristics. While we can combine two qualitative features into one class, for example common or similar language, we have to keep in mind that in the case of identity these can be much less similar than we think at first. Another aspect is that only one of the original categories that will be combined can be large enough to have a dominance in a certain area of the map. In other words, all but one category must be a very small local minority. A good example is the Bunjevci (an ethnic group living mostly in Serbia, Croatia and Hungary). If the map shows the area where they live in detail, they should not be combined with another category. If the title of the map contains any reference to them, then they should also not be combined. But if neither of these cases exist then they can be combined with one of the large south Slavic groups (Croats or Serbs) since their languages are similar. Due to their language, they often are declared as Serbs, while due to their religion they are declared as Croats in many cases. While this does cause a problem regarding identity it does not materially change the picture a map of, for example, the Carpathian Basin communicates to the map user since both the population and the area inhabited by the Bunjevci is very small, and they are in many ways similar to the other two ethnic groups. If one however looks at the Croats and the Serbs the criteria of not altering the picture does not stand. The foundation for a common Serbo-Croation language was created in Vienna in 1850 and was codified in 1954 after which this became the official language of Yugoslavia. In 1971 the Croats demanded that their language be accepted as one of the languages of Yugoslavia which in 1974 was acknowledged by the Yugoslav government (Jordan, 2002). This means that, while similar, one by no means can call the two languages the same. While the two ethnic groups speak similar languages and have both common features in their cultures and many differences, each ethnic group inhabits a large area in the Carpathian Basin so on a map showing the region the picture communicated to the map reader is severely distorted should these categories be combined. While attempts were made to combine these

categories it is clear that one cannot regard them as the same lingual, ethnic or cultural group (Krallert, 1961).

While combining categories on maps does happen creating new categories is under no circumstances the job of the cartographer. There have been maps where such categories have appeared and, in most cases, these cannot be proven by any available data from the time of the map's making.

The last important factor is the map's scale. This is something that appears on all maps and, in the case of topographic maps, there are certain practices that have standardized the scale. Since the base maps used on thematic maps are overgeneralized topographic maps the scale used has been standardized but one still needs to take the usual problems of the scale into account: the smaller the scale the less information can be shown on a map. The larger the scale the larger the map making it harder to have a general picture of a given area. If the map cannot be printed on one sheet reading the map becomes very complicated and time consuming which, again, makes it very difficult for the map reader to get an accurate picture of the ethnic structure of the depicted area even if the map itself is very accurate. On large scale maps the exact geographical location of the population can be depicted much more precisely.

3. DEPICTING ETHNIC GROUPS IN PRACTICE

While the concepts discussed above are great concepts in theory, it is often very difficult to apply them in practice. These concepts contradict each other to a certain degree thus applying all of them in full is impossible. Hence the question the mapmakers need to ask themselves is not if one is able to apply these concepts in full by checking if the map shows density of the population while depicting the given population in exactly the geographical area where they live all the while keeping the map legible. At the same time cartographers need to choose a mapping method that does show the statistical data provided to the extent possible in an objective manner (Krallert, 1961).

Analyzing this is the best when one uses historical examples. The largest number of ethnic maps using different mapping methods that both apply the above concepts and others that prove the negative effects of the lack of applying the above concepts were made at the end of the First World War of the Carpathian Basin. It is important when selecting the maps to be analyzed that both positive and negative examples should be available from the same era and the same area should be depicted on all maps. The examples, while there will be some from all parts of the Carpathian Basin, will focus on Transylvania since this is the area where (i) most different maps are available and (ii) the terrain makes applying these concepts even more important.

3.1. Choosing an ideal projection and scale

Before a map can be made in any way a scale and projection must be chosen and all information depicted on the map must be depicted at the chosen scale. As far as the projection is concerned an equal area projection should be used when depicting pop-

ulation since the goal of the map is to present data about the population in geographical space. This means that the mapmaker wants to communicate information about the territory inhabited by a certain group of people. The choice of ideal projection in practice depends on the depicted territory. In the temperate climatic zones, one would generally choose a conic projection while in the tropics, due to its closer proximity to the equator, one would choose a cylindrical projection (Cauvin et al., 2010a). At the poles a plane projection would be the best, but this is not a question that would arise in practice since those regions a very sparsely inhabited. In the case of the Carpathian Basin (or parts of it) one can say that in general an equal area conic projection is what one should use. It is however important that the central meridian and the central parallel should be visible on the map since these define the starting point of the projection, which also define the distortion free area on the map. The further a given point on the map is from the distortion free area the greater the distortion on the map.

In practice the maps showing population are often based on an existing map. Before computers became widely available in the 1990s the calculation of projections was a strenuous task. Today the method that Muehrcke was expecting is available in all commercial and open-source GIS software. However, that when automation is used the concepts developed before automation still need to be applied.

The original topographic map was usually heavily generalized and the projection was very rarely recalculated. The intense generalization is necessary in order to avoid overloading the map and making it cluttered (Frenzel, 1967). While it is true that usually equal area conic projections were used, especially on Romanian maps that depicted only the eastern parts of the Carpathian Basin, the starting point of the projection is not on the map. While this should be avoided on all maps it can be said that this had less effect on how the ethnic structure of the area communicated by the map to its user than other factors discussed in this study.

When choosing the scale one must keep in mind the size of the depicted area. The smaller the scale the more heavily the map must be generalized. The choice of the scale on maps generally depends on the size of the smallest object. Unless the symbol depicting the object is enlarged on the map (for example roads that become too narrow to depict at the given scale), it will have to be removed from the map. The smallest depictable object on a map is 0.25 mm (Cauvin et al., 2010a). This applies not only to topographic data on the base map but also to the thematic data on the map. Depicting thematic data does have its similarities to depicting topographic data. If the area of the sampled data or its geographical neighborhood are smaller than the mesh size on the map the information will be lost (Muehrcke, 1972). Enlarging symbols showing population will distort the picture as will removing it. This needs to be compensated using the correct set of symbols. All types of thematic maps have their own set of rules, so one should not try to apply rules developed for topographic maps (Cauvin et al., 2010a). Using different mapping methods can mitigate this loss to a certain extent but in general the basic concept that larger scale maps can hold more information also stands in the case of ethnic maps. This means that the mapping method used on the map depends on the scale of the map.

While large scale maps can hold large amount of information two further aspects have to be considered. Firstly, one must have an understanding as to how much information someone can interpret from the picture and how long this will take. While some people will analyze the map for long periods of time most people need a fast oversight of the map to get an objective picture. Secondly, the larger the scale of the map the larger the map sheet of a given area will be. If the sheet would become too large the map has to be printed onto multiple sheets. This makes a complete oversight of the area very difficult. Initially this was not considered by Hungarian cartographers resulting in a map printed on 54 sheets at a scale of 1 : 200 000. The map made by Zsigmond Bátky and Károly Kogutowicz showed the number of inhabitants and their ethnic affiliation but would have been so large if the sheets were fitted that most rooms would not have been large enough to accommodate for this (Bátky & Kogutowicz, 1918). But even if this would have been possible no map reader would have had any oversight of the area. Studying the sheets individually and putting the picture together in a person's head is very time consuming and only very experienced map users can do this and get an accurate picture of the ethnic structure of the area. The map is a dot map where a small half circle shows 50 inhabitants, a small circle shows 100 inhabitants, a large half circle shows 500 inhabitants, and a large circle shows 1000 inhabitants (Kocsis, 2007). The circles are grouped in such a way that all inhabitants represented by a given dot like symbol belong to the same ethnic group. The color of the symbol presents the ethnic group. Dot maps such as this one are the best in showing the exact topographic location (Jordan, 1999) and the exact number of the different ethnic groups (Jordan, 1999).

After this very accurate map was made, they did realize that while very accurate and precise the scale of the map made it just about impossible to read. After this the scale was reduced and the map was republished at a scale of 1:300 000 on 12 sheets (Bátky & Kogutowicz, 1919). While this did reduce its size without severely affecting its contents the problem that the map was on multiple sheets was not solved. The scale was reduced again to 1 : 900 000 by Jenő Dörre and Ernő Lux (Kocsis, 2007). Loss of data did occur in this case since the first two maps used symbols showing 50 inhabitants, and the 1 : 900 000 map used only symbols showing 1000 inhabitants (Lux & Dörre, 1919). This generalization had to be done since when reducing the scale one cannot have symbols covering each other, otherwise the map will not convey an objective picture of the data shown (Arnberger, 1966), in this case the ethnic affiliation of the population. While the problem of the scale was solved and one could conclude that a map of a scale around 1 : 1 000 000 is ideal for depicting the Carpathian Basin the mapping method still had several shortcomings. It was however clear that the ideal scale of the map was found and that this map could be printed on one sheet that any map user could handle.

3.2. Mitigating data loss

One can see in the above that while a larger scale does give more opportunities to depict the density of the population on a map that shows ethnic affiliation of the population an ethnic map of the Carpathian Basin that has a scale larger then

1 : 1 000 000 is hard to read and hard to handle. This means that a good, easy to use map of the Carpathian Basin cannot have a scale that is larger than 1 : 1 000 000. A mapping method had to be created that showed the density of the population in such a way that minimizes the data loss at the prescribed scale, does not clutter the map, and lets the user have a fast oversight of the ethnic structure of the area. When choosing map symbols for such a map one has to choose symbols that are simple to read. One has to take care of the symbols such that after being tested for convenience and simplicity they still have to function as expected when brought together on a map (Muehrcke, 1972).

If one analyses the maps made by Zsigmond Bátky and Károly Kogutowicz one can see that while the mapping method is very precise it is hard to read. This is not only due to the scale since the map uses a dot symbol method that only creates very small areas that are colored in a certain color that represent a given ethnic group. Dots are discrete so they will lead the eye to see them as discrete while surfaces give the impression of continuity (Cauvin et al., 2010a). While the map does show the uninhabited areas the colored surface of one specific symbol is rather small. Due to this any given color does not even dominate the area of the map inhabited by the given population and the map reader does not have a picture on which areas of a specific color exist, rather spots of that color. Due to this the user cannot see the larger areas dominated by a specific ethnic group. This information can be gathered from the map but is time consuming. Furthermore, when the scale is reduced to 1 : 900 000 the loss of information is too large to create an accurate picture of the ethnic structure of the area. This meant that a mapping method had to be created which could depict the ethnic structure and density of the population of the Carpathian Basin without extensive loss of data.

The fact that data is lost is a feature of mapping. One however had to set a limit as to how much data loss could be tolerated. To get an accurate picture this limit had to be set to a point where the local minorities had to be visible. A problem that arises from generalization is that when the thematic content is generalized the local small minorities start disappearing. This cannot be completely avoided, but when the picture of an area gets homogenized to an extent that creates the impression that only one ethnic group resides in an area while a significant number of inhabitants live there who are members of another ethnic group or groups the map communicates a false picture. This meant that a mapping method had to be developed that could meet these criteria at a scale of around 1 : 1 000 000.

3.3. Showing the ratio of ethnic groups

When a symbol shows the ethnic group that makes up the majority in the area represented by the symbol the minorities cannot be seen. Reducing the area the symbol represents mitigates this problem, however the smaller the scale, the less this method can be applied. Since it is clear from the above that the scale cannot be larger than 1 : 1 000 000 the method had to be adapted to this scale. Using surface symbols to show the majority would, at this scale, not show the ethnically mixed areas and the minorities in detail thus another method had to be constructed.

In 1918 the Hungarian government was developing such methods for the map to be used at the peace talks existing methods were analyzed and some even adopted. One of these methods was developed by Jenő Cholnoky in 1906 *(Figure 1)*. When Cholnoky had to flee Kolozsvár in 1918 he fled to Budapest and assisted the work of the Hungarian peace delegation, thus it was rather evident to try and use his method.

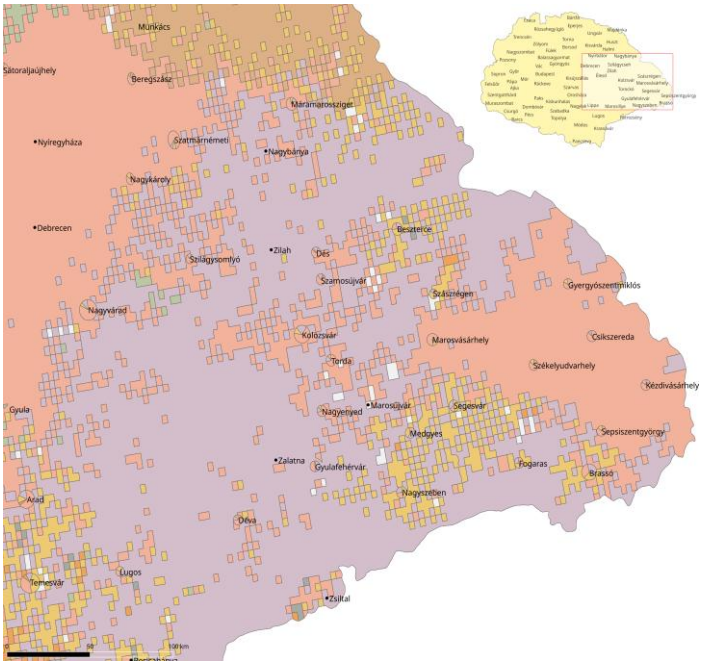

Figure 1

Eastern Transylvania on a reconstruction of the map made in 1918 using Cholnoky's method. The Hungarians are shown in red, the Romanian in purple, the Germans and Ruthenians in yellow, and other in white. The ethnically mixed areas can be seen well (reconstruction made by János Jeney)

Cholnoky's method used ratios instead of showing the majority. He used districts as reference areas for his symbols. The area of the Carpathian Basin was dived into small rectangles. Each district was made up of a certain number of rectangles and the number depended on the size of the district (Cholnoky, 1906). The percentage of rectangles colored in a certain color was the same as the percentage of the population of the district made up by a particular ethnic group. This means that each symbol represents a district and the symbols show the ratio of ethnic groups in the given district (Kocsis, 2007).

This method has its advantages and shortcomings. It fits into the scale of 1 : 1 000 000, but it can also be used effectively at smaller scales. The colored surfaces are large enough for the map reader to have an actual picture of the ethnic structure of the Carpathian Basin in a short time. The minorities can be clearly seen on the map, since the map does not homogenize the areas that have an ethnically

heterogeneous population. The areas with ethnically mixed population can be seen very well. However the map does not show the density of the population or any uninhabited areas. For this reason, the 1918 publication of the map is based on the 1910 census data and had an inset that showed the density (the real number and territorial distribution) of the population. The problem with this is that while the requested data is available it is shown on two maps. It is very difficult for the map reader to combine this into one picture, especially in a very limited amount of time. This meant that the density of the population had to be shown on one map for the map user to get an accurate picture.

3.4. Showing ethnic data based on the density of the population

Not showing the density of the population severely distorts the picture of the ethnic structure of the depicted area. The extent of this distortion depends on how much the density of the population differs in space: the larger these differences are in the depicted area the larger the distortion. In practice this means that in the Carpathian Basin mountainous areas not showing the density of the population results in much larger distortion than on flat plains. In other words, using colored surface symbols on maps to show very sparsely populated areas without showing the density of the population in any way severely distorts the picture of the ethnic structure and can be regarded as extremely manipulative (Jordan, 1999). The Romanians very often used colored surfaces to depict the ethnic groups. Using such a method would make the Romanian rural population (50 thousand) around Kolozsvár (Romanian: Cluj/Cluj-Napoca) seem eight times as large as the Hungarian population living inside the city (50 thousand) when in reality they were roughly equal (Kocsis, 2002).

It is important however that the criteria discussed above must be applied to such a map as well. This means that a map had to be created where the size of the population, the minorities, and ethnically mixed areas can be seen at a scale of maximum 1 : 1 000 000. It was also of concern that the map reader must get an accurate picture in a very short amount of time, meaning that the interpretation of the symbology cannot be overly complicated.

This was first achieved by Count Paul Teleki who created a map (actually a cartogram, a value-area map) in 1919 based on the census of 1910. All criteria discussed above were achieved. The cartogram[1] was made at a scale of 1 : 1 000 000. Every square millimeter on the map represented 100 inhabitants, and its color showed the ethnic affiliation of the depicted population *(Figure 2)*. If any inhabitants lived in an area where the population was less than 100 this population was added to the nearest inhabited area, meaning that every inhabitant was represented on the map. This led to the fact that while there was a minor error in the geographical area of some inhabitants, the general picture the map communicated of the ethnic composition of the

[1] The work is commonly known as a map since the base map actually does have a projection and is indeed a map. The thematic data however is presented in such a way that it resembles a cartogram, hence in this study it will be referred to as a cartogram since the study deals with the thematic data

Carpathian Basin is very accurate (Kocsis & Tátrai, 2006). Uninhabited and sparsely populated areas can be seen while the population numbers are also clearly visible (Teleki, 1919). If one looks at the method used for showing the thematic content on the map, one can say that the method resembles an anamorphic cartogram (Kocsis, 2007). Not all studies of this map interpreted its methodology correctly. When one looks at the map the white areas are often interpreted as uninhabited areas while in actual fact the legend states that they are uninhabited and sparsely populated areas. Often no mention of the fact is made that the areas where the population was less than 100 inhabitants these are added to the nearest populated area as it was the case in the publication of Wilfried Krallert in 1961 in the International Yearbook of Cartography (Krallert, 1961). At the same time, it is said the Bátky and Kogutowicz maps are very objective but no research is done into the interpretation of their mapping methods (Krallert, 1961). While the maps not showing the density of the population over represent the rural population this map shows the exact ratios.

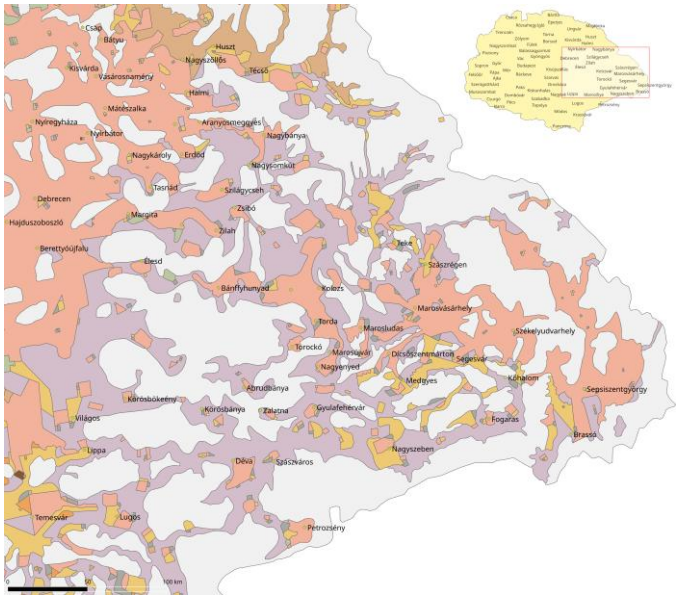

Figure 2

Transylvania based on the Teleki cartogram. Purple shows the Romanians, yellow the Germans, pink the Hungarians and gray the uninhabited and sparsely populated areas. One can see that on this value-area thematic map Romanians create a visual impression corresponding to their proportion within the contemporary population (1910: 55%). (reconstruction made by János Jeney)

Looking at it from the point of view of the ethnic composition one can see that in Transylvania the ratio of Romanians against the total population is much less than what it seems on maps not showing the density of the population. At the same time in the Banat the general picture is very similar to that conveyed by the map designed by Cholnoky since both show the mixture of the population. The method employed

on the map lets the map reader get an accurate picture in a very short time since colored surfaces and not colored spots are easily distinguished.

3.5. Maps with new categories

In the first part of this study, it was discussed that a mapmaker in some cases must combine categories if it is not possible to create the number of symbols needed to depict all categories on the map. A mapmaker cannot however create new categories since cartography is about depicting the data not about creating statistics. The map also must give reference to the source of the data otherwise it cannot be determined of the data is accurate or not.

Despite this a map has been made where very strange categories have been created that cannot be proven by any available census data. Aurelian Florinescu made a map where a new manipulative category was introduced by the name of "Hungarianized Romanians" (Florinescu, 1914). It is not clear what data source the mapmaker used for this category. While this type of category-creating is incorrect and fortunately uncommon it does happen from time to time. Similar issues arose on the ethnic map of the Balkans made by Jovan Cvijić of the Balkans where he added the category of "Albanized Serbs" on his map of Macedonia in 1909 (Wilkinson, 1951).

The symbology of the map is also of great interest. The symbol for the category of "Hungarianized Romanians" uses a symbol that is the same color as that used to depict Romanians. This causes the two symbols to be seen nearly as one by the map user. In fact, if the time available to interpret the map is very short the two symbols are seen as one. Since the symbols in theory depict very similar categories this would be a logical choice of symbology, but it is not clear how this category was created. This means that since there is no explanation for the source of this category on the map sheet the data represented by this symbol cannot be considered accurate.

Another interesting category on the map is the category of German and Romanian mixed areas. Since the map is severely overgeneralized, this could have been avoided by choosing a smaller reference area of the symbols. The symbol uses a pattern that also has the same color as used for the Romanian areas. The creation of this symbol can theoretically be justified by the cartographer since this was created by combing two existing categories but no criteria that is to be used for such combinations was followed. The categories of Germans and Romanians are not similar: both ethnic groups are present in large numbers in the depicted area and separate categories for Germans and for Romanians do exist on the same map. The map is overgeneralized to the extent that the German and Hungarian minorities in southern and western Transylvania are not visible. It is interesting however, that the Seklers in eastern Transylvania are shown as Hungarians and not "Hungarianized Romanians". This is correct, since the Seklers do consider themselves ethnic Hungarians and this is the data that is given by the census from that time (Florinescu, 1914).

Since the map is overgeneralized, it communicates a picture that shows a much larger percentage of Romanians in Transylvania than that shown by the maps made by both Teleki and Cholnoky. This is because the map is overgeneralized, and the minorities and ethnically mixed areas cannot be seen. The fact that the map does not

show the number of inhabitants further distorts this picture when compared to the Teleki cartogram (Teleki, 1919). The fact that the map contains an otherwise unknown category from an unknown data source further distorts this picture. It is safe to say that the map communicates a false picture of the ethnic structure of Transylvania.

3.6. Maps with inconsistent symbology

When creating a map the symbols used in the legend must be applied in all areas of the map. This means that if, for example, the legend has a symbol for uninhabited areas the map must show all uninhabited areas. One can see from the above examples that the depiction of uninhabited areas on ethnic maps is very important for the map to be able to communicate an accurate picture of the ethnic structure of a given area.

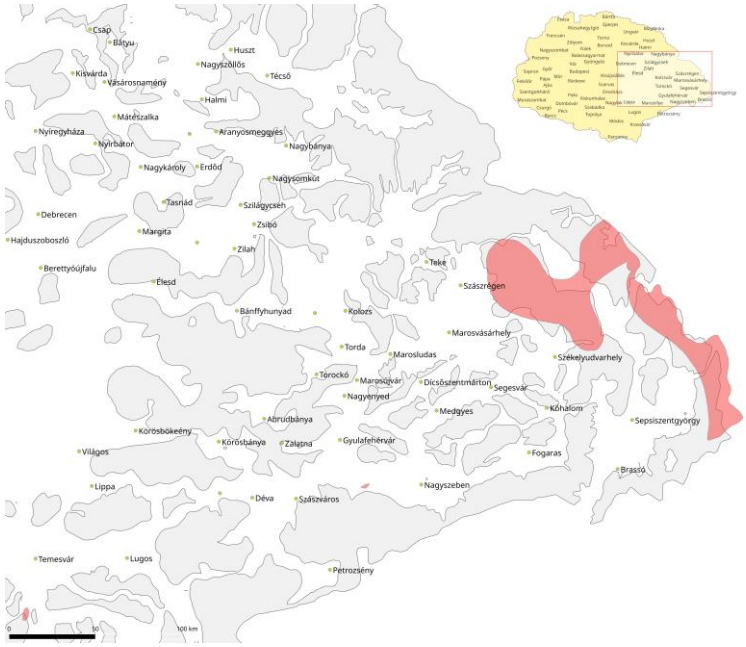

Figure 3

Uninhabited areas shown on the Teleki map (gray) and uninhabited areas show on the Popa & Istrate map (red). One can see the gray areas under the red areas, but other uninhabited areas seen on the Teleki map cannot be seen on the Popa & Istrate map. (reconstruction made by János Jeney)

On a map made by Val. Popa and N. Istrate a category of uninhabited areas is shown in the legend. This does appear on the map in the middle of Seklerland which is inhabited dominantly by Hungarians. While the area shown by this symbol is largely uninhabited the fact that no other uninhabited areas are shown makes this a very serious mistake (Popa & Istrate, 1916). Having such a symbol on the map creates the impression that all uninhabited areas are shown on the map. While ethnic maps generally do not show relief since this would make reading the map very difficult, it is

rather clear that high mountains in general are usually uninhabited with the population living in valleys. The edge of this uninhabited area is on a ridge on the top of the Carpathian Mountains which is unrealistic. Furthermore, other uninhabited areas are not shown on the map *(Figure 3)*. Since the other uninhabited areas not shown are in the proximity of Romanian-inhabited areas and are shown as Romanian areas, the uninhabited areas shown are in the proximity of areas inhabited by Hungarians should also have been shown as Hungarian areas Using this symbol in the way it was used distorts the picture even more than if no uninhabited areas were shown. The map is overgeneralized, thus the minorities are invisible which distorts the picture even more creating the impression of an even larger Romanian dominance in Transylvania.

3.7. Showing ethnically mixed areas using one symbol

As it can be seen from the previous examples a reference area of a symbol has to be as small as possible. If this is not the case the map either homogenizes the picture of the ethnic landscape or new symbols are created which cause confusion.

British cartographer B. C. Wallis used a method in which symbols used different shades of a color to represent the percentage of a given group living in a certain area. A light shade of a certain color showed that a certain ethnic group made up 25% of the population, a somewhat darker shade of the same color showed that the given ethnic group made up over 50% of the population and an even darker shade showed that the ethnic group made up over 90% of the total population (Wallis, 1918). In ethnically mixed areas this made the map cluttered and no information could be read from the map. This in general could have been avoided if the mapmaker would have used symbols with a much smaller reference area. After having made this map Wallis decided to publish another version where the category showing the population between 25% and 50% was scrapped. This resulted in a map that was not cluttered, but the loss of information was extremely large. Large areas are shown where the ethnic group shown only makes up 50%–90% of the population, and no information is provided as to which other ethnic group or groups live in the area. The map reader does not even know how many other ethnic groups live in the given area and where in the area they live. Areas where no ethnic group makes up 50% of the population are left white. A white symbol is created in the legend to depict mixed areas creating further information loss, since the map has large areas where no information is available about the ethnic composition other than the fact that they are mixed. Through this symbology even extent to which these areas are ethnically mixed is not communicated very well since all the map reader sees is one large homogeneous area. This heavily overgeneralizes the map, and severely distorts the picture the map communicates to the map reader. In the Banat for example large white areas are seen where no information is communicated about the area represented by the given symbol other than that no ethnic group makes up 50% of the population in that area.

3.8. Showing uninhabited areas using the same symbol as another category

In the previous examples it can be clearly seen that depicting uninhabited areas is crucial to communicate an accurate picture. If these are not shown the area has to be colored in such a way that represents the inhabited areas around it in order to preserve the ratios of ethnic groups on the map as much as possible.

On a map made by Prof. Demetresco this is not adhered to. All uninhabited areas regardless of where they were found were shown as if they were inhabited by Romanians *(Figure 4)*. Many of these areas are not just uninhabited but also uninhabitable since these are in high mountains. The uninhabited areas in Seklerland are shown as areas inhabited by Romanians. While the fact that no uninhabited areas are shown on the map distorts the picture the map communicates of the ethnic landscape, but showing uninhabited areas in the proximity of areas inhabited by Hungarians as if they were inhabited by Romanians distorts the picture to an even greater extent. By doing this the map would need to have a data source according to which the areas concerned are inhabited by Romanians. No data source is shown on the map, which discredits the information shown on the map (Demetresco, 1919).

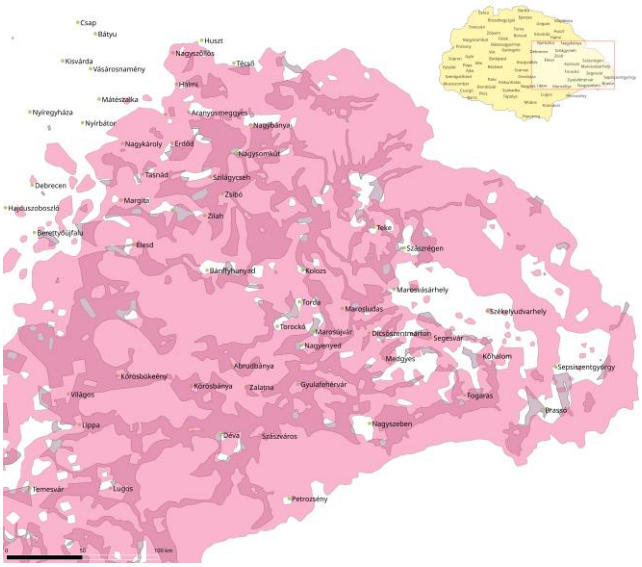

Figure 4

Romanians show on the Demetresco map (pink) and Romanians shown on the Teleki map (purple and dark pink). It can be clearly seen that by showing uninhabited areas as if they were inhabited by Romanians changes the picture of the dominance of Romanians in the area. (reconstruction made by János Jeney)

4. CONCLUSION

The mapping method used on a map heavily affects how information is conveyed by the map to the user. While using a larger scale can help to convey more information

to the user increasing the scale increases the size of the map. If the map is too large reading the map becomes very difficult and creating a picture of the ethnic landscape of the depicted area becomes impossible. One must find the maximum scale that can be used to depict the area and then find or develop a mapping method that can depict the population in such a way that gives an accurate picture of the ethnic landscape of the mapped area. Two very important aspects when choosing the mapping method is that the minorities should be visible and that the density of the population should also be visible on the map especially when the density of the population is very heterogeneous in the mapped area.

While it can be seen from the examples how to improve the quality of the map to convey an accurate picture of the ethnic structure of the mapped area other examples show what happens if very basic cartographic principles are adhered to. In these cases, the picture of the mapped area is severely distorted especially when the symbols in the legend are not applied consecutively or the thematic content, in this case the ethnic affiliation of the population, is overgeneralized.

While it is clear from the above that some methods show a more accurate picture than others, inaccurate methods were used by some mapmakers (especially Romanian mapmakers). This happened even though by then it was clear that these methods were inaccurate. When one simply handles these maps as simple thematic maps this seems irrational. The only rational explanation is that ethnic maps were always made using political motives since one of their primary functions was to influence decision makers redrawing borders.

REFERENCES

Arnberger, E. (1966). *Handbuch der thematischen Kartographie.* Wien, Franz Deuticke, p. 187.

Unknown author (1940). *Rumänische Landkartenfälschungen.* Budapest, Staatwissenshcaftliches Institut, p. 24.

Cauvin, C., Escobar, F., Serradj, A. (2010). *Thematic Cartography and Transformations.* Hoboken–London, John Wiley & Sons Inc & ISTE Ltd., p. 41, 98, 100, 228, 324. https://doi.org/10.1002/9781118558133

Cauvin, C., Escobar, F., Serradj, A. (2010). *Cartography and the Impact of the Quantitative Revolution.* Hoboken & London, John Wiley & Sons Inc & ISTE Ltd., p. 7. https://doi.org/10.1002/9781118558126

Cholnoky J. (1906). *Magyarország néprajzi térképe.* Budapest, Magyar Földrajzi Intézet.

Demetresco, Sc. (1919). *Carte Ethnographique des Régions Habitées par les Roumains.* Paris, Imp Dufrénoy.

Florinescu, A. (1914). *Harta Ethnografica a Ţinuturilor Romaneşti de sub Stapanirea Austro-Ungara.* Bucureşti, Institutul de Arte grafice C. Sfetea.

Frenzel, K. (1967). Das kartographische Problem der Darstellung des Lebensraumes in thematische Karten, insbesondere Wirtschaftkarten. In: Frenzel, K., Aurada, F., Castiglioni, M., Imhof, E., Ormeling, F., Bartholomew, J., Gaussen, H., Lundqvist, G., Otremba, E., Robinson, A. (eds). *International Yearbook of Cartography.* Wien, International Cartographic Association, Freytag – Berndt & Artaria, pp. 136–142. p. 137

Jordan, P. (1999). Können ethnische Karten objektiv sein? Möglichkeiten und Grenzen der Darstellung ethnischer Strukturen in Karten. In: Kretschmer, I., Kriz, K. (eds). *25 Jahre Studienweig Kartographie.* Wien, Institut für Geographie der Universität Wien, Ordinariat für Geographie und Kartographie, p. 121, 122, 125, 126.

Jordan, P. (2002). Die ethnische Struktur des mittleren und östlichen Europas (anhand der Karten des Atlasses Ost- und Südosteuropas). In: Kraas, F., Stadelbauer, J. (eds). *Nationalitäten ind Minderheiten in Mittel- und Osteuropa.* Wien, Universitäts- Verlagsbuchhandlung Ges.m.b.H., p. 33.

Klinghammer I., Papp-Váry Á. (1983). *Földünk tükre a térkép.* Budapest, Gondolat, p. 184.

Klighammer I., Papp-Váry Á. (1991). *Tematikus kartográfia.* Budapest, Tankönyvkiadó, p. 28.

Klinghammer I., Török Z. (1995). A tematikus kartográfia fejlődése. In: Klinghammer I., Pápay G., Török Z. (eds.). *Kartográfiatörténet.* Budapest, Eötvös Kiadó, p. 161.

Kocsis K. (1989). *Vegyes etnikumú területek társadalmának népességföldrajzi kutatása Szlovákia és a Vajdaság példáján.* Debrecen, Studia Geographica, p. 12.

Kocsis K. (2002). Vázlat a magyar enikai térképezés történetéhez. *Néprajzi látóhatár*, XI (1–4), p. 230.

Kocsis, K., Tátrai, P. (2006). Contributions to the History of the Hungarian Ethnic Mapping. *Studia Cartologica*, 2006 (13), p. 252.

Kocsis, K. (2007). Beiträge zur Geschichte der ungarischen ethnischen Kartographie im Karpatenbacken. In: Hurni, L., Klinghammer, I., Rounitschek, W. (Hrsg.). *Thematische Kartierungen in den Geowissenschaften* [Sonderausgabe]. Nova acta Leopoldina 94 (349). Halle (Saale), Deutsche Akademie der Naturforscher Leopoldina.

Bátky, Zs., Kogutowicz, K. (1918). *Ethnographical map of Hungary.* Budapest, Hungarian Geographical Society.

Bátky Zs., Kogutowicz K. (1919). *Magyarország néprajzi térképe.* Budapest, Magyar Földrajzi Intézet.

Krallert, W. (1961). Methodische Probleme der Völker- und Sprachenkarten, dargestellt an Beispielen von Karten über Ost- und Südosteuropa. In: Imhof, E.,

Aurada, F., Castiglioni, M., Lehmann, E., Robinson, A, Bartholomew, J., Gaussen, H., Mannerfelt, C., Sijmons, A. (eds). *International Yearbook of Cartography.* Günterloh, International Cartographic Association, C. Bertelmann Verlag, pp. 99–120, p. 100, 107–109, 117.

Lux E., Dörre J. (1919). *Magyarország néprajzi térképe.* Budapest, Klösz György és Fia Térképészeti Műintézet.

Muehrcke, P. (1972). *Thematic Cartography.* Washington D.C., Association of American Geographers Commission on College Geography, p. 5, 7, 11, 47, 54.

Popa, V., Istrate, N. (1916). *Harta Ethnografica Pămatului Romanesc.* Unknown publisher.

Robinson, A. (1961). The Cartographic Representation of the Statistical Surface. In: Imhof, E., Aurada, F., Castiglioni, M., Lehmann, E., Robinson, A., Bartholomew, J., Gaussen, H., Mannerfelt, C., Sijmons, A. (eds). *International Yearbook of Cartography.* Günterloh, International Cartographic Association, C. Bertelmann Verlag, pp. 53–63, p. 55.

Robinson, A. (1967). Psychological aspects of colour in cartography. In: Frenzel, K., Aurada, F., Castiglioni, M., Imhof, E., Ormeling, F., Bartholomew, J., Gaussen, H., Lundqvist, G., Otremba, E., Robinson, A. (eds). *International Yearbook of Cartography.* Wien, International Cartographic Association, Freytag – Berndt & Artaria, pp. 50–61, p. 53, 54, 56.

Teleki P. (1919). *Magyarország néprajzi térképe a népsűrűség alapján.* Budapest, Klösz György és Fia Térképészeti Műintézet.

Wallis, B. C. (1918). *Eastern Hungary: Natioalities.* New York, The American Geographical Society of New York.

Wilkinson, H. R. (1951). *Maps and Politics. A Review of the Ethnographic Cartography of Macedonia.* Liverpool, University Press of Liverpool. p. 175.

Geosciences and Engineering, Vol. 12, No. 2 (2024), pp. 25–36.
https://doi.org/10.33030/geosciences.2024.02.002

APPLICATION OF COLUMN TESTS TO DERIVE TRANSPORT PARAMETERS OF MANGANESE IN MINE WASTE DUMP MATERIAL OF RUDABÁNYA

MÁRTON TÓTH[1]*, ENIKŐ TÓTH-DARABOS[2], BALÁZS KOVÁCS[3]
[1, 2, 3] *Institute of Water and Environmental Management, National Laboratory for Water Science and Water Security, University of Miskolc*
[1]*marton.toth@uni-miskolc.hu
[2]eniko.darabos@uni-miskolc.hu
[3]balazs.kovacs@uni-miskolc.hu
[1]https://orcid.org/0000-0002-8262-2748
[2]https://orcid.org/0009-0008-7477-7898
[3]https://orcid.org/0000-0002-3594-7355

Abstract: The most accurate method to create a transport model of an area is to determine the transport parameters of a contaminant in the investigated porous media. The batch and column tests are the tools that can be used to derive this information. To describe the transport process in a column, 1D transport equation is applicable therefore the equation's analytical solution becomes possible. In our work, two-column test setups were investigated from the aspect of their accuracy in the determination of longitudinal dispersivity, retardation factor, and irreversible reaction rate constant, respectively. In the first measurement method, a solution with constant concentration (0.01 M Mn solution) was percolated through the column filled with mine waste dump material. In the second measurement method, distilled water was percolated through the column continuously but in a moment an impulse amount of manganese (10 ml 0.5 M Mn solution) was injected into the column at its bottom. The first measurement served the breakthrough curve (BTC), and the second measurement resulted the impulse curve (IMP). The retardation factor of Mn found in the media is similar in both measurement setups ($R_{BTC} = 1.87$, $R_{IMP} = 1.47$). The value of the irreversible reaction rate constant differs in the two experiments; an order of magnitude difference was found between the result of the breakthrough test ($\mu_{BTC} = 6.94 \cdot 10^{-5}$ 1/s) and the impulse test ($\mu_{IMP} = 2.09 \cdot 10^{-4}$ 1/s).

Keywords: *heavy metal, breakthrough test, mine waste dump, irreversible reaction rate*

1. INTRODUCTION

Heavy metal contaminations related to various human activities are crucial environmental hazards waiting for management and solutions (Sharma and Reddy, 2004). With their high pervasion, persistence, and toxicity they threaten ecosystem services, and they potentially have human health implications (Moulatlet et al., 2023). Potentially toxic heavy metals like Cd, Cr, Cu, Hg, Mn, Ni, Pb and Zn could be released during the mining-, industrial-, agricultural-, traffic- and waste-deposing activity (Heltai et al., 2018).

During the mining and milling processes, four types of waste could be generated which could have significant environmental hazards of their heavy metal content, like mine waste, tailings, dump heap leach, and acid mine water (Anju and Banerjee, 2010). The exploited ore never can separate from secondary rocks, so the mine waste always has significant heavy metal content (Zou and Ren, 2023) but their mobility is significantly dependent on their mineralogical forms. Generally, in the mines, heavy metals can be found in sulfide-bearing ores, and between them iron sulfide is an outstanding one that can be oxidized quickly after they are brought to the surface. The oxidation of iron (and after its hydrolysis) releases a significant amount of acid into the environment (Stumm and Morgan, 1996). This process is Acid Mine Drainage (AMD) which is another well-known environmental hazard related to mines (Zheng et al., 2023) occurring not just in mine waste dumps but also in the open pits and drifts. Water affected by AMD has a very low pH (pH ≈ 2-3) and it has a high reduction-oxidation potential which serves the proper conditions for heavy metals to be dissolved and transported with the percolating water. Then contaminated water can flow on the surface as surface runoff threatens surface water resources or after infiltration through the vadose zone, it can deteriorate aquifers (Tomiyama and Igarashi, 2022).

Implementation of remediation is not always necessary when heavy metal contamination occurs but to constrain and forecast the movement of the plume is crucial. To manage heavy metal contaminations in groundwaters the transport models are frequently used tools (Kresic, 2007). In porous media of mine waste dumps, the dissolved heavy metals are affected by the following transport processes: advection, hydrodynamic dispersion, chemical–biochemical reactions such as adsorption-desorption reactions, acid-base reactions, solution-precipitation reactions, oxidation-reduction reactions, ion pairing or complexation, and microbial cell synthesis (Freeze and Cherry, 1979). An appropriate transport model describing the investigated environmental situation postulates reliable parameters. These parameters could be determined in column experiments which are commonly used procedures (Kang et al., 2021; Mufalo et al., 2023). Transport of heavy metals in columns is a special case of transport modeling that can be described by 1D transport equations therefore application of an analytical solution is possible. In transport equations, the concentration change in function of time or location is determined by a couple of parameters but not all of them can be measured easily as flow velocity, initial concentration, or porosity. The determination of the dispersion constant, retardation factor, and irreversible reaction rate constant is an iterative work by the fitting of the properly selected form of the 1D transport equation which depends on boundary conditions. The retardation factor, the dispersion constant can be determined according to Ogata and Banks's solution (1961) that presumes reversible processes as reversible adsorption (Czinkota et al., 2006). But in more complex situations additional parameters such as first-order irreversible reaction rate constant and first-order production should be involved (Van Genuchten, 1981) to solve the transport problem.

1.1. Study area

Rudabánya is an old, abandoned mine site in north-east Hungary located in the Aggtelek-Rudabánya Mountains *(Figure 1a)*. Geological formations of the area are building units of the Silicic Superunit of the ALCAPA region. The elements of the Silicic Superunit are Upper Permian- Lower Triassic evaporites, Lower Triassic siliciclastic formations and carbonates, and Middle-Upper Triassic and Jurassic carbonates (Szentpétery and Less, 1986). The origin of mineralization occurs in several superposed periods (Földessy et al., 2010). The first period of ore formation was a synsedimentary, stratiform, sedimentary-exhalative Pb-Zn accumulation associated with barite and pyrite (Nemeth et al., 2013). After, probably in the Cretaceous age, during the process of metasomatism siderite was generated in the Lower-Middle Triassic carbonates (Bodor et al., 2016). In the last phase of ore formation pyrite-bearing massive sulfide-filled veins with later lead-, zinc-, silver-, and copper enrichments were generated (Földessy et al., 2010).
The open pit and underground iron ore (siderite and limonite) mining activity took place in Rudabánya between 1872 and 1985 resulting in a lot of mine waste dumps with significant heavy metal content [nowadays these waste dumps are under investigation as secondary raw material (Földessy et al., 2010)]. In the closure procedure of the mine, mechanical recultivation was performed by the explosion of steep walls of the open pit and by filling up of emptied areas but the open pit was not filled up where a lake was formed from the concentration of surface and subsurface waters (Balla et al., 1987). Mine waste dumps all over the mine site were not recultivated, their environmental impact now is under investigation in our research.

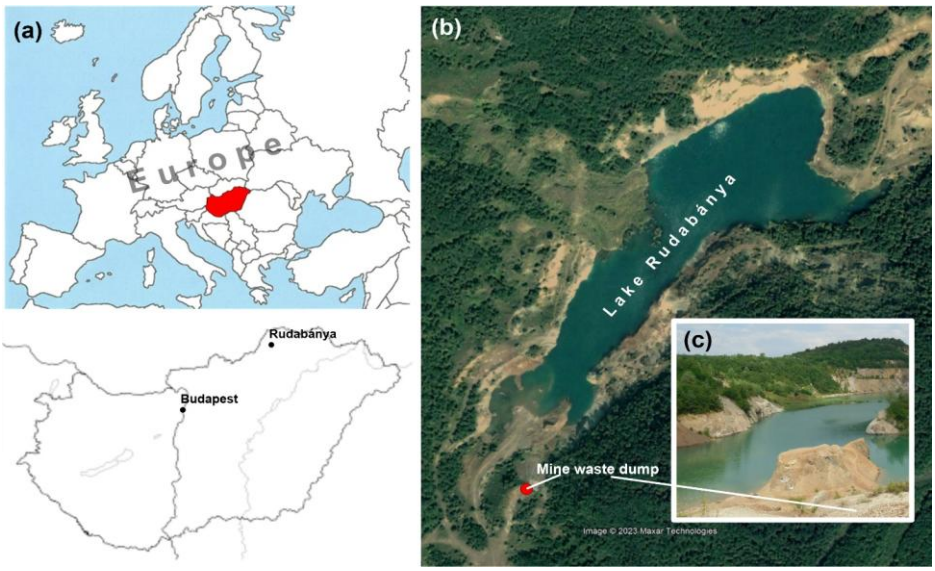

Figure 1

(a) Location of abandoned mine site of Rudabánya, (b) Location of the investigated mine waste dump, (c) View of the lake from the sampled mine waste dump

2. MATERIALS AND METHODS

2.1. Soil sampling

Mine waste dump material (MWDM) was collected from the upper 20 cm depth of a waste dump on the abandoned mine site of Rudabánya *(Figure 1b–c)*. Because the research work aimed to answer the vulnerability of surface waters against heavy metal leaching from waste dumps, the samples were collected from waste dumps near Lake Rudabánya. The collected material was placed in a PE bag and immediately brought to the laboratory. The drying of the sample happened at 105 °C until reaching mass constancy, then bigger aggregates were crushed in a mortar to prepare for sieving. Particles above a diameter of 8 mm were removed from the sample because they were not fitted to the inner dimensions of the column, and their lack did not influence the result of the column test because the reactive particles can be found below a diameter of 0.2 mm (Plassard et al., 2000). Based on the grain size distribution of the filling material, the prepared sample for the column test consisted of approximately 70% gravel, 21.5% sand, 7.5% silt, and 1% clay.

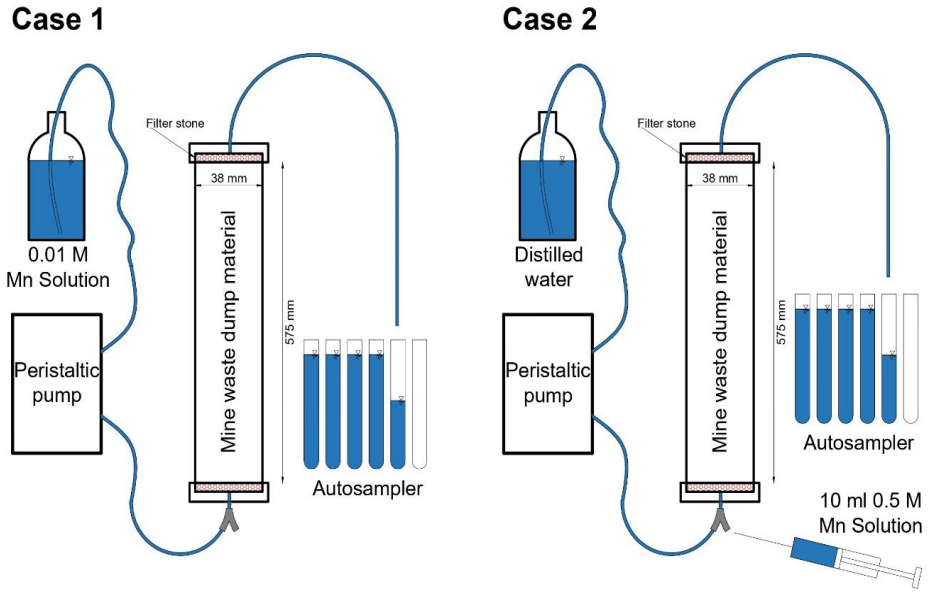

Figure 2
Schematic view of the experimental setup

2.2. Column experiment

Prepared MWDM was packed into a 575 mm length and 38 mm inner diameter Plexiglas column, yielding an approximate packing density of 1.96 g/cm^3 and a porosity

of 0.4 v/v determined according to average particle density from pycnometer measurements (Tan, 1995). The column was flushed with 10 pore volumes of distilled water to remove contaminants and to check the hydraulic stability of built-in materials. Metal solutions were then fed into the column from the bottom with a flow rate of ca. 24 ml/min which meant 0.04 cm/s flow velocity. Two-type of break through experiments were performed; in the first case an Mn solution (pH = 6 at 25 °C) with a constant concentration of 0.01 M was driven through the column, in the second case 10 ml of 0.5 M concentration of Mn solution (pH = 6 at 25 °C) was injected into the column at its bottom, then only just distilled water was fed into the column *(Figure 2)*. The effluent fluid in both cases was collected in 10 ml units until the total flow-through volume exceeded 5 times the pore volume. The collected samples were analyzed by a UniCam 929 AAS. In the following, we refer to the first measurement setup as a breakthrough test (BTC) (described later by *Equation 6*). and to the second measurement as an impulse test (IMP) (described later by *Equation 9*).

2.3. Mathematical background of experiments

The governing equation describes the transport of any compound in porous media in case of constant volumetric moisture content and volumetric fluid velocity (Van Genuchten, 1981)

$$R\frac{\partial c}{\partial t} = D\frac{\partial^2 c}{\partial x^2} - v\frac{\partial c}{\partial x} - \mu c + \gamma \tag{1}$$

where R is the retardation factor, c is the solution concentration (mg/L), t is time (s), D is dispersion coefficient (cm^2/s), x is the distance (cm), v is pore-water velocity (cm/s), μ is irreversible reaction rate constant (decay) and γ is production coefficient (Goode and Konikow, 1989).

We apply the following boundary conditions (Van Genuchten, 1981)

$$c(x,0) = C_i$$

$$c(0,t) = \begin{cases} C_0 & 0 < t < t_0 \\ 0 & t > t_0 \end{cases}$$

$$\frac{\partial c}{\partial x}(\infty,t) = 0$$

where C_i is initial concentration, the C_0 is input concentration and t_0 is duration of solute pulse. The analytical solution of *Equation 1* is

$$c(x,t) =$$

$$\begin{cases} and\frac{\gamma}{\mu} + \left(C_i - \frac{\gamma}{\mu}\right)A(x,t) + \left(C_0 - \frac{\gamma}{\mu}\right)B(x,t) & 0 < t < t_0 \\ and\frac{\gamma}{\mu} + \left(C_i - \frac{\gamma}{\mu}\right)A(x,t) + \left(C_0 - \frac{\gamma}{\mu}\right)B(x,t) - C_0B(x,t-t_0) & t > t_0 \end{cases} \quad (2)$$

where

$$A(x,t) = e^{\left(\frac{-\mu t}{R}\right)}\left\{1 - \frac{1}{2}erfc\left[\frac{Rx-vt}{2\sqrt{DRt}}\right] - \frac{1}{2}e^{\left(\frac{vx}{D}\right)}erfc\left[\frac{Rx+vt}{2\sqrt{DRt}}\right]\right\} \quad (3)$$

$$B(x,t) = \frac{1}{2}e^{\left[\frac{(v-u)x}{2D}\right]}erfc\left[\frac{Rx-ut}{2\sqrt{DRt}}\right] + \frac{1}{2}e^{\left[\frac{(v+u)x}{2D}\right]}erfc\left[\frac{Rx+ut}{2\sqrt{DRt}}\right] \quad (4)$$

and

$$u = v\sqrt{1 + \frac{4\mu D}{v^2}} \quad (5)$$

In out experimental setup, in the interval of

$$0 < t < t_0$$

there was no production ($\gamma = 0$), and there was no initial concentration of Mn in the column ($C_i = 0$), too. With these boundary conditions, the following equation describes 1D transport (BTC)

$$BTC = c(x,t) = \frac{C_0}{2}\left\{e^{\left[\frac{\left(v-v\sqrt{1+\frac{4\mu D}{v^2}}\right)x}{2D}\right]}erfc\left[\frac{Rx-v\sqrt{1+\frac{4\mu D}{v^2}}t}{2\sqrt{DRt}}\right] + \right.$$

$$\left. e^{\left[\frac{\left(v+v\sqrt{1+\frac{4\mu D}{v^2}}\right)x}{2D}\right]}erfc\left[\frac{Rx+v\sqrt{1+\frac{4\mu D}{v^2}}t}{2\sqrt{DRt}}\right]\right\} \quad (6)$$

where erfc is the complementary function of Gauss error function

$$erfc(x) = 1 - erf(x) = \frac{2}{\sqrt{\pi}}\int_x^\infty e^{-t^2}dt \quad (7)$$

By the elimination of irreversible reaction rate constant, the *Equation 6* simplifies to

$$C = C_0 \left[\frac{1}{2} erfc\left(\frac{Rx-vt}{2\sqrt{DRt}}\right) + \frac{1}{2} e^{\frac{vx}{D}} erfc\left(\frac{Rx+vt}{2\sqrt{DRt}}\right)\right] \tag{8}$$

as given by Ogata and Banks (1961).

We solve *Equation 1* for instantaneous injection of pollutant mass ΔM, at the point x = 0 and in time t = 0. This type of initial condition can be expressed by means of Dirac-function (Kinzelbach, 1986; Kovács, 2004)

$$C_\delta(x,0) = \frac{M}{n_0 AR}\delta(x) \tag{9}$$

where A is cross-sectional area of flow medium and Dirac-function δ(x) is defined as

$\delta(x) = 0$, when $x \neq 0$,

and

$\int_{-\infty}^{+\infty} \delta(x)dx = 1$, when $x = 0$.

When $C(\pm\infty, t) = 0$, the solution of *Equation 9* is

$$IMP = C(x,t) = \frac{M}{2An_0R\sqrt{\frac{\pi\alpha_L vt}{R}}} e^{\left(-\frac{\left(x-\frac{vt}{R}\right)^2}{\frac{4\alpha_L vt}{R}}\right)} e^{(-\mu t)} \tag{10}$$

where n_0 is effective porosity and α_L is longitudinal dispersivity.

To derive transport parameters fitting analysis of OriginPro 8.6.0 of OriginLab Co was used. In the following, *Equation 6, Equation 8* and *Equation 10* are used to determine the transport parameters of MWDM.

3. RESULTS

Three parameters were derived from experiments: retardation factor, longitudinal dispersivity (by neglecting the molecular diffusion, it can be calculated from hydrodynamic dispersion), and irreversible reaction rate constant *(Figures 3–4)*.

Longitudinal dispersivity is not generally usable information because this parameter only just characterizes the investigated scale of the model. This parameter will be higher in the mine waste dumps because the ratio of the spatial extension of the

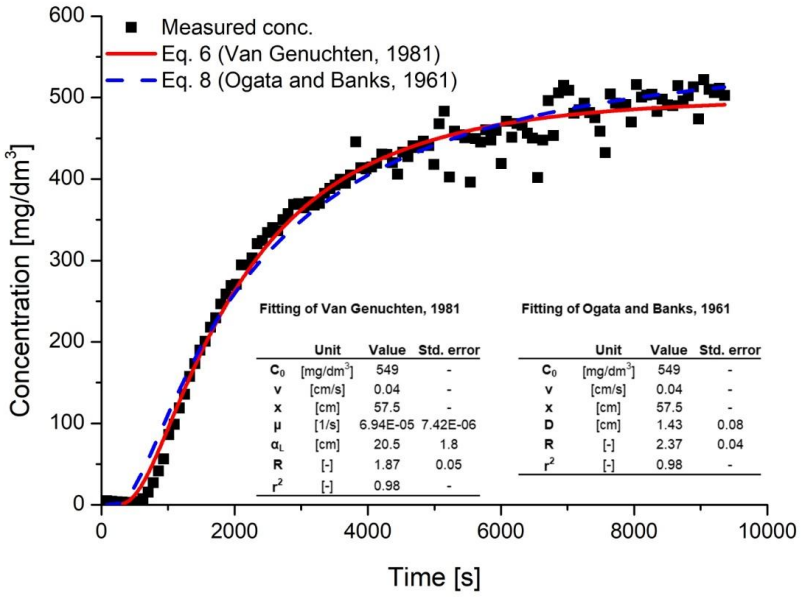

Figure 3
Results of Mn solution breakthrough test

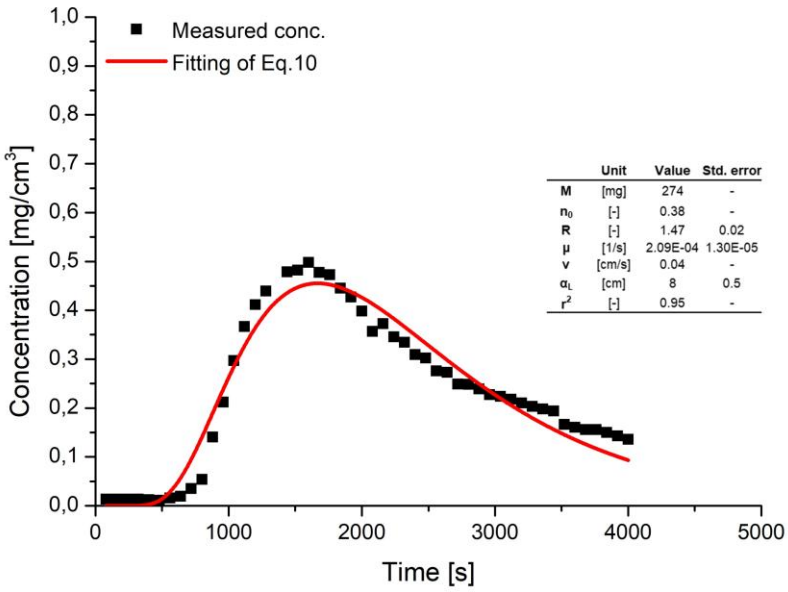

Figure 4
Result of Mn impulse test

model and longitudinal dispersivity changes between 10 : 1 and 100 : 1 (Kinzelbach, 1986), but it could be higher than 100 : 1 in larger scales (Kovács and Szanyi, 2005). The values of longitudinal dispersivity in the breakthrough test and impulse test are 20.5 cm and 8 cm, respectively.

The retardation factor describes the adsorption of the component in the system. The retardation factor of Mn in the MWDM is similar in both measurement setups [R_{BTC} = 1.87 (*Figure 3*, Van Genuchten solution) and R_{BTC} = 2.37 (*Figure 3*, Ogata and Banks solution), R_{IMP}=1.47 *(Figure 4)*]. The difference experienced between the resultant parameters of Van Genuchten solution and Ogata and Banks solution of breakthrough test comes from the neglection of irreversible reaction rate in *Equation 8* (Ogata and Banks solution). This difference highlights how important to enumerate the possible processes during heavy metal transport.

The value of the irreversible reaction rate constant differs in the two experiments; there is an order of magnitude difference between the result of the breakthrough test ($\mu_{BTC} = 6.94 \cdot 10^{-5}$ 1/s, (*Figure 3*, Van Genuchten solution) and the impulse test [$\mu_{IMP} = 2.09 \cdot 10^{-4}$ 1/s *(Figure 4)*]. Because the determination of transport parameters is based on the same fitting analysis, the difference in irreversible reaction rate constant is probably related to the different sensitivity of transport equations (*Equation 6* and *Equation 10*) for this parameter.

4. DISCUSSION

In case of high retardation factor the breakthrough of the heavy metal is slower in the investigated material. According to the definition of retardation factor values greater than unity indicate sorption (Amacher et al., 1986). Fonseca et al. (2011) found retardation factors for Zn R_{Zn} = 6 and for Cu R_{Cu} = 49 in loamy sand soil during mono-metal transport conditions. To compare the Mn retardation factor in our experiment the low values indicate low affinity of the component to adsorb, thus Mn can be considered a mobile element in the MWDM.

Although the adsorption of Mn is not determinant in the transport process its irreversible reaction rate constant significantly modifies the heavy metal concentration in the effluent fluid. In a column test aiming determination of the transport parameters of a solute, it is better to investigate first the possibility of irreversible material loss because it can cause significant differences between the determined parameters of the impulse test and breakthrough test. According to our investigation, it seems the impulse test is more sensitive on change of irreversible reaction rate constant compared to the breakthrough test but to prove this assumption further sensitivity analysis is needed.

ACKNOWLEDGEMENT

The research presented in the article was carried out within the framework of the Széchenyi Plan Plus program with the support of the RRF 2.3.1 21 2022 00008 project.

REFERENCES

Amacher, M., Kotuby-Amacher, J., Selim, H., Iskandar, I. (1986). Retention and release of metals by soils — Evaluation of several models. *Geoderma*, 38 (1–4), pp. 131–154, https://doi.org/10.1016/0016-7061(86)90011-X

Anju, M., Banerjee, D. (2010). Comparison of two sequential extraction procedures for heavy metal partitioning in mine tailings. *Chemosphere*, 78 (11), pp. 1393–1402, https://doi.org/10.1016/j.chemosphere.2009.12.064

Balla, L. (ed.) (1987). Rudabányai vasércbányászat. Bányabezárási dokumentáció (Iron ore mining at Rudabánya. Mine closure documentation). – Manuscript, Heavy Industrial Technical University, Miskolc, 441 p. (in Hungarian).

Bodor, S., Polgári, M., Szentpétery, I., Földessy, J. (2016). Microbially mediated iron ore formation, Silicic Superunit, Rudabánya, Hungary. *Ore Geology Reviews*, 72 (1), pp. 391–401, https://doi.org/10.1016/j.oregeorev.2015.08.005

Czinkota, I., Issa, I., Rétháti, G., Kovacs, B. (2006). Determination of the Behaviour and the Transport Parameters of Chromium in Soil-Water Systems. *Agrokémia és Talajtan*, p. 55, http://doi.org/10.1556/Agrokem.55.2006.1.31

Fonseca, B., Figueiredo, H., Rodrigues, J., Queiroz, A., Tavares, T. (2011). Mobility of Cr, Pb, Cd, Cu and Zn in a loamy sand soil: A comparative study. *Geoderma*, 164 (3–4), pp. 232–237, https://doi.org/10.1016/j.geoderma.2011.06.016

Földessy, J., Németh, N., Gerges, A. (2010). Preliminary results of the re-exploration of the Rudabánya base metal ore deposit. *Bulletin of the Hungarian Geological Society*, 140 (3), pp. 281–292.

Freeze, R., Cherry, J. (1979). *Groundwater.* Englewood Cliffs, Prentice-Hall Inc.

Heltai, Gy., Győri, Z., Fekete, I., Halász, G. Kovács, K., Takács, A., Boros, N., Horváth, M. (2018). Longterm study of transformation of potentially toxic element pollution in soil/water/sediment system by means of fractionation with sequential extraction procedures. *Microchemical Journal*, 136, pp. 85–93. https://doi.org/10.1016/j.microc.2017.01.026

Kang, J.-K., Lee, S.-C., Jang, H.-Y., Lee, C.-G., Kim, S-B. (2021). Nitrate removal by quaternized mesoporous silica gel in ternary anion solutions: Flow-through column experiments and artificial neural network modeling. *Journal of Water Process Engineering*, 41, p. 102067, https://doi.org/10.1016/j.jwpe.2021.102067

Kinzelbach, W. (1986). *Groundwater modelling- An introduction with sample programs in BASIC.* Amsterdam, Elsevier.

Kovács B. (2004). *Hidrodinamikai és transzportmodellezés I.* Miskolc, GÁMA-GEO Kft., p. 159.

Kovács B., Szanyi J. (2005). *Hidrodinamikai és transzportmodellezés (Processing MODFLOW és Surfer for Windows környezetben) II.* Miskolc, GÁMA-GEO Kft.

Kresic, N. (2007). *Hydrogeology and Groundwater Modeling.* 2nd ed. Boca Raton, CRC Press.

Moulatlet, G. M., Yacelga, N., Rico, A., Mora, A., Hauser-Davis, A. A., Cabrera, M., Capparelli, M. V. (2023). A systematic review on metal contamination due to mining activities in the Amazon basin and associated environmental hazards. *Chemosphere*, 339, 139700, https://doi.org/10.1016/j.chemosphere.2023.139700

Mufalo, W., Tangviroon, P., Arima, T., Igarashi, T., Ito, M., Sato, T., Noto, K., Kawashima, T., Nyambe, I., Nakata, H., Nakayama, S., Ishizuka, M. (2023). Immobilization of Pb and Zn leached from mining residue materials in Kabwe, Zambia: Performance of calcined dolomite in column experiments. *Journal of Geochemical Exploration*, 249, 107209. https://doi.org/10.1016/j.gexplo.2023.107209

Nemeth, N., Földessy, J., Kupi, L., Iglesias, J. (2013). Zn-Pb mineralization types in the Rudabánya ore bearing complex. *Carpathian Journal of Earth and Environmental Sciences*, 8 (1), pp. 47–58.

Ogata, A., Banks, R. B. (1961). *A Solution of the Differential Equation of Longitudinal Dispersion in Porous Media.* US Geological Survey Professional Papers, No. 34, p. 411-A.

Sharma, H. D., Reddy, K. (2004). *Geoenvironmental engineering: site remediation, waste containment, and emerging waste management technologies.* Hoboken, John Wiley and Sons.

Stumm, W., Morgan, J. (1996). *Aquatic Chemistry, Chemical Equilibria and Rates in Natural Waters.* 3rd ed. New York, John Wiley and Sons.

Szentpétery, I., Less, G. (1986). *Geology of the Aggtelek-Rudabánya Mts. Explanations to the 1:25000 Scale Geological map of the Aggtelek-Rudabánya Mts.* Budapest, Hungarian Geological Institute.

Tan, K. (1995). *Soil sampling, preparation, and analysis.* Boca Raton, CRC Press.

Tomiyama, S., Igarashi, T. (2022). The potential threat of mine drainage to groundwater resources. *Current Opinion in Environmental Science and Health*, 27, 100347, https://doi.org/10.1016/j.coesh.2022.100347

Van Genuchten, M. (1981). Analytical solutions for chemical transport with simultaneous adsorption, zero-order production and first-order decay. *Journal of Hydrology*, 49, pp. 213–233, https://doi.org/10.1016/0022-1694(81)90214-6

Zheng, X., Lu, Y., Xu, J., Geng, H., Li, Y. (2023). Assessment of heavy metals leachability characteristics and associated risk in typical acid mine drainage (AMD)-contaminated river sediments from North China. *Journal of Cleaner Production*, 413, 137338, https://doi.org/10.1016/j.jclepro.2023.137338

Zou, H., Ren, B. (2023). Analyzing topsoil heavy metal pollution sources and ecological risks around antimony mine waste sites by a joint methodology. *Ecological Indicators*, 154, 110761. https://doi.org/10.1016/j.ecolind.2023.110761.9

Geosciences and Engineering, Vol. 12, No. 2 (2024), pp. 37–44.
https://doi.org/10.33030/geosciences.2024.02.003

ON THE IMPACT OF HYDROCARBON CONTAMINATION ON COMPACTION AND PLASTICITY BEHAVIOR OF SANDY CLAY SOIL CASE STUDY: NORTHEAST HUNGARY

SIRINE TRABELSI[1*], NOÉMI SZÁSZ[2], ANDREA TÓTH[3]
[1, 2, 3]*Institute of Water Resources and Environmental Management*
University of Miskolc
[1, 2, 3]*National Laboratory for Water Science and Water Security*
[1*]*trabelsi.sirine@student.uni-miskolc.hu*
[2]*noemi.szasz@uni-miskolc.hu*
[3]*andrea.toth@uni-miskolc.hu*
[1]*https://orcid.org/0009-0008-8251-270X*
[2]*https://orcid.org/0000-0002-6433-9885*
[3]*https://orcid.org/0000-0002-7353-4367*

Abstract: This study investigates the behavior of hydrocarbon-contaminated soils, using Atterberg tests and Modified Proctor Tests (MPT) conducted on sandy clay soil samples. By exposing the soil to higher artificial contamination percentages than has been reported in the literature, our approach gives a further comprehensive analysis and provides a complex interpretation of the contamination process and its impact on compaction. The oil contamination led to an increase in the plastic limit and a decrease in the plasticity index. It also influenced the compaction behavior, resulting in a decrease in the maximum dry density. The analysis emphasizes the significance of considering higher contamination levels for a more robust understanding with implications for diverse engineering applications.

Keywords: *Atterberg tests, compaction, contamination, hydrocarbon, MPT, soil*

1. INTRODUCTION

Industrialization and increased reliance on hydrocarbon-based fuels have brought forth significant environmental concerns. As hydrocarbons, the primary constituents of crude oil, infiltrate the soil matrix, they trigger a cascade of transformations in its physical and chemical properties. Under the force of gravity, the oil that had spilled or was rushing down to the groundwater. The oil on its route has partially saturated the soil. The liquid migrated within the capillary zone and spread horizontally after it reached the groundwater (Shroff, 1997). As a result, they have the potential to cause irreversible harm to the environment.

Although oil spills have decreased in recent years, the long-term impact of the previously recorded oil spill still affects some productive and vulnerable compartments of the ecosystem (Chen et al., 2012).

When the environment is contaminated by a fluid substance, clay soil, which is electrochemically active, is most impacted (Rehman et al., 2017). An oil spill could cause pollution on land or in water. Crude oil pollution on land is influenced by several variables, such as the soil's permeability, adsorption capacity, and partition coefficient (Nudelman et al., 2002).

This matter been a long-standing concern in Western countries for 30-40 years, while Hungary began addressing it only after the end of the Soviet era in 1989. The Soviet occupation from 1945–1989 left behind numerous barracks and military bases, serving as significant sources of pollution. After the withdrawal of Russian military troops, these areas, such as old Soviet barracks in Szentendre turned factory sites, continued to exhibit contamination, particularly with chlorinated hydrocarbons. This can be investigated with geophysical surveys such as engineering geophysical soundings (EGS) and direct-push geophysical measurements (Háromkő Bt., 2018).

In addition, contaminated soils exhibit a distinctive profile of lower maximum dry density and higher optimal moisture content, indicative of a compromised compaction effectiveness (Adejumo, 2012). When compared to uncontaminated soils, contaminated soils typically exhibit decreased maximum dry density and higher optimal moisture content, which indicates less effective compaction (Safehian et al., 2018). By increasing oil contamination in clayey soil, oil pollution usually decreases the permeability, strength, and Atterberg limits (Khamehchiyan et al., 2007).

The objective of this study is to perform a series of laboratory tests such as Modified Proctor Test (MPT) and Atterberg Limits tests to determine the impact of high percentages of hydrocarbon contamination on geotechnical properties of artificially sandy clay soil. These properties include Atterberg limits and compaction curves provide valuable insights into the compaction and the plasticity behavior.

2. MATERIALS AND METHODS

The materials used in this study are soil samples and a synthetic brake fluid. Disturbed soil sample was collected from Mályi quarry located in the northeast of Hungary. Particle size distribution analysis, Atterberg limit and compaction properties were determined. The soils are then classified as medium plasticity, lean clay according to European standard (Eurocode7) and Hungarian standard (MSZ) classification. *Table 1* shows the summary of basic properties.

Table 1

Summary of basic properties of the investigated soil

Natural water content [%]	Plasticity index (IP) [%]	Organic matter content [%]
12.79	17.69	2.70

On the other hand, X-Ray Diffraction (XRD) analysis is a potent method used to examine the mineralogical composition of soil samples. By identifying and measuring the mineral phases that are present in soil, XRD techniques offer important

insights about the soil's origin. The dominating minerals can be identified by researchers by examining the X-ray diffractograms. *Table 2* provides a summary of the outcomes.

Table 2

XRD results for the investigated soil.
[The values are expressed in percentages (%)]

Quartz	**Muscovite 2M1**	**Chlorite IIb**	**Kaolinite**	**Calcite magnesian**	**Dolomite**	**Albite**
35.171	13.761	1.989	3.836	2.277	1.911	6.304
Illite 2M1	**i/sm 11A**	**Smect 14A**	**Microcline**	**Biotite 1M**	**Goethite**	**Vermiculite**
22.311	5.729	1.299	0.869	0.099	2.904	1.540

The following sample preparation procedure was followed. After particle size classification, each sample was dried in oven at 105 °C. Then the clay samples were mixed with clean sand in a ratio of 80 : 20 (80% clay and 20% sand) by weight. This mixing strategy was chosen to facilitate laboratory testing methods and enhance the workability of the clay soil samples during the Proctor compaction tests resulting in more accurate and effective testing. The testing program includes Atterberg limits and the compaction tests. The tests were performed on clean samples and then repeated for contaminated ones.

3. RESULTS AND DISCUSSION

The following section provides an analysis of the data collected from compaction tests and the Atterberg limits test.

3.1. Compaction test results

The standard Proctor test: the soil mass is put and compacted in three layers inside a 944 cm^3 volume cylindrical mold and a diameter of 101.6 mm. A hammer 2.5 kg weight is dropped 25 times from a height of 30 cm to compress each layer. (Knappett et al., 2012). In the Modified Proctor Test *(Figure 1)* according to MSZ-EN 13286-2, the procedure involves meticulous steps, it's the modified version of the Standard Proctor Test that uses a heavier compaction effort and a larger mold.

This laboratory test typically includes compacting soil with a known moisture content into a cylindrical mold while applying a controlled amount of compaction force. It was developed to better simulate the compaction effort of heavy machinery used in the field. The soil mass is put and compacted into five layers inside a 944

cm^3 volume cylindrical mold and a diameter of 101.6 mm. A hammer of 4.54 kg is dropped 25 times from a height of 457 mm to compress each layer.

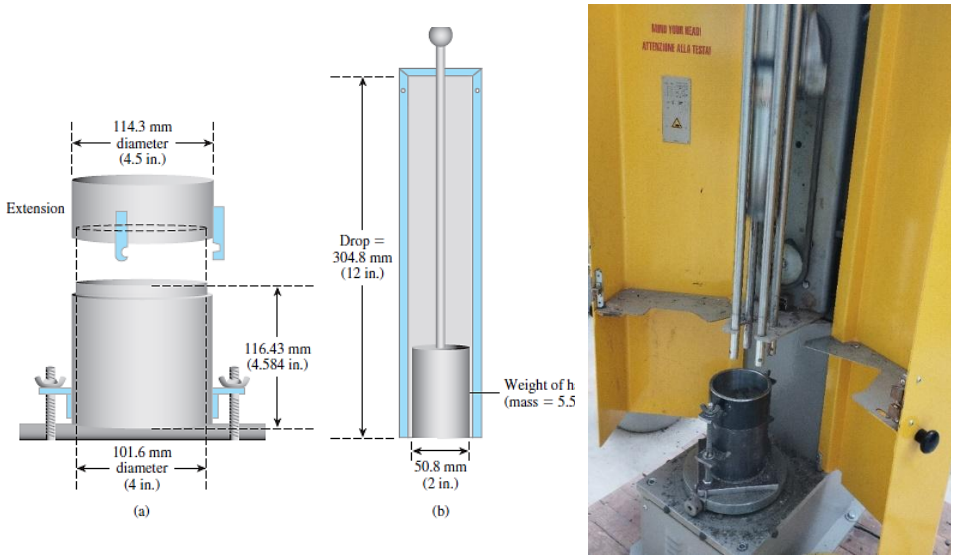

Figure 1

Schematic picture of the standard proctor test [Das and Sobhan, (2013)] (left) and compacting the samples under laboratory conditions (right)

The water content is determined by the test, and the dry density of the compacted sample is calculated according to *Equation 1*:

$$\rho_d = \frac{1}{1+\frac{\omega\%}{100}} * \rho_n \quad (1)$$

where ρ_n bulk density [g/cm^3], $\omega\%$ water content of the sample [%], ρ_d dry density in [g/cm^3].

Moisture content and dry density are recorded for each compaction effort, enabling the establishment of a compaction curve (Proctor, 1933). This section of the study compares the compaction behavior of samples of clean soil with those that were previously contaminated with oil brake fluid. In addition, two levels of contamination were applied to the soil samples, with 30% and 50% (by volume) of brake oil added to the water used to moisten the soil.

These levels of contamination represent the typical moderate to extremely high contamination levels found in contaminated environments to approximate extreme real-world scenarios, such as industrial spills or prolonged exposure to hydrocarbons. By testing these elevated levels, the study aims to expand scientific understanding of the impact of substantial oil pollution on soil behavior.

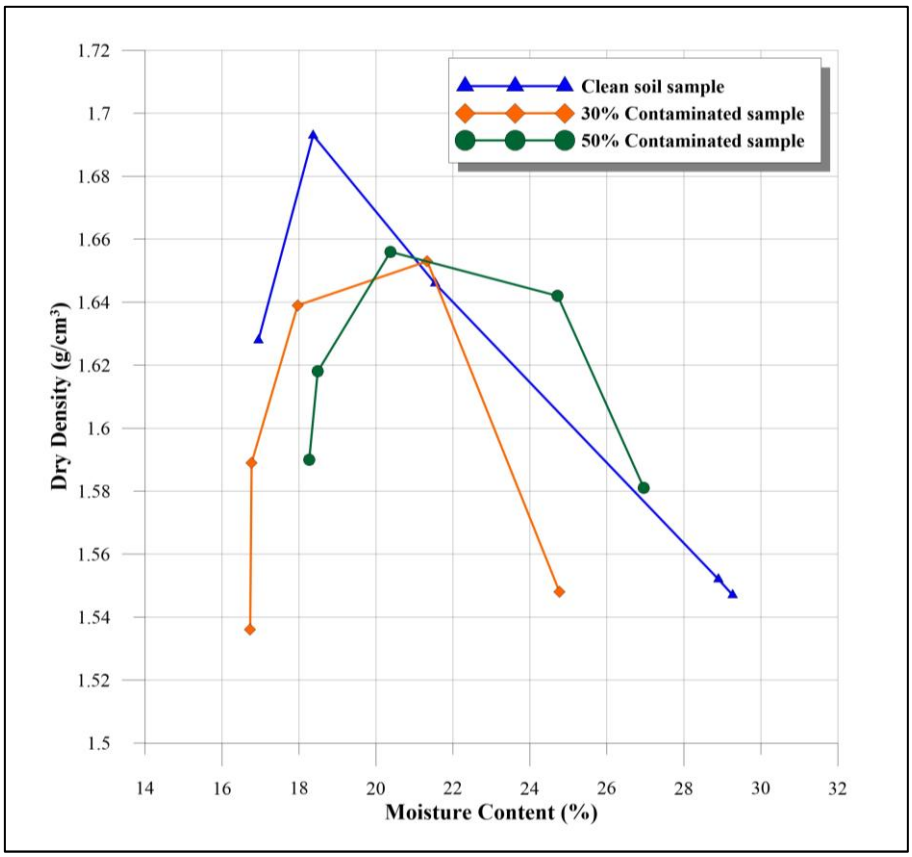

Figure 2
Compaction curves of the investigated soil sample

The maximum dry density and optimum water content of the contaminated and clean samples differ noticeably, according to study. When brake oil is added, the optimum water content increases by around 3%, suggesting that a larger moisture content is required to achieve optimal compaction. Simultaneously, data analysis reveals a marginal reduction in the maximum dry density in the presence the contamination. The maximum dry densities of the contaminated clay samples are slightly lower than those of the clean clay samples. These results shown in *Figure 2* highlight the influence of brake oil on the compaction properties of the soil, highlighting the necessity of cautious thought and modifications in construction methods while working with contaminated soil.

3.2. Atterberg limit test

Atterberg limits provide critical information about the consistency and plasticity of soils. The limits are described as certain moisture levels at which the soil changes from one condition to another, such as from liquid to plastic to solid. The tests were

conducted in accordance with MSZ EN ISO 14688-2 and MSZ 14043-2 standards, and the outcomes are shown in *Table 3*.

Table 3

Atterberg limits results of the investigated soil

	clean	**30 w/w% contamination**	**50 w/w% contamination**
plastic limit [%]	23.05	28	33.1
liquid limit [%]	47.7	43.9	43.7
plasticity index [%]	24.64	15.9	10.6
consistency index [-]	1.425	1.62	1.63

When brake oil is added, the Plastic Limit (WP) increases, as measured by looking at the 50% polluted soil sample, which is 33.1% compared to 23.05% for the clean sample. This 10% increase suggests that contamination reduces the soil's plasticity making it less prone to reach the semisolid state at lower moisture contents. Comparably, the 50% contaminated sample's Plasticity Index (PI) drops from 24.645% for the clean sample to 10.6%, suggesting a 14% decrease in the range of moisture content at which the soil exhibits plastic behavior. By comparing the 50% and 30% contaminated samples, the contaminated samples. Liquid Limit (WL) values are found to be marginally lower than those of the clean sample. This indicates that a larger brake oil concentration can increase the amount of moisture needed for the clay to become liquid.

4. CONCLUSIONS

The oil contamination has been found to affect the compaction behavior, leading to a decrease in the maximum dry density and an increase in the optimum moisture content in most cases. By combining plasticity characteristics and compaction behavior, we can understand how oil contamination impacts the overall engineering properties of sandy clay soil. The increased plasticity limits and reduced plasticity indexes, in conjunction with the decrease in maximum dry density and the increase in optimum moisture content, indicate that hydrocarbon contamination reduces the soil's compaction potential and alters its behavior.

The presence of hydrocarbons can interfere with the soil particles' ability to aggregate and rearrange, affecting the compaction process. This can be explained by disruption of Particle Arrangement. In other words, oil contamination tends to lubricate the soil particles, reducing inter-particle friction and making it more difficult for the particles to interlock during compaction. This results in a looser arrangement of soil particles, leading to a decrease in the maximum dry density.

To improve this study in general, several recommendations can be implemented. It is crucial to ensure an adequate sample size and replication for each treatment group to enhance statistical power and account for natural variability. Proper data analysis using appropriate statistical methods such analysis of variance (ANOVA),

along with thorough interpretation and discussion of results, is necessary to derive meaningful conclusions.

ACKNOWLEDGMENT

The research presented in the article was carried out within the framework of the Széchenyi Plan Plus program with the support of the RRF-2.3.1-21-2022 00008 project.

REFERENCES

Adejumo, T. Elisha (2012). Effect of Crude Oil Contamination on the Geotechnical Properties of Soft Clay Soils of Niger Delta Region of Nigeria. *Electronic Journal of Geotechnical Engineering*, 17, pp. 1929–1938.

Braja, D. M., Sobhan, K. (2013). *Principles of Geotechnical Engineering.* SI Edition. 8th ed. Andover, UK, Cengage Learning.

Chen, P., Li, Y., Lan, G., Liu, B., Zhou, H. (2012). Oil spills detection and monitoring using airborne thermal infrared remote sensing in Dalian Xingang oil pipeline explosion, *Proceedings of the 2012 2nd International Conference on Remote Sensing, Environment and Transportation Engineering*, Nanjing, China, 01–03 June 2012. https://doi.org/10.1109/RSETE.2012.6260647

Das, B. M., Sobhan, K. (2013). *Principles of Geotechnical Engineering.* SI Edition. 8th ed. Andover, UK, Cengage Learning.

Habib-ur-Rehman, Abduljauwad, S. N., Akram, T. (2007). Geotechnical Behavior of Oil Contaminated Fine-Grained Soils. *Electronic Journal of Geotechnical Engineering EJGE*, Vol. 12, Bundle A, 0720.

Bucsi Szabó L., Ungvári O., Nagy G. (2018) Veszélyeztetett vízbázis vizsgálata, Szentendre (Szentendre, protection of water resources). Háromkő Bt., Miskolc, pp. 2–4., (in Hungarian).

H. Safehian, A. M. Rajabi, H. Ghasemzadeh (2018). Effect of diesel-contamination on geotechnical properties of illite soil. *Engineering Geology*, 241 (2018), pp. 55–63. https://doi.org/10.1016/j.enggeo.2018.04.020

Khamehchiyan, M., Charkhabi, A. H., Tajik, M. (2007). Effects of crude oil contamination on geotechnical properties of clayey and sandy soils. *Engineering Geology*, 89 (3–4), pp. 220–229. https://doi.org/10.1016/j.enggeo.2006.10.009

Knappett, J. A., Craig, R. F. (2011). *Craig's Soil Mechanics.* 8th ed. London, Spon Press.

Nudelman, N. S., Rios I. S., Katusich, O. (2002). Fate of the oil residuals in Patagonian soils effects of the environmental exposure time. *J. Environ. Assessment Remediation*, Vol. 3, pp. 1–8.

Proctor, R. R. (1933). Fundamentals principles of soil compaction. *Engineering News-record*, 111 (9), 245–248.

Shroff, A. V. (1997). *Properties of oil contaminated soil and their remedial methods by admixtures – A case study.* I.G.C.-1997. Vadodara, India, pp. 399–400.

https://utugyilapok.hu/cikkek/tomorsegi-fok-atszamitasa-az-egyszerusitett-es-modositott-proctor-vizsgalatok-kozott/, (accessed on 13 January 2025), in Hungarian

Geosciences and Engineering, Vol. 12, No. 2 (2024), pp. 45–56.
https://doi.org/10.33030/geosciences.2024.02.004

DIRECT POROSITY MEASUREMENT USING SINGLE CHAMBER GAS PYCNOMETERS

ROLAND DÓCS[1]*, ISTVÁN SZUNYOG[2]
[1]**Mining and Energy Institute of University of Miskolc Hungary;*
roland.docs@uni-miskolc.hu
[2]*Mining and Energy Institute of University of Miskolc Hungary*
istvan.szunyog@uni-miskolc.hu
[1]*https://orcid.org/0000-0002-1456-2990*
[2]*https://orcid.org/0009-0007-6289-3210*

Abstract: During porosity measurements, error most certainly originates from the incorrect determination of the samples total geometrical volume. This uncertainty will affect all porosity measurement procedures with greater degree on the indirect methods. However, there is a solution where the effect of the sample volume can be eliminated. If both the matrix and pore volume of the sample is measured the porosity can be calculated using those values instead of the bulk and pore volumes. The two-chamber gas pycnometer is the most used method for determining the matrix volume. The procedure applies Boyle's principle which can also be used to determine the pore volume directly using a single chamber construction, if the difficulties discussed in this article are solved.

Keywords: *porosity, reservoir, petrophysics, pycnometer*

1. INTRODUCTION

Porosity is considered one of the most basic yet most important petrophysical parameter of hydrocarbon reservoirs, as it describes the ratio of the void volume to the total volume of the porous rock (Dotson, Slobod, McCreery, & Spurlock, 1951). Thus, describing the volume fraction where fluids could accumulate in the rock. Numerous procedures were developed throughout the years (Lawrence & David, 2015) for the estimation/measurement of porosity from which the most reliable ones are those of laboratory measurements performed on samples taken from the reservoir.

Some authors categorize these measurements into two groups namely direct and indirect porosity methods. From which those that measure the pore volume are the direct and the ones measuring the matrix volume or true solid volume are the indirect methods. As mentioned previously the total volume, also referred to as the bulk or geometrical volume of the sample, consists of two parts. The void volume where no material is present and the matrix where the material mass is located. Porosity therefore can be calculated if either of two of the three volumes is determined.

In result at least two individual procedures are required to specify the porosity of a given material. Most laboratories measure the petrophysical properties such as permeability, relative permeability, rock mechanics… etc. on cylindrical shaped sample

plugs. Therefore, in convenience the total volume is measured with simply digital calipers while a volume measurement method is used for either the matrix or the pore volume of the sample (Anovitz & Cole, 2015). In most laboratories for this purpose two chamber gas pycnometers (API, 1998) are applied due to their accuracy (~0,01% for all sample volume range) and the simple fact that there is no risk of damaging the sample in any means which is truly important for sample integrity. However, traditional gas pycnometers measure the true material volume of the sample rather than its pore volume.

In result one must ask how reliable and accurate the porosity of the sample will be the manually measured total volume of the sample is used in both the nominator and denominator of the equation. One may ask, ff this uncertainty is known to exist why no other total volume measurement are used instead?

Although in the industry several well-established measurement methods exist both for pore as well as matrix volume. On the other hand, for total volume measurement this unfortunately is not as simple. In the past the total volume of the samples was measured using the nonwetting properties of mercury with either a Westman Balance applying Archimedes' law or a pycnometer (Luffel & Howard, 1988). But due to the toxic nature of the material and the technical difficulties regarding these methods, total volume measurements of such forms are not very popular nowadays in the petroleum industry.

Other practices such as imbibition or buoyancy methods could be combined with two chamber gas pycnometers for porosity determination; however, the accuracy of these methods is nowhere near that of a gas pycnometer. And would not present better results than the manual measurements done with digital calipers. Also, in the case of strong oil wet rocks and unconventional rock materials are not very applicable due to the high pressures necessary for the saturation to reach and stay at 100%.

On the other hand, the other two pore volume measurement methods, namely gas adsorption and mercury intrusion porosimeters (Jimmy, Reza, Tobias, & Mohammad, 2020) would certainly have the necessary accuracy to be implemented with gas pycnometers for porosity measurement. Also, the above-mentioned pore size and wetting properties would also not be a concern due to the nature of the procedures. Unfortunately, due to the presence of another problem, these methods are also not the perfect solution.

For gas absorption and mercury injection porosimeters a usual sample size is somewhere between 0,5–1,5 cm^3 while an average sample plug (for example 1.5" diameter) has a total volume between 60–80 cm^3 depending on the final length after cutting. In most laboratories, however, the gas- and mercury intrusion pycnometers are the most frequently used instruments for porosity measurement. In these cases, normally the porosity of the sample plug is determined by caliper and gas pycnometer and the mercury pycnometer serves as an additional method for pore volume measurement as well as serving other important properties (pore size distribution, sub surface area, grainsize distribution…etc.).

In some cases, the porosity of the small samples is considered to that corresponding to the sample plug since the small samples are produced from the access cut

material of those. If so, the small samples porosity can be determined at a high accuracy since mercury intrusion porosimetry measures the true pore volume of the sample and for the matrix volume a traditional gas pycnometer can be used.

For samples of homogenous nature this principal could be valid but natural rock formations could never be considered as such. Many publications and self-experiences show that is not as simple and this is never truly the case. This causes many petrophysical laboratories to not bother with porosity determination of the small samples and such measurements are primarily used for additional information.

Another solution for structural presentation hence volume determination is using NMR, unfortunately these types of equipment's are not very common due to their high cost and also limitations of sample volume. Despite their higher resolution and additional information on the structure of the pore system the implementation of mercury porosimetry is more approved.

In result during the research, it was clear that the porosity of a sample plug could only be measured with high accuracy if some other pore volume measuring method which not yet been mentioned could be used in combination of the traditional gas pycnometer.

In some literature an altered configuration of the gas pycnometer was presented (API, 1998) where the pore volume is measured rather than the matrix one using a Hassler type core holder (Rajib, Madland, Fred, & Aksel, 2012). One must then ask why this method is not used in most cases. The single chamber gas pycnometer has several difficulties which need to be addressed to perform the measurement which hindered its spread in the industry. These difficulties and their solutions will be covered in detail.

2. MATERIALS AND METHODS

2.1. Effect of total volume error on porosity

As shown in *Equation 1* during porosity (ϕ) calculation there are three individual volumes of the porous sample namely the pore (V_P), the true solid (V_S) and the total also referred to as apparent volume (V_T). As mentioned previously if either two of the three are measured porosity can be calculated.

$$\phi = \frac{V_P}{V_T} = \frac{V_T - V_S}{V_T} \tag{1}$$

Knowing that during porosity measurements the highest error always comes from the uncertainty of the total volume, its effect can be clearly seen to be more dominant in indirect methods. Unfortunately, during the sample preparation process total symmetry cannot be achieved hence the caliper method is not always reliable enough. Another solution is the Westman balance where the buoyant force required to totally submerge the sample into mercury is determined which if done correctly could give good results but is only used for irregular shape samples due to its complexity and potential high error. Also, for rocks with vuggy secondary porosity the removal of mercury on itself is a huge problem.

Let us give a simple example of how this error effects porosity. Let us consider a theoretical sample of exactly 100 cm^3 of total volume where the total void volume is 25 cm^3 resulting in 25% porosity.

To observe how the uncertainty of the geometric volume affects the value of porosity let's assume a positive and negative 5% error *(Table 1)* while using the correct pore and matrix volumes.

Table 1

The divergence in porosity due to the error of the total volume

Correctly measured values		**V_{T_actual}**	**100 cm^3**
V_{P_actual}	25 cm^3	ϕ_{actual} = 0,2500	
V_{S_actual}	75 cm^3		
Presenting 5% Error into the measurement of the total volume			
$V_{T(-5\%)}$	95 cm^3	$V_{T(+5\%)}$	105 cm^3
$\phi_{calculated}$ from V_{P_actual}	0.2632	$\phi_{calculated}$ from V_{P_actual}	0.2381
$\phi_{calculated}$ from V_{S_actual}	0.2105	$\phi_{calculated}$ from V_{S_actual}	0.2857
Error of porosity at $V_{T(-5\%)}$		**Error of porosity at $V_{T(+5\%)}$**	
From $V_{P\_calculated}$	0.0526	From $V_{P\_calculated}$	–0.0476
From $V_{S\_calculated}$	–0.1579	From $V_{S\_calculated}$	0.1429

During direct porosity measurements the error of the geometry appears with the same weight in the calculated porosity. Unfortunately, this cannot be said for the indirect methods where the total volume of the sample is used in both the nominator and in the dominator of the equation.

Therefore, the most reliable solution is to measure the true solid and the pore volumes directly and calculate the total volume as the sum of these values. For which in most petrophysical laboratories the gas pycnometer and the mercury intrusion pycnometer are used.

2.2. The discussion of the existing methods for matrix and pore volume determination

As mentioned previously in the industry the two most accepted procedures for porosity determination are the gas- and mercury intrusion pycnometers from which the previous is a direct while the latter is an indirect method. Both methods are favored over each other for different reasons of which the most important factors are addressed in *Table 2*.

If the two methods are taken into consideration the only positive regarding the mercury pycnometer is the fact that it provides much more information on the samples pore structure above the total porosity. Such as pore size distribution which gives a good picture of how the reserve will perform during production. The main problem however is that the mercury samples are much smaller than the sample plugs which are used for all other petrophysical measurements. For this cause the results of this method are not suggested by us to be used with other data of the sample plug for porosity calculation purposes.

Table 2

Pros and cons of the different pycnometers

Point of interest	Gas Pycnometer	Mercury intrusion pycnometer
Maximum sample size	Approximately 85 cm^3	Approximately 1 cm^3
Measurement time	From 15 minutes to several hours	Approximately 1 hour
Additional information	No additional information from measurement	Pore size distribution, grainsize distribution, Surface area, and more
Pollution of the sample	No effect	After measurement sample is unusable for other procedures
Health concerns	No effect	Highly toxic material and waste

The question can be asked is it possible to measure the cylindrical samples pore volume directly with any existing method? Before an answer could be given, the method for matrix volume measurement first must be discussed in detail.

The apparatus presented in *Figure 1* is the most used gas pycnometer in the industry. The measurement uses Boyle's law which states that at isothermal condition the new volume (at the new pressure) of a known quantity of gas can be determined if its previous volume at given pressure is known. The procedure consists of three main phases, first the air from the device is evacuated by flushing the measuring gas through the system, after which the gas outlet valve and chamber separation valves are closed, and gas is pressurized in the reference chamber (V_R). After constant reference pressure is reached the separation valve is opened and gas is expanded to the other chamber where the sample is located (V_C). The second stable pressure after expansion is recorded and the true material volume present in the sample holder chamber can be calculated.

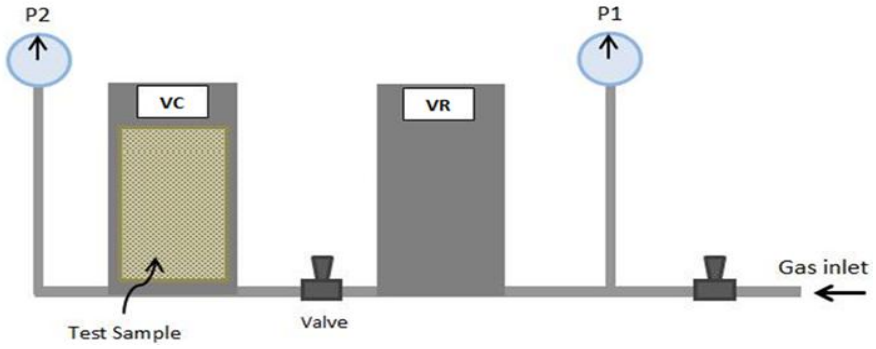

Figure 1

Schematic figure of a two-chamber gas pycnometer

The calculation procedure starts with writing up the equation of states for the three phases. First the equation of state for the gas (for quantity n_a) present in the sample holder chamber at ambient pressure (p_a) after the ventilation phase can be written up as presented in *Equation 2*.

$$p_a(V_C - V_S) = n_a R_u T \tag{2}$$

Next *Equation 3* presents the state of the given quantity of gas (n_1) after closing the two valves and filling the reference chamber to the desired reference pressure (p_1).

$$p_1 V_R = n_1 R_u T \tag{3}$$

Equation 4 will present the last phase where the total amount of gas inside the inner volume at p_2 pressure after expansion.

$$p_2(V_C - V_S + V_R) = n_a R_u T + n_1 R_u T \tag{4}$$

The previous three equations can then be combined into one *(Equation 5)* from which after some rearrangements made *(Equations 6–9) Equation 10* gives the main result of the procedure.

$$p_2(V_C - V_S + V_R) = p_a(V_C - V_S) + p_1 V_R \tag{5}$$

$$p_2(V_C - V_S) + p_2 V_R = p_a(V_C - V_S) + p_1 V_R \tag{6}$$

$$p_2(V_C - V_S) - p_a(V_C - V_S) = p_1 V_R - p_2 V_R \tag{7}$$

$$(p_2 - p_a)(V_C - V_S) = (p_1 - p_2) V_R \tag{8}$$

$$(V_C - V_S) = \frac{(p_1 - p_2)}{(p_2 - p_a)} V_R \tag{9}$$

$$V_S = V_C - V_R \frac{(p_1 - p_2)}{(p_2 - p_a)} \tag{10}$$

Until *Equation 10* all formulas used absolute pressures but with the introduction of gauge pressures (p_{g1}, p_{g2}, psig) the value of the barometric pressure could be taken out of the calculation *(Equations 11–12)*.

$$V_S = V_C - V_R \frac{(p_{g1} + p_a) - (p_{g2} + p_a)}{(p_{g2} + p_a) - p_a} \tag{11}$$

$$V_S = V_C - V_R \frac{p_{g1} - p_{g2}}{p_{g2}} \tag{12}$$

$$V_S = V_C - V_R \left[\left(\frac{p_{g1}}{p_{g2}} \right) - 1 \right] \tag{13}$$

The calculation of the true solid volume inside the apparatus can be made using *Equation 13* in knowledge of the two-gauge pressures before and after the expansion and the volumes of the two chambers with the additional volumes of the connecting pipes and valves.

Now to answer the previous question the measurement of the pore volume of the sample in such equipment is also possible but only if there is no second chamber and gas is expanded from the reference volume to the pore volume itself. In this scenario the pressure drop will be caused by the additional volume of the effective pore space of the sample plug.

The concept of such measurement devices is not new and is already described in the API 40 standard. Unfortunately, this method had not become a staple procedure regarding some problematic nature of it discussed in detail in the following chapter.

However, in combination of the traditional two chamber and the single chamber gas pycnometer both the true solid and pore volume of the sample can be measured. In result porosity could be calculated eliminating the uncertainties coming from the determination of the total geometric volume. However, this is easier said than done due to the difficulties of this kind of procedure.

2.3. The difficulties of the single chamber gas pycnometer setup

As mentioned previously, the pore volume could directly be measured by gas pynometer if a so-called single chamber equipment is used. In this solution the sample must be put in a sample holder where no volume is present around the sample. With this solution, after the separation valve is opened, the gas can only expand to the additional volume inside the core holder which at sufficient seal is equal the pore volume of the sample. To ensure the correct seal the following two criteria must be met. First the inner holder's length must be adjustable to correctly set to the length of the sample. The second is the volume around the sample must be eliminated. Such core holders exist in the petroleum industry for other petrophysical measurements called Hassler type core holders.

These core holders are used during permeability measurement where fluids are pumped through the cross section of the samples. For this purpose, a rubber sleeve is used which goes around the sample and is squeezed onto the surface of the sample using a hydraulic pump. Eliminating the free space around the sample completely. If a bypass channel is used the end plugs could be driven in the direction of the sample as pressure is raised to assure a perfect seal as in the case of a triaxial chamber. In addition, the distilled water used for the sleeve pressure could also be used as a thermostat to ensure the constant temperature throughout the measurement, which is critical.

The remaining two ports of the Hassler type core holders which originally serve as the inflow and out-flow during permeability measurements could be used for filling and evacuating the cell of the measurement gas. The previously described core holder *(Figure 2)* could be used with great results in the single chamber gas pycnometer setup.

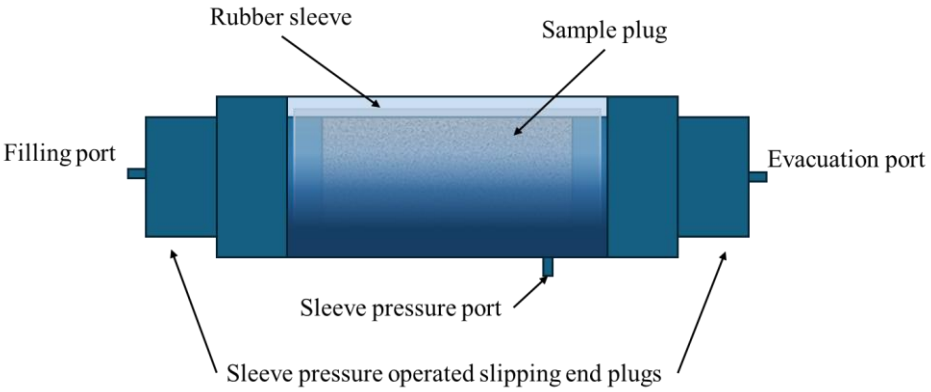

Figure 2
Schematic figure of a Hassler type core holder

With no additional volume in the sample holder during the expansion phase of the measurement the only volume increment causing the pressure drop is the effective pore volume of the sample itself. In result the new formulas for each phase could be derived from *Equations 2–4* as shown by *Equations 14–16*.

$$p_a V_P = n_a R_U T \tag{14}$$

$$p_1 V_R = n_1 R_U T \tag{15}$$

$$p_2 (V_R + V_P) = n_a R_U T + n_1 R_U T \tag{16}$$

After a similar procedure discussed previously the final equation can be written up where the pore volume can easily be calculated in knowledge of the two-gauge pressures in knowledge of the reference volume.

$$V_P = V_R \left[\left(\frac{p_{g1}}{p_{g2}} \right) - 1 \right] \tag{17}$$

Besides the problem of the sealing of the sample there is another major problem that must be solved the accurate reference volume has to be used regarding the measured pore volume of the sample. In the two-chamber configuration multiple reference chambers and measurement chambers are present in function of the sample size. During the procedure there is a tolerance in the size difference between the reference chamber and the free volume in the measurement chamber which if not met causes incorrect results.

Let's consider the following two scenarios. First, the reference volume is significantly larger than the pore volume. In this case the constant p_1 after expansion could drop such slightly that it could not be detected correctly. In the second scenario the reference volume is smaller than the measured pore volume to such an extent that

after the expansion the pressure gauge could show error. These unfortunate cases could be eliminated if the reference volume is correctly sized for which the following procedure could be used.

Table 3

Geometry and volume data of sandstone samples

Sample_ID	diameter, [cm]	length, [cm]	V_T, [cm^3]	$V_{S\_measured}$, [cm^3]	$V_{P\_calculated}$, [cm^3]	ϕ_{He}, [%]
S_01	3.7860	6.1760	69.5278	57.2770	12.2508	17.6200
S_02	3.7960	6.9620	78.7909	61.3480	17.4430	22.1383
S_03	3.7900	6.1820	69.7425	54.6781	15.0644	21.6000
S_04	3.7750	6.9680	77.9887	53.3071	24.6816	31.6477
S_05	3.7860	6.9560	78.3088	52.5987	25.7101	32.8317
S_06	3.7900	6.1250	69.0994	53.5590	15.5405	22.4900
S_07	3.7920	6.1740	69.7257	51.8620	17.8637	25.6200
S_08	3.7900	6.1450	69.3250	50.1081	19.2169	27.7200
S_09	3.7900	6.1790	69.7086	58.2485	11.4601	16.4400
S_10	3.7690	7.0150	78.2654	66.3506	11.9148	15.2236
S_11	3.7740	6.9640	77.9027	58.3604	19.5423	25.0855
S_12	3.7560	7.0110	77.6821	57.3515	20.3306	26.1715
S_13	3.7710	6.9620	77.7565	59.2761	18.4804	23.7671
S_14	3.7900	6.1680	69.5845	55.2779	14.3066	20.5600
S_15	3.7720	6.9840	78.0436	59.9882	18.0555	23.1351
S_16	3.7850	6.9810	78.5488	57.7826	20.7662	26.4373
S_17	3.7830	7.0970	79.7696	54.3739	25.3957	31.8363
S_18	3.7900	6.1370	69.2348	53.4354	15.7994	22.8200
S_19	3.7890	6.9860	78.7712	57.2837	21.4875	27.2784
S_20	3.7750	6.9700	78.0111	52.6042	25.4069	32.5683
S_21	3.7750	6.9700	78.0111	53.9864	24.0248	30.7966
S_22	3.7900	6.1830	69.7537	53.2221	16.5316	23.7000
S_23	3.7880	6.9540	78.3690	53.8532	24.5159	31.2826
S_24	3.7900	6.1530	69.4153	51.3881	18.0272	25.9700
S_25	3.7900	6.1660	69.5620	50.8359	18.7261	26.9200
S_26	3.7710	6.9630	77.7677	58.1860	19.5817	25.1797

First the pore volume range of the samples that will be measured in the future must be determined. In *Table 3* the geometric and porosity data of 26 sandstone samples of Hungarian origin are presented. The dimensions of the cylindrical samples are 1.5" in diameter and approximately 6-7 cm in length. Where the true volumes ($V_{S\_measured}$) were measured by two-chamber Helium pycnometer while the geometrical data by

digital calipers. The data shows that the pore volume of such samples ranges between 11–26 cm^3.

After the separation valve is opened the gas present in the reference cell will expand into this additional volume causing the pressure drop from p_{g1} to p_{g2}. To size the reference volume that would give us the correct reading for both pressure in function of the corresponding volume range the measurement conditions of a true working case were taken into consideration.

3. RESULTS

As presented previously, if a modified triaxial Hassler type core holder is used, and sufficient seal of the sample surface is achieved then theoretically only one problem must be solved. Which is none other than the sizing of the reference volume in function of the measured pore volume.

Considering the porosity range (15–30%) of the 26 sandstone samples the calculated pore volume ranges between 11 cm^3 and 26 cm^3. These values in the following calculations will be referred to as the minimum and maximum of pore volume. The correct reference volume will be found where at the minimal pore volume sufficient pressure loss of the reference pressure is recorded while at the same time at the maximum pore volume pressure loss does not reach a critical level. For the sizing method pressure conditions used in Quantachrome pycnometers (such as Ultrapyc 1200e and older devices) will be taken into consideration. In these two chamber pycnometers the reference pressure is usually set between 17–20 psig which using the correct sample holder and reference chambers for the given sample size will result in an expansion pressure of somewhere between 9–12 psig.

For this reason, during the sizing procedure the recommended pressure of 17 psig (reference) and 10 psig (expanded) was used. Meaning that if the expansion pressure is located between these values the volume is considered sufficient, and if it decreases below 10 psig it is not. This ensures that the added volume is large enough to produce recognizable pressure loss to measure correctly but not large enough to provide the risk of a significant pressure drop.

During the procedure first, the optimal reference volume for both the minimum and maximum pore volumes must be calculated according to Equation 13 where the pressure ratio of 17/10 is used. Resulting in the reference volumes of 15.7143 cm^3 for the minimal and 37.1428 cm^3 for the maximal pore volumes. The required reference volume should be located in between these two values. In the second step the expansion pressures are calculated for both the minimal and maximal pore volumes on this volume range in function of the starting 17 psig reference pressure applying the rearranged form of *Equation 13*. These calculations resulted in the two curves presented in *Figure 3*.

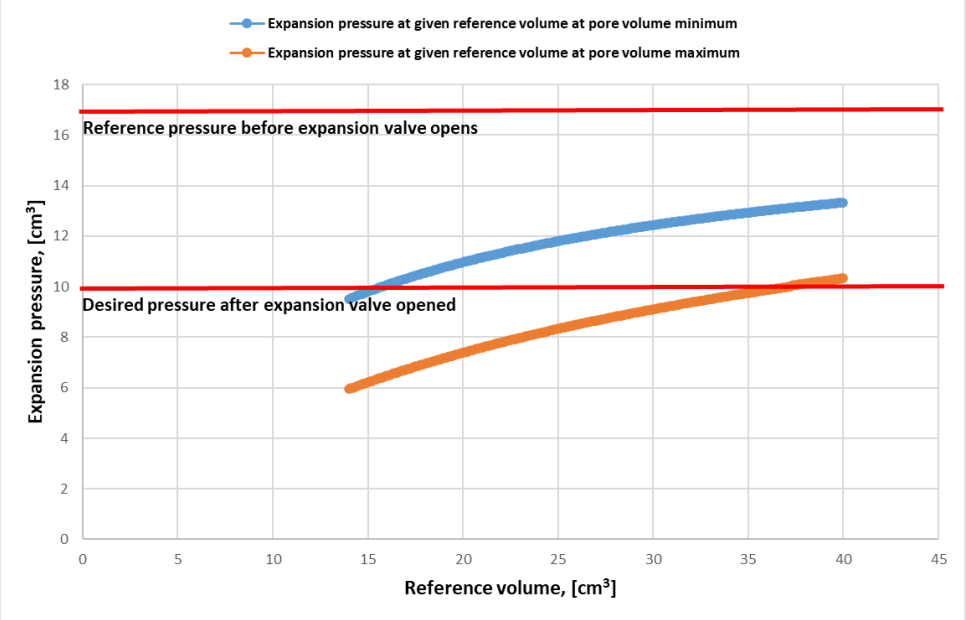

Figure 3

The calculated expansion pressures in function of reference volumes

As shown in the figure the reference volume which is usable for both the minimum and maximum pore volumes is somewhere of 37.2 cm^3. This volume will cause sufficient pressure to drop for the minimum pore volume to calculate the pore volume and is not small enough to cause problems at the maximum pore volume as well. In result a reference volume of 40 cm^3 could be considered as a preferable solution for the measurement of such rock samples.

4. DISCUSSION AND CONCLUSION

In this work the theoretical basis and the need of single chamber gas pycnometry for direct pore volume measurement was introduced. During porosity calculation of sample plugs the highest error occurs from the uncertainties of the total geometric volume of the sample. Therefore, to eliminate its effect, the pore and matrix volumes of the sample must be determined instead.

However, this is easier said than done since traditional two chamber gas pycnometers can only measure the solid volume of the sample. As a result, a second procedure is required to determine the pore volume for which mercury penetration pynometry could be considered as gold standard. Unfortunately, this method is uncapable of measuring the same sample size therefore a much smaller secondary sample must be prepared. Thus, the heterogeneity of the rock can cause significant diversions between the two procedures.

The only solution for direct porosity measurement of the sample plugs is to alter the existing method of gas pycnometry by using a single chamber construction where the pressure after expansion would only be the function of the pore volume.

However, this is easier said than done due to the known difficulties regarding the procedure that hindered its spread in the industry. The problematics of sample loading and the sizing of the reference volume for correct measurement, however, could be solved as presented in this paper.

ACKNOWLEDGMENTS

The research was funded by the Sustainable Development and Technologies National Program of the Hungarian Academy of Sciences (FFT NP FTA).

REFERENCES

Anovitz, L. M., & Cole, D. R. (2015, January). Characterization and analysis of porosity and pore structures. *Reviews in Mineralogy and Geochemistry*, Vol. 80, pp. 61–164. https://doi.org/10.2138/rmg.2015.80.04

API. (1998). *Recommended Practices for Core Analysis RP 40 II.* Washington D.C.: API Publishing Services.

Dotson, B., Slobod, R., McCreery, P., & Spurlock, J. (1951, December). Porosity-Measurement comparisons by five laboratories. *J. Pet. Technol.*, 3 (12), pp. 341–346. https://doi.org/10.2118/951341-G

Jimmy, X. L., Reza, R., Tobias, M. M., & Mohammad, S. (2020). Pore size distribution controls dynamic permeability. *Geophysical Research Letters*, 48 (5). https://doi.org/10.1029/2020GL090558

Lawrence, A. M., & David, C. R. (2015). Characterization and analysis of porosity and pore structures. *Reviews in Mineralogy and Geochemistry*, 80 (1), pp. 61–164. https://doi.org/10.2138/rmg.2015.80.04

Luffel, D., & Howard, W. (1988, december). Reliability of laboratory measurement of porosity in tight gas sands. *SPE Formation Evaluation*, 3 (4), pp. 705–710. https://doi.org/10.2118/16401-PA

Rajib, A., Madland, M. V., Fred, B., & Aksel, H. (2012). A study of sulphite ions-effects on aging and imbibition capillary pressure curve. *International Symphosium of the Society of Core Analysts.* Aberdeen. Retrieved from https://www.researchgate.net/publication/307174636_A_STUDY_OF_SULPHATE_IONS_-EFFECTS_ON_AGEING_AND_IMBIBITION_CAPILLARY_PRESSURE_CURVE#fullTextFileContent

Geosciences and Engineering, Vol. 12, No. 2 (2024), pp. 57–69.
https://doi.org/10.33030/geosciences.2024.02.005

COMBUSTION PROPERTIES OF HYDROGEN-NATURAL GAS MIXTURES FROM 0 TO 100% HYDROGEN CONTENT

KATALIN TOMKÓNÉ NYIRI[1]*, ANNA BELLA GALYAS[2], ISTVÁN SZUNYOG[3]
[1]**Institute of Mining and Energy, University of Miskolc, katalin.tomkone.nyiri@uni-miskolc.hu*
[2]*Institute of Mining and Energy, University of Miskolc, bella.galyas@uni-miskolc.hu*
[3]*Institute of Mining and Energy, University of Miskolc, istvan.szunyog@uni-miskolc.hu*

Abstract: In the past few years, a rising interest has been seen in the use of hydrogen. In the long term, the aim is to replace natural gas, as it is one of the most frequently used energy sources in the EU. In the meantime, blending hydrogen into the existing natural gas pipeline network is also thought to be a promising strategy in environmental aspects. One of the most important environmental benefits of switching from natural gas to hydrogen is the decreasing amount of greenhouse gases coming from combustion. This study focuses on the changes that injecting hydrogen into the natural gas grid causes the combustion characteristics of the mentioned substances. This paper investigates whether the combustion characteristics change drastically if the volume of hydrogen varies between 0–100% or not.

Keywords: *hydrogen-natural gas blend, H_2NG, combustion characteristics, combustion properties*

1. INTRODUCTION

Hydrogen can be an energy carrier, an energy fuel and even an industrial raw material, so it is not surprising that the concept of mixing hydrogen and natural gas is not a new idea. Recent technical developments and the drive towards green energy and carbon neutrality have once again brought the topic into the centre of interest. The transport of a mixture of hydrogen and methane (the primary component of natural gas) by pipeline also has a long history (Hydrogen Europe, 2022), as pipeline networks were built for this purpose in the early 1800s. At that time, however, it was a gas mixture typically produced from coal with a hydrogen content of 30-40%, the so-called “city gas”, that was used to light street lamps, commercial buildings and households. These systems served as the forerunners of today’s modern natural gas networks. To reach the technical level of today’s reliable networks, over the past 200 years many questions and challenges have had to be solved and answered. The next challenge for the working gas infrastructure is injecting hydrogen.

During the process of mixing hydrogen into the natural gas network, an increasing concentration of hydrogen enters the already built natural gas transport and distribution infrastructure, and gets to the end points of the system, which are the gas-using appliances. This can be done for economic or environmental reasons. The basis

of the economic consideration is actually that feeding hydrogen into the already existing gas network can offer a quick and cost-effective temporary solution to the lack of immediately available dedicated hydrogen infrastructure. Furthermore, it is possible to benefit from the advantages provided by hydrogen without the burdens and obligations associated with pipeline construction. This way, mixing hydrogen also provides the possibility for users to have access to certain levels of renewable energy with low carbon dioxide emissions, which benefits corresponding to the environmental protection aspect of the mixing. (Melaina et al., 2013)

With its hydrogen strategy, the REpowerEU plan, the "Fit for 55!" climate law the European Union aims to reduce emissions by at least 55% by 2030 and save energy, diversify supplies and quickly substitute fossil fuels by accelerating Europe's clean energy transition. All these actions make hydrogen essential to support the EU's commitment to reach carbon neutrality by 2050 (European Commission, 2020).

Hungary's national hydrogen strategy, published in June 2021, states that Hungary's natural gas supply infrastructure must be prepared for the blending of at least 2 %(v/v) hydrogen. For this reason, the authors aim to point out the differences between the combustion properties and material characteristics of hydrogen and natural gas. (Hungary's National Hydrogen Strategy, 2021) The introduction of hydrogen into natural gas distribution and transport systems can be considered as the first step on the long road to reduce the burden on our environment, thus creating an opportunity for users to burn the hydrogen-enriched gas mixture. The higher the proportion of the latter component present in the natural gas-hydrogen gas mixture, the lower the number of harmful emissions produced during combustion (Topolski et al., 2022).

2. FLUE GAS COMPOSITION OF NATURAL GAS AND HYDROGEN

The combustion process can be considered perfect if the fuel that reacts with oxygen burns completely during the reaction. The success of the process depends on whether an adequate amount of oxygen is available during combustion or not. If it is given, the reaction results in the formation of a specific amount of combustion products. *Table 1* contains the quantity values of the components of the average natural gas used for our calculations.

Table 2 shows the combustion properties of the individual components of the natural gas-hydrogen mixture (H_2NG). It can be used to compare the products produced during the combustion of hydrogen and methane. The products of perfect and imperfect combustion must be differentiated as well.

The main components of natural gas are hydrocarbons. The perfect combustion of these compounds results in carbon dioxide (CO_2) and water vapor (H_2O) formation. CO_2 has a strong greenhouse effect, so it is an undesired flue gas component, but H_2O can be considered harmless for both the human body and the environment. However, natural gas does not only contain hydrocarbons, and air does not only consist of oxygen, so it is also important to mention what happens when other compounds are also present during combustion, or more specifically the elements that make up the compounds, are burned.

Table 1

National weighted average natural gas component values used for calculations

Source: Order of natural gas quality accounting 2024–2025

Components	Formula	mol%
Methane	CH_4	92.883
Ethane	C_2H_6	3.419
Propane	C_3H_8	1.039
i-Butane	i-C_4H_{10}	0.179
n-Butane	n-C_4H_{10}	0.194
i-Pentane	i-C_5H_{12}	0.043
n-Pentane	n-C_5H_{12}	0.033
n-Hexane	n-C_6H_{14}	0.019
n-Heptane	n-C_7H_{16}	0.014
n-Octane	n-C_8H_{18}	0.007
Carbon-dioxide	CO_2	1.308
Nitrogen	N_2	0.862

Table 2

Combustion equations of individual components of the natural gas-hydrogen mixture

(Vida, 1991)

Main components of the natural gas-hydrogen mixture	
Hydrogen	**Methane**
Stoichiometric combustion equations	
$2\ H_2 + O_2 = 2\ H_2O$	$CH_4 + 2\ O_2 = CO_2 + 2\ H_2O$
Products of complete combustion	**Products of complete combustion**
Water	Carbon-dioxide Water
Products of incomplete combustion	
Hydrogen Nitrogen oxides	Carbon monoxide Sulfur dioxide Nitrogen oxides Residual hydrocarbons

There are some sulfur-containing compounds that can occur as trace components in natural gas. Due to the fact that there is sulfur in the combustion process, an inert gas, sulfur dioxide (SO_2), is produced, which is indirectly responsible for the formation of sulfuric acid (H_2SO_4). The most common sulfur-containing component is hydrogen sulfide (H_2S) (Vida, 1991).

Nitrogen molecules (N_2) can also be present in trace amounts in natural gas and make up more than 2/3 of the air. These molecules are also present during the combustion process, but do not directly participate in it. However, if the flame temperature is high enough, the N_2 molecules combine with the oxygen in the air and produce nitrogen oxides (NO_x) of various compositions. They can be linked to global warming as they are indirect greenhouse gases. In addition, they contribute significantly to the formation of acid rain.

In practice, absolutely perfect combustion is never achieved, so the consequences of incomplete combustion must also be taken into consideration. In the case of incomplete combustion, there is not enough oxygen during combustion for the fuel and

oxygen to fully react, or something, such as a solid surface, takes the heat away from the combustion process. These cases can be summarized as improperly directed firing processes. And the potential source of danger lies in the fact that during these processes, unwanted products are produced, such as carbon monoxide (CO), nitrogen oxides (NO_x) or hydrocarbons (Vida, 1991).

During the combustion of hydrogen, as shown in *Table 1*, neither carbon nor sulfur-based combustion products are produced. The forming water vapor and residual hydrogen are harmless substances, but the nitrogen oxides (NO_x), that are also produced during the combustion of hydrogen, can cause a bigger problem, as these are strong greenhouse gases. As explained in a few paragraphs above, a sufficiently high flame temperature is necessary for NO_x to form. During the burning of hydrogen, the flame speed (which is several times higher than the flame speed that can be measured during the combustion of methane) locally raises the flame temperature to such an extent, that a sufficiently high temperature can be formed for the process to take place. With the help of a special burner, the flame temperature can be reduced, thus preventing the possibility of NO_x formation (Menzies, 2019).

Therefore, to ensure that there are no substances harmful to the environment among the products created during the burning of hydrogen, it is necessary to control the flame temperature, for example with the help of a diffusion burner. This already appears as a requirement if hydrogen is blended with natural gas, since the optimal combustion properties can only be achieved this way.

Additional criteria and critical points for mixing hydrogen into the natural gas transmission and distribution network arise from the different properties of hydrogen and methane (natural gas). Maintaining safety while blending hydrogen into the currently functioning natural gas infrastructure is not simple, because the grid is calibrated for 100% natural gas. Consequently, material grades, fittings, leak-detecting equipment and all other technologies are selected according to the composition of natural gas. It is therefore crucial to investigate how the physical and chemical properties of the gas mixture change when hydrogen is injected.

2.1. Basic differences in gas properties

Hydrogen is a diatomic molecule, so a pair of hydrogen forms unity, while methane, which is considered the main component of natural gas, has 4 hydrogen atoms attached to one carbon atom. Hydrogen is the very first element in the periodic table, and therefore it is the element with the lowest relative atomic mass. Carbon, on the other hand, occupies sixth place in the system, which means that it is characterized by a bigger relative atomic mass. Thus, while pure hydrogen has two atoms with a very low relative atomic mass, methane is a molecule with a much higher relative atomic mass and physical size. These differences foreshadow the challenges of blending hydrogen into the natural gas grid. The following paragraphs describe the combustion characteristics of the natural gas-hydrogen mixture, namely as a function of the hydrogen content. Different formulas are used to calculate the properties of H_2NG blends from 0 to 100% hydrogen content. All the formulas in this study are taken from the book of Meszléry (1978).

3. COMBUSTION PROPERTIES OF NATURAL GAS AND HYDROGEN

The energy found in natural gas, hydrogen and all in their mixtures can be released by combustion. To characterize the combustion process, stoichiometric equations are used, which are based on the consistency of the atomic number and refer to unit mass, volume or mole.

The general stoichiometric combustion equation that can be written down for the combustible components in hydrocarbons is the following

$$C_nH_m + \left(n + \frac{m}{4}\right) * O_2 = n * CO_2 + \frac{m}{2} * H_2O \tag{1}$$

where n is the number of carbon atoms [–], m is the number of hydrogen atoms [–]. *Equation 1* can be used for all the hydrocarbons that can be found in the different types of natural gases. As a result, the combustion equations of the individual components of the natural gas-hydrogen mixture are given, as can be seen in *Table 3*.

Table 3

Combustion equations of individual components of the natural gas-hydrogen mixture (Vida, 1991)

Hydrocarbons and other components (general formula)	**Stoichiometric combustion equations**		**Hydrocarbons and other components (general formula)**	**Stoichiometric combustion equations**	
Methane	CH_4+2O_2	$=CO_2+2H_2O$	Heptane	$C_7H_{16}+11O_2$	$=7CO_2+8H_2O$
Ethane	$C_2H_6+3{,}5O_2$	$=2CO_2+3H_2O$	Octane	$C_8H_{18}+12{,}5O_2$	$=8CO_2+9H_2O$
Propane	$C_3H_8+5O_2$	$=3CO_2+4H_2O$	Carbon-monoxide	$CO+0{,}5O_2$	$=CO_2$
Butane	$C_4H_{10}+6{,}5O_2$	$=4CO_2+5H_2O$	Hydrogen	$H_2+0{,}5O_2$	$=H_2O$
Pentane	$C_5H_{12}+8O_2$	$=5CO_2+6H_2O$	Hydrogen-sulphide	$H_2S+1{,}5O_2$	$=SO_2+H_2O$
Hexane	$C_6H_{14}+9{,}5O_2$	$=6CO_2+7H_2O$			

3.1. Specific theoretical oxygen demand for perfect combustion

The individual stochiometric combustion equations can be combined to calculate the specific theoretical oxygen demand of the perfect combustion process. Being aware of this value is important for the calculation of the stoichiometric air-fuel ratio, that ensures efficient and complete combustion, thus fuel waste is minimized as energy output is maximized if the ratio is known. The specific theoretical oxygen demand of the perfect combustion can be written as follows

$$V_{O_{2theoretical}} = 2 * r_{CH_4} + 3{,}5 * r_{C_2H_6} + 5 * r_{C_3H_8} + 6{,}5 * r_{C_4H_{10}} + \\ + 8 * r_{C_5H_{12}} + 9{,}5 * r_{C_6H_{14}} 11 * r_{C_7H_{16}} 12{,}5 * r_{C_8H_{18}} + 0{,}5 * r_{H_2} + \\ +0{,}5 * r_{CO} + 1{,}5 * r_{H_2S} - r_{O_2} \left[{}^{m^3}/_{m^3} \right] \quad (2)$$

where r_i is the volume ratio of given gas components [–].

When natural gas is burned perfectly, 2.082 m^3/m^3 of oxygen must be available, as is shown in *Table 4*. The introduction of hydrogen into the system reduces this value to a quarter, since only 0.5 m^3/m^3 of oxygen is enough for the perfect combustion of hydrogen. Therefore, the higher the hydrogen feed, the fewer oxygen molecules are sufficient for perfect combustion. Although, it is also necessary to consider that to release the same energy content in the gas appliance that is given when natural gas is burned, several times the volume of hydrogen is required, and thus several times the amount of combustion air.

Table 4

Specific theoretical oxygen demand of the H_2NG mixture for hydrogen at 20 and 100% vol

Specific theoretical oxygen demand of mixture ($V_{O_{2,theoretical}}$) [m^3/m^3]		
NG 100%(v/v)	H_2NG 20%(v/v) H_2	H_2 100%(v/v)
2.082	1.766	0.500

Considering the financial aspects of mixing, it is important to define the concentration limit below which the related gas-using equipment does not even have to be modified or replaced under certain conditions. Several studies have addressed the issue, the consensus of these is that the general limit of mixing hydrogen and natural gas is at 20%(v/v), adding that this is a theoretical maximum. (Lévai and Laza, 2024; Birkitt et al., 2021) It can be said that below 20%(v/v), the change in properties is so small that there is no need to modify the most critical points of the system, the gas-using appliances. For this reason, the values for specific theoretical oxygen demand and other calculations are shown for 0, 20 and 100%(v/v) H_2 content.

3.2. Specific theoretical air requirement for perfect combustion

Based on the fact that approximately 21% is the oxygen content of the air, the formula for the specific theoretical air requirement for perfect combustion is given in *Equation 3*

$$V_{air_{theoretical}} = \frac{100}{21} * V_{O_2\,theoretical} \left[{}^{m^3}/_{m^3} \right] \quad (3)$$

The specific theoretical air requirement defines the exact amount of air needed to completely oxidize the fuel, leading to complete combustion this way. Knowing the

specific theoretical air requirement is essential for designing safe, efficient, and clean combustion systems.

Table 5

Specific theoretical air requirement of the H_2NG mixture for hydrogen at 20 and 100% vol

Specific theoretical air requirement of a mixture ($V_{air_{theoretical}}$) [m³/m³]		
NG 100 v/v%	H_2NG 20 v/v% H2	H_2 100 v/v%
9.916	8.409	2.381

When natural gas is burned perfectly, an air volume of 9.916 m^3/m^3 must be available, as shown in *Table 6*. The introduction of hydrogen into the system reduces this value by almost a quarter, since only 2.381 m^3/m^3 of air is enough for the perfect combustion of hydrogen. Therefore, the higher the hydrogen feed-in, the less air is sufficient for perfect combustion to occur. This confirms what has been discussed in the previous paragraph.

3.3. Specific volume of flue gas components

The amount of flue gas produced during perfect combustion decreases continuously in proportion to the increase in hydrogen content, since the amount of specific oxygen required to burn a unit of hydrogen is significantly less than in the case of natural gas. Therefore, the number of individual components of the flue gas is also continuously decreasing, as can be seen in *Figure 1*.

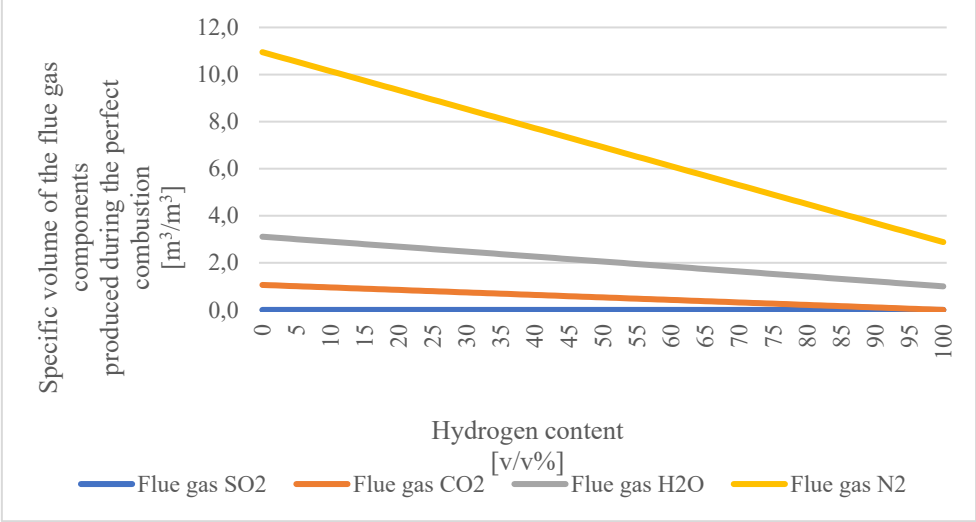

Figure 1

The effect of hydrogen feed on the specific volume of the flue gas components produced during the perfect combustion of the H_2NG mixture

3.4. Flammability concentration limits

To ensure the safe use of the hydrogen-natural gas mixture, it is essential to understand the explosion hazards associated with these mixed gaseous fuels. The flammability concentration limit – also known as the explosion limit – is commonly used as a key indicator in the quantitative risk assessment of explosion risks related to these fuels. There are two types of flammability limits, the Lower Flammability Limit (LFL) and the Upper Flammability Limit (UFL), which define the leanest and richest fuel-air mixtures capable of sustaining combustion. (Jiao et al., 2019) The limits of the range are influenced by many factors, including initial temperature, pressure, quantity and quality of contaminants, ignition source, etc. The addition of inert gas (non-combustible, e.g. N_2, CO_2) significantly affects only the upper concentration limit by decreasing it. Therefore, injecting more inert gas narrows the ignition range. The ignition concentration limits of gas mixtures can be calculated using the Le Chatelier equation, shown in *Equation 4, 5* and *6*

$$Z_{blend} = Z_{c_{blend}} \frac{1 + \frac{B}{1-B}}{1 + Z_{c_{blend}} * \frac{B}{1-B}} \left[{}^{m^3}/_{m^3} \right] \tag{4}$$

$$Z_{c_{blend}} = \frac{1}{\sum_{i=1}^{n} \frac{x_{ci}}{Z_{ci}}} \left[{}^{m^3}/_{m^3} \right] \tag{5}$$

$$x_{ci} = r_i * \frac{1}{1-B} \, [-] \tag{6}$$

where Z_{blend} is the upper or lower ignition concentration limit for each component [m^3/m^3], $Z_{c_{blend}}$ is the lower or upper ignition concentration limit of the mixture calculated on the combustible part [m^3/m^3], x_{ci} is the volume ratio of combustible component to combustible material in the mixture [–], B is the inert content of the mixture [–], Z_{ci} is the upper or lower ignition concentration limit for each combustible component [m^3/m^3].

3.5. Inert content of the gas mixture

The inert content of the natural gas-hydrogen blend shows the summary of the proportions of non-combustible components in the gas mixture, as shown in *Equation 7*

$$B = \sum_{i=1}^{n} x_i \, [-] \tag{7}$$

where x_i is volume fraction of non-combustible components of the gas mixture [–].

Our calculations led to the result, that the value of the inert content decreases to zero because of hydrogen injection, since hydrogen is a combustible component. Therefore, increasing the hydrogen content cannot increase the proportion of non-combustible components (CO_2, N_2 and O_2 content). This conclusion is supported by the calculation results in *Table 6*.

Table 6

Inert content of the H_2NG mixture for hydrogen at 0, 20 and 100%(v/v)

Inert content of mixture (*B*) [-]		
NG 100%(v/v)	H_2NG 20%(v/v) H2	H_2 100%(v/v)
0.010	0.008	0.000

3.6. Volume quotient of combustible components

For further calculations, it is necessary to calculate the volume quotient of combustible components *(Equation 8)*, to establish the flammability concentration limits for the combustible material and then for the whole mixture.

$$x_{ci} = x_i * \frac{1}{1 - B} \; [-] \tag{8}$$

where x_i is the volume fraction of combustible components of the gas mixture [–], B inert content of the mixture [–].

Under the influence of hydrogen feed, practically the volume ratio of all components (other than hydrogen) decreases linearly until it reaches zero as the proportion of hydrogen increases from 0 to 100%(v/v).

3.7. Lower flammability limit of the gas mixture

The first step of calculating the flammability concentration limits is calculating the flammability limits of the combustible content of the hydrogen-natural gas mixture. The lower flammability limit (LFL) refers to the minimum concentration of a combustible component in a gas mixture that can support flame propagation in the presence of an ignition source. Below this concentration, the mixture is too lean to ignite or sustain combustion. (Jiao et al., 2019) The lower flammability limit for the concentration of the combustible content of the gas mixture can be calculated by *Equation 9*

$$Z_{c_{blend_{lower}}} = \frac{1}{\sum_{i=1}^{n} \frac{x_{ci}}{Z_{c_{lower\ i}}}} \left[{}^{m^3}/_{m^3} \right] \tag{9}$$

where x_{ci} is the volume ratio of combustible component to combustible material in the mixture [–], $Z_{c_{lower\ i}}$ is the lower flammability concentration limit for each combustible component [m^3/m^3].

Table 7

Lower flammability limit of the combustible content of H_2NG mixture for hydrogen at 0, 20 and 100%(v/v)

Lower limit of flammability concentration of combustible content of mixture ($Z_{c_{blend_{lower}}}$) [v/v%]		
NG 100%(v/v)	H_2NG 20%(v/v) H_2	H_2 100%(v/v)
4.20	4.16	4.00

When hydrogen is supplied, the lower flammability concentration limit of the combustible components of the gas mixture decreases slightly, dropping by 0.2 v/v%, as can be seen in *Table 7*. This reduction cannot be considered significant. However, knowing the result, the value of the lower flammability limit concentration can be further calculated using *Equation 10*

$$Z_{blend_{lower}} = Z_{c_{blend_{lower}}} \frac{1 + \frac{B}{1-B}}{1 + Z_{c_{blend_{higher}}} * \frac{B}{1-B}} \left[m^3/m^3 \right] \quad (10)$$

where $Z_{c_{blend_{higher}}}$ is the lower ignition concentration limit of the mixture calculated on the combustible part [m^3/m^3], B is the inert content of the mixture [–].

When hydrogen is supplied in the natural gas infrastructure, the lower flammability concentration limit of the gas mixture decreases slightly by 0.24%(v/v), as can be seen in *Figure 2*. This may not be a high value, but knowing it is a key factor from a safety point of view.

3.8. Higher flammability limit of the gas mixture

The higher flammability limit (HFL) – also known as the upper flammability limit (UFL) – is the maximum concentration of a combustible gas in air above which the mixture cannot ignite or explode, even in the presence of an ignition source (Jiao et al., 2019). The first step to calculate the higher flammability limit of the natural gas-hydrogen mixture is calculating the higher flammability limit for the concentration of the combustible content of the gas mixture

$$Z_{c_{blend_{higher}}} = \frac{1}{\sum_{i=1}^{n} \frac{x_{ci}}{Z_{c_{higher\ i}}}} \left[m^3/m^3 \right] \quad (11)$$

where x_{ci} is the volume ratio of combustible component to combustible material in the mixture [–], $Z_{c_{higher\ i}}$ is the higher flammability concentration limit for each combustible component [m^3/m^3].

Table 8

Higher flammability limit of the combustible content of the H_2NG mixture for hydrogen at 0, 20 and 100v/v%

Higher limit of flammability concentration of combustible content of mixture ($Z_{c_{blend_{higher}}}$) [%(v/v)]		
NG 100 %(v/v)	H_2NG 20 %(v/v) H2	H_2 100 %(v/v)
15.43	18.43	80.00

Under the influence of hydrogen feed, the upper flammability concentration limit of the combustible components of the gas mixture shows a clear increase of 64.57%(v/v), as shown in *Table 8*. Knowing the result, the value of the higher flammability limit concentration can be further calculated with *Equation 12*

$$Z_{blend_{higher}} = Z_{c_{blend_{higher}}} \frac{1 + \frac{B}{1-B}}{1 + Z_{c_{blend_{higher}}} * \frac{B}{1-B}} \left[{}^{m^3}/_{m^3} \right] \tag{12}$$

where $Z_{c_{blend_{higher}}}$ is the upper flammability concentration limit of the mixture calculated on the combustible part [m^3/m^3], B is the inert content of the mixture [–].

Under the influence of hydrogen feed, the upper flammability concentration limit of the gas mixture shows a clear, significant increase of 64.40%(v/v). By including the non-combustible components in the equation, the bounds do not change significantly. However, when considering the values of methane and pure hydrogen, there is a very large difference, as can be seen in *Figure 2*. Broader flammability limits mean that a wider variety of gas concentrations becomes flammable, hence even small leaks may result in a flammable or explosive atmosphere.

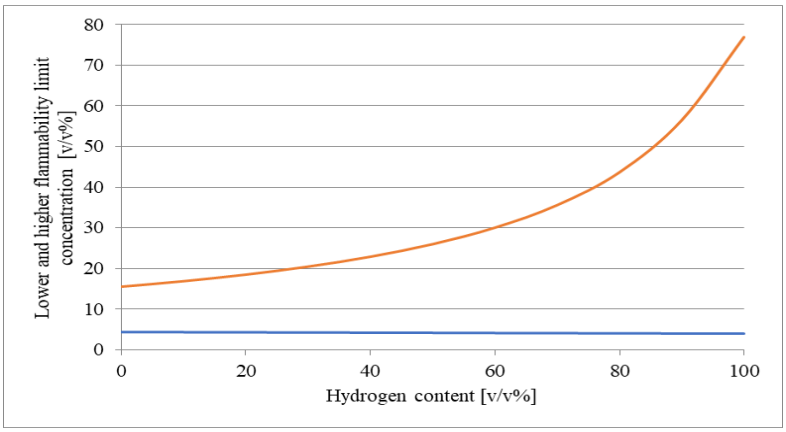

Figure 2

The effect of hydrogen blending on the lower and higher flammability limit concentration of the H_2NG mixture

4. CONCLUSIONS

Hydrogen produced from renewable energy sources can be incorporated into existing natural gas distribution systems or utilized directly at industrial sites. The resulting hydrogen-enriched fuel mixtures facilitate thermal and power generation with reduced greenhouse gas emissions, primarily due to hydrogen's superior combustion characteristics and lower carbon intensity compared to conventional natural gas. Therefore, hydrogen can be the energy carrier of the future, due to its promising combustion properties. As a result of our calculations, we found that the specific theoretical air requirement for perfect combustion is decreasing. The higher the hydrogen feeding, the fewer oxygen molecules are sufficient for perfect combustion. The flammability concentration limits for hydrogen-natural gas mixtures are wider than for natural gas only. The reason for this is that hydrogen has much wider ignition concentration limits than methane. Our calculations have led to the conclusion that the combustion characteristics of hydrogen–natural gas blends are significantly more complex than those of pure methane, introducing challenges in accurately modeling flame behavior and establishing reliable safety thresholds for operational use.

The biggest challenge related to this topic is whether natural gas using equipment can tolerate the presence of hydrogen or not, since these are the bottleneck of the network. An important consideration is the maximum hydrogen fraction that can be safely blended into natural gas without compromising the integrity of infrastructure, combustion performance, or safety standards. Furthermore, existing safety infrastructure – such as sensors, control valves, and ventilation systems – originally designed for pure natural gas applications may lack the sensitivity and response speed required to effectively detect and manage hydrogen-enriched mixtures, given hydrogen's higher reactivity and diffusivity.

ACKNOWLEDGMENTS

The research was funded by the Sustainable Development and Technologies National Programme of the Hungarian Academy of Sciences (FFT NP FTA). https://fenntarthatotechnologiak.hu/

REFERENCES

Hydrogen – Enabling a zero emission society. Hydrogen Europe. Available online: https://hydrogen.revolve.media/2022/Hydrogen_Report_2022.pdf, (accessed on 1 September 2024).

Melaina, M. W., Antonia, O., and Penev, M. (2013). *Blending Hydrogen into Natural Gas Pipeline Networks. A Review of Key Issues.* United States: N. p., 2013. https://doi.org/10.2172/1219920

Topolski, K., Reznicek, E. P., Erdener, B. C., San Marchi, C. W., Ronevich, J. A., Fring, L., Simmons, K., Fernandez, O. J. G., Hodge, B.-M., Chung, M. (2022). *Hydrogen Blending into Natural Gas Pipeline Infrastructure: Review of the State*

of Technology. United States, Golden, CO, National Renewable Energy Laboratory. NREL/TP5400-81704. https://www.nrel.gov/docs/fy23osti/81704.pdf.

Meszléry C. (1978) *Gáztechnikai példatár.* Budapest, Műszaki Könyvkiadó.

Vida M. (1991). *Gáztechnikai kézikönyv.* Budapest, Műszaki Könyvkiadó.

Hungary's National Hydrogen Strategy. National Research, Development and Innovation Office. Available online: chrome-extension://efaidnbmnnnibpcajpcglclefindmkaj/https://cdn.kormany.hu/uploads/document/a/a2/a2b/a2b2b7ed5179b17694659b8f050ba9648e75a0bf.pdf, (accessed on 1 September 2024).

Order of natural gas quality accounting 2024–2025. FGSZ Zrt. Available online: https://fgsz.hu/en/for-business/network-operators/regulatory-framework-network operators/order-of-natural-gas-quality-accounting-users, (accessed on 1 October 2024).

A hydrogen strategy for a climate-neutral Europe. Brussels, European Comission. Available online: https://eur-lex.europa.eu/legal-content/EN/TXT/?uri=CELEX:52020DC0301, (accessed on 1 September 2024).

Lévai, E., Laza, T. (2024). Investigation of Flow and Combustion Technology Changes in a Device Nozzle for Natural Gas as a Result of Mixing in Hydrogen. *Periodica Polytechnica Chemical Engineering*, 68 (2), pp. 172–180. https://doi.org/10.3311/PPch.22785

Birkitt, K., Loo-Morrey, M., Sanchez, C., O'Sullivan, L. (2021). Materials aspects associated with the addition of up to 20 mol% hydrogen into an existing natural gas distribution network. *International Journal of Hydrogen Energy*, 46 (23), pp. 12290–12299. https://doi.org/10.1016/j.ijhydene.2020.09.061

Fit for 55! Council of the European Union. Available online: https://www.consilium.europa.eu/en/policies/fit-for-55/, (accessed on 1 September 2024).

REPowerEU. European Comission. Available online: https://commission.europa.eu/topics/energy/repowereu_en, (accessed on 1 September 2024).

EU Hydrogen Strategy. European Comission. Available online: https://energy.ec.europa.eu/topics/eus-energy-system/hydrogen/key-actions-eu-hydrogen-strategy_en, (accessed on 1 September 2024).

Jiao, Z., Escobar-Hernandez, H. U., Parker, T., Wang, Q. (2019). Review of recent developments of quantitative structure-property relationship models on fire and explosion-related properties. *Process Safety and Environmental Protection*, Vol. 129, pp. 280–290. https://doi.org/10.1016/j.psep.2019.06.027

Geosciences and Engineering, Vol. 12, No. 2 (2024), pp. 70–81.
https://doi.org/10.33030/geosciences.2024.02.006

PREPARATION OF A CANDLESTICK-SHAPED STALAGMITE'S DIGITAL 3D SHAPE

DÓRA RÁBAI[1], TAMÁS BAZSÓ[2], SÁNDOR SZALAI[3], GÁBOR BROLLY[4*]
[1, 2, 4] *Institute of Geomatics and Civil Engineering, University of Sopron, Hungary*
rabai.dora@uni-sopron.hu
[2]*Institute of Geomatics and Civil Engineering, University of Sopron, Hungary*
bazso.tamas@uni-sopron.hu
[3]*Institute of Earth Physics and Space Science, Hungarian Research Network*
szalai.sandor@epss.hun-ren.hu
[4]*Institute of Geomatics and Civil Engineering, University of Sopron, Hungary*
brolly.gabor@uni-sopron.hu
[2]*https://orcid.org/0009-0007-8115-7665*
[3]*https://orcid.org/0000-0001-9034-7945*
[4*]*https://orcid.org/0000-0002-1694-9996*

Abstract: Tall stalagmites, also known as candlestick stalagmites, are considered vulnerable, since their break has a relatively high probability in the event of an earthquake. Their existence has implications on the maximum magnitude of recent earthquakes, which highlights the importance of recording their dimensions and shape accurately. This study introduces the acquisition and processing of terrestrial laser scanner data over the tallest and most vulnerable stalagmite in the Plavecká priepast (Detrekői-zsomboly) in the Little Carpathians (Slovakia). In addition, the 3D point cloud that was captured from three scan positions in 2024 was compared to a TIN model representing an earlier state of stalagmite dated back to 2015. The comparison of the present 3D point cloud and the former TIN model provides information not only on the temporal change of the stalagmite over the past nine years, but also on the discrepancies between the two surveys taken at the different epochs.

Keywords: *laser scanning, 3D point cloud, stalagmite, karstic cave*

1. INTRODUCTION

Since 2013, several measurements and analyses in Plavecká priepast have been carried out. These include resonance measurements of stalagmites, age determination of stalagmites, mechanical laboratory analysis of broken stalagmite fragments (Gribovszki et al., 2017a, 2017b), stalagmites' shape analyses and laser scanning. The main goal of the existing studies is to estimate the long-term seismic hazard values for the close surroundings of the cave. In this paper, we report on the laser scanning of a slim and vulnerable, 4.3 m high standing stalagmite, and the creation of a 3D point cloud.

This stalagmite is located in a shallow cave close to the surface (Gribovszki et al., 2017a) and is therefore suitable for earthquake hazard assessment, either for the present day or backwards in time (think here of the surface amplification of earthquake waves coming from the deep earth). By examining vulnerable dripstones, information can be obtained on the maximum magnitude of earthquakes *(M_{max})*, e.g. the maximum

horizontal acceleration or velocity that the dripstone can "withstand" without fracturing (Szeidovitz et al., 2005, 2008a, 2008b; Gribovszki et al., 2008, 2013a, 2013b, 2017a, 2017b, 2018, 2020; Paskaleva et al., 2006, 2008; Zembaty et al., 2023).

Usually, the first step in the stalagmite-based numerical studies for seismic hazard used to be the calculation of natural frequencies of the stalagmite and its higher harmonics. These kind of numerical eigenfrequency calculations (FEM: Finite Element Method) have been done not only by Hungarian and Polish researchers (Gribovszki et al., 2018; Zembaty et al., 2023), but in other caves in Europe (Martin et al., 2020; Bottelin et al., 2020) as well. Martin et al. (2020) applied 3D laser scanning to build a detailed 3D numerical model of the Minaret stalagmite in Han-sur-Lasse cave. They used this 3D numerical model to calculate the stalagmite natural frequencies with FEM. Bottelin et al. (2020) investigated very fragile soda straws in Choranche cave (France) by FEM both for eigenfrequency and maximal tensile stress calculation, but they did not use laser scanning for building the numerical model of the soda straws. They have first simulated the resonance amplification of speleothems, particularly for very slender soda straws. Kovács and Takács (1980) dealt with the theoretical considerations of finite element analysis of bending vibrations of straight-axial beams like stalagmites or stalactites.

In 2023, we conducted a complete survey with a laser scanner of one of the cave's chambers (the Chamber of Dripstones) in Plavecká priepast. The complete processing of the collected data is still in progress. So far, one 3D digital model of the same 4.3 m high stalagmite has been produced in 2015. This study shows the comparison of the recently prepared and the previous model as well.

2. AIMS AND METHODS

The aim of this present investigation was to create a 3D point cloud of the highest stalagmite in the cave, using data collected by laser scanning in the Plavecká priepast in the Little Carpathians (Slovakia). The cave survey was made difficult by the fact that the cave can only be approached through a 30 m deep ravine and that access to the cave is subject to a permit.

After the laser scanning of the stalagmite from three positions, the registration of the point clouds was carried out using the software packages Leica Cyclone and CloudCompare. The registered point cloud can be used as input data for future stalagmite growth assessment, modeling of natural frequencies and harmonics (Gribovszki et al., 2018; Zembaty et al., 2023), to determine the elastic parameters of the stalagmite (Zembaty et al., 2023) and to calculate the ground acceleration or velocity required for stalagmite fracture (Paskaleva et al., 2006, 2008; Zembaty et al., 2023).

The measurement was carried out using Leica BLK360 instrument, which performs laser ranging with a precision of ±6 mm at 10 m distance, with approximately 100 kHz scanning frequency. Furthermore, the instrument has three integrated HDR cameras, with which RGB colors can be assigned to point measurements (Leica Geosystems, 2017). Two tripods, five 4.5" retro-reflective targets and two 6.5" retro-reflective targets were used. The light weight, and compact size of the instrument enables its use in the cave where rough terrain conditions, and narrow corridors set limitations for using larger equipment.

Three scan positions were established in the "Chamber of dripstones" *(Figure 1a)* to get multiple views of the highest stalagmite in the cave. The next step was to position retro-reflective targets that are used as tie-points for the orientation and merging of individual point clouds. Minimum three tie points were visible from each scan position, and their distance from the instrument was less than 10 m. *Figure 1b* shows an intensity image of part of the cave. The figure also shows two retro-reflective targets.

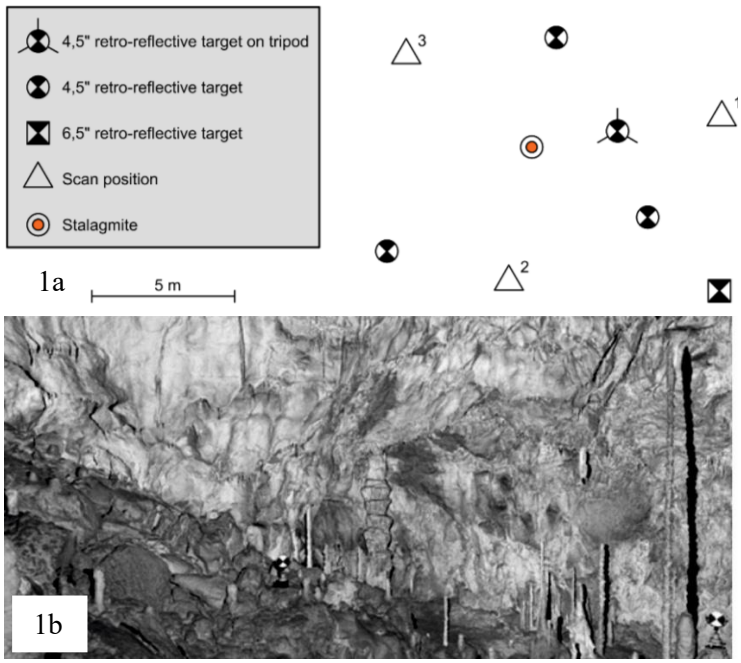

Figure 1

a) Locations of the scan positions and tie-points in the cave area in the "Chamber of dripstones", with the location of the stalagmite under investigation, b) intensity image of a part of the cave with 2 retro-reflective targets

In 2015, a triangulated irregular network (TIN) model of the stalagmite was made by Anton Arpáš, Branislav Balžan and Matej Ruttkay researchers from the Institute of Archaeology of the Slovak Academy of Sciences (SAS). This TIN model from 2015 has been uploaded to the Mendeley database (Zembaty et al., 2022). The 3D point cloud presented in this study has been compared with the TIN model prepared by the researchers from the Institute of Archaeology in 2015. The comparison was made using the CloudCompare software (Girardeau-Montaut, 2011).

3. DESCRIPTION OF THE CAVE AND THE STALAGMITE

The stalagmite is located in Plavecká priepast *(Figure 2)*. The Plavecká priepast is situated in the Little Carpathians, in the western part of Slovakia, close to the Vienna Basin, and close to the Slovak (Bratislava), and Austrian (Vienna) capitals as well.

The karst area on the western edge of the central part of the Little Carpathians is the Plavecký karst. The cave is situated inside the hill on which the Plavecká Castle was built in the thirteenth century. The entrance to the cave is located on the western slope of the castle hill, near the village of Plavecké Pohradie. The castle hill and the adjacent Pohanská Hill contain several caves.

The cave was formed in Triassic limestones which contain layers of dolomite. The Plavecká priepast is a hypogene cave. This origin was first verified by Bella et al. (2019a, 2019b, 2022) during their detailed studies of the surrounding caves – Pec, Plavecká Jaskyna.

The formation of hypogene karst caves is caused by warm or lukewarm waters along regional flow paths. The process is determined by the dissolving effect of these waters and by additional hypogene phenomena specific to the process. Hypogene acids are generated independently of the surface, usually at greater depths in a reductive environment. They usually occur as aqueous solutions of deep CO_2 and H_2S. In addition to carbonic acid dissolution, sulphuric acid cavitation can also occur. In general, deep cavities are unrelated to the surface topography. Nearly equidistant passages, called labyrinthine or networked, usually follow the direction of previous fractures or fissures. The formation of multi-level cave systems is not uncommon (Virág, 2016).

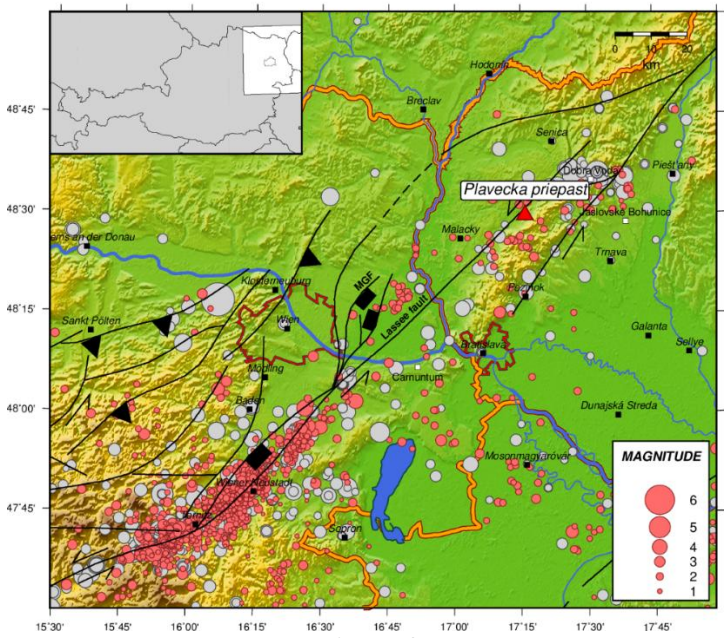

Figure 2

Location of the Plavecká priepast (red triangle) in the Little Carpathians of Slovakia, near the Vienna Basin Transfer Fault System and the other major faults, furthermore grey circles represent the historical and red ones represent instrumental epicentres of earthquakes (Gribovszki et al., 2017a modified by Péter Mónus, GeoRisk Earthquake Engineering Ltd)

The object of our research is a certain 4.3 m high, intact but vulnerable candlestick-shaped stalagmite *(Figure 3)*. Our basic assumption for the earthquake hazard is that these formations survived all earthquakes that have occurred over thousands of years, depending on the age of the stalagmite. Their 'survival' requires that the horizontal ground acceleration has never exceeded a certain critical value within that time period. Such investigations of the mentioned dripstone were reported in detail in Gribovszki et al. (2017a and 2017b) and Zembaty et al. (2023).

The present work aims to compare the models created in 2024 and in 2015, and to assess their usability as input data for future seismic vulnerability-related dripstone studies for various model calculations.

Figure 3
The 4.3 m high stalagmite under study in the Plavecká priepast
(Gribovszki et al. 2017b)

4. DATA PROCESSING

4.1. Registration of individual scans using targets

The point clouds surveyed from different scan positions are referenced in the sensor's own coordinate system, so they need to be transformed into a common one to obtain a spatially consistent, merged point cloud. This process is known as registration, or relative orientation. The point cloud from scan position 2 was chosen as the reference to which the other two point clouds were aligned. The transformation parameters were determined by locating the center of retro-reflective targets in the overlapping parts of the point clouds. Target center coordinates were extracted automatically using Leica Cyclone software package. The RMSE values of the registration were 2 and 3 mm for scans 1 and 3, respectively. The transformation that is defined by a spatial offset vector and three rotation angles about the three coordinate axes, is known as the Helmert transformation. To model the complete shape of the stalagmite, the three point clouds were merged *(Figure4)*. Registration, transformation, and point cloud merging were carried out using the Cloud Compare software package.

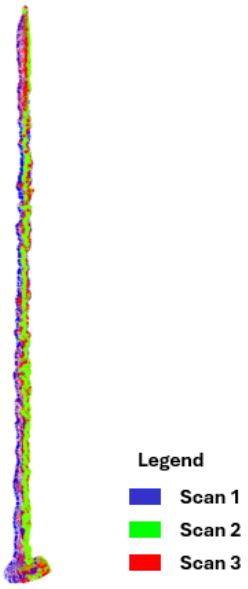

To check the correct fit of the individual point clouds, horizontal cross-sections with a 2 cm thickness were taken along the height of the stalagmite. Figure 5 clearly shows that the alignment of the individual scans is fair, except in the upper-middle part, where unexpected but significant spatial inconsistency is visible.

Figure 4
The merged point cloud of the stalagmite. Colors of the points correspond to the scan positions they originate from.

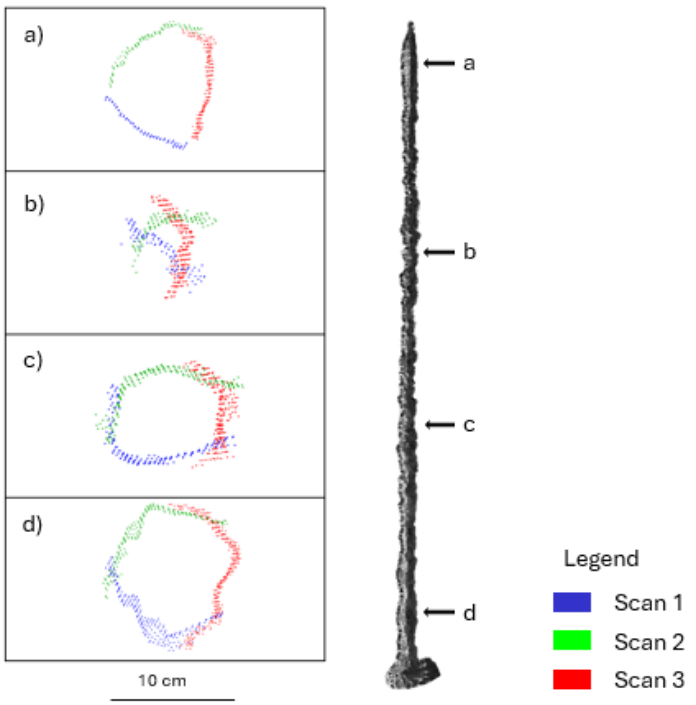

Figure 5
Horizontal sections of the point clouds registered using targets only. Section heights are 0.3 m (a), 1.5 m (b), 2.7 m (c), and 3.9 m (d). Colors correspond to individual scans

4.2. Improvement of the registration

The inconsistency along the middle part of the stalagmite arose from an apparent shift among the individual scans in the radial direction. The magnitude of the shift changes up the stem without showing any systematic pattern. To fix the issue, the individual point clouds were subdivided into 20 cm height slices. Point slices from scan positions 1 and 3 were manually adjusted to that of scan position 2, applying horizontal translation so that the point slices match in the overlapping region. The radial offset vectors resulting from the translation varied both in direction (inward / outward) and in length of up to 3 cm *(Figure 6)*. The merged point cloud with improved alignment is regarded as the structural model of the stalagmite.

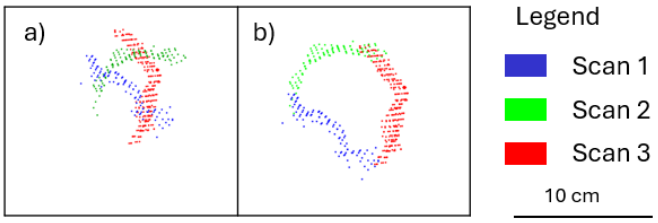

Figure 6

Horizontal sections of the point clouds before (a), and after (b) manual improvement at a height of 2.7 m. Green points of scan 2 were fixed in position, blue and red points of scans 1 and 3 respectively were translated

4.3. Co-registration with the TIN model (2014)

The merged point cloud was compared to the Triangulated Irregular Network (TIN) model created in 2015 (Zembaty et al., 2022). As the point cloud and the TIN model had different local coordinate systems, the former was aligned with the latter using Helmert transformation. The optimal values for the transformation parameters are obtained through the Iterative Closest Point (ICP) procedure, which minimizes the sum of squared distances between the closest point pairs of two data sets.

5. RESULTS

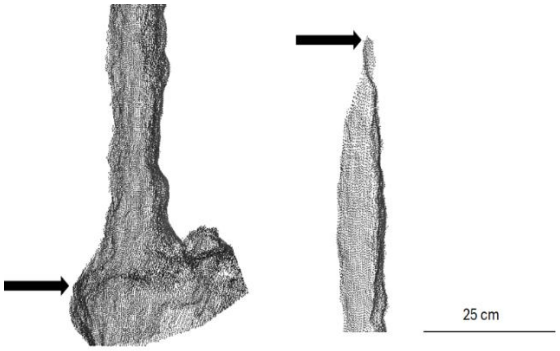

The merged 3D point cloud that represented the surface of the stalagmite consisted of 152.227 points. The total height of the stalagmite measured between the points depicted in *Figure 7* was 4.28 m.

Figure 7

Measurement of the stalagmite's height between the marked points resulted in 4.28 m

The mean directed distance of the closest pair of points in the point cloud and the TIN model was –3 mm. The minus sign indicates that the resultant vector is pointing inward, i.e. from the TIN model towards the point cloud. The standard deviation of the distance between the closest point pairs was 8 mm, with a minimum of –28 mm and a maximum of 62 mm. *Figure 8* depicts the spatial distribution of the residuals. Points with green color lie as close as a few millimeters to the surface of the TIN model. Blue points are inside the TIN model; red points are outside. It is important to note that there is not any extended region along the stalagmite that introduces systematic deviation. Assuming significant growth of stalagmite during the past nine years, most of the points would be expected outside the TIN model. Actually, small errors in data capture (e.g. ranging error of the instrument), registration (e.g. inaccurate location of target centers), and co-registration (e.g. subtle differences in shape) introduce a mixture of errors that together exceed the growth in radial direction, which is far below 1 mm over nine years.

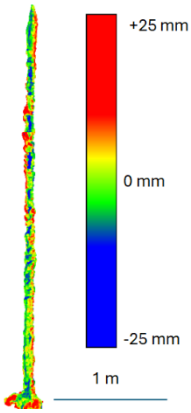

Figure 8
The measure of the directed distances between the two models. For better visuality, the color ramp is clipped to ±25 mm; however, distances range from –28 to 62 mm

Although radial growth is too small to be detected, the largest vertical difference that was observed between the TIN-model and the point cloud may indeed reflect a temporal change, i.e. karst formation, that took place at the base of the stalagmite *(Figure 9)*.

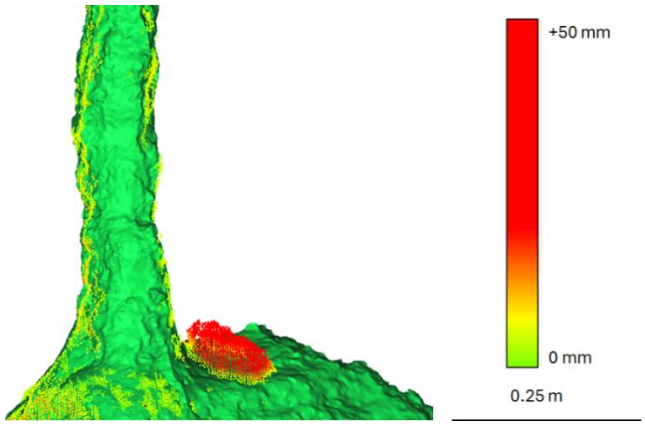

Figure 9
The largest deviation is observed at the base of the stalagmite, which might result from karst formation. The TIN model is displayed in green color; the color ramp applies to the point measurements

Another important difference was revealed at 1.61 m, at a bottleneck, which was regarded as the most vulnerable point of the stalagmite according to statical simulations performed on the TIN model. The shape of the bottleneck seems different in the point cloud; smoother, and the 'nose-shaped' enlargement that is present in the TIN model is absent from the point cloud *(Figure 10)*. The resulting modification in the shape might change the outcome of statical simulations on what magnitude earthquake would cause the breaking of the stalagmite.

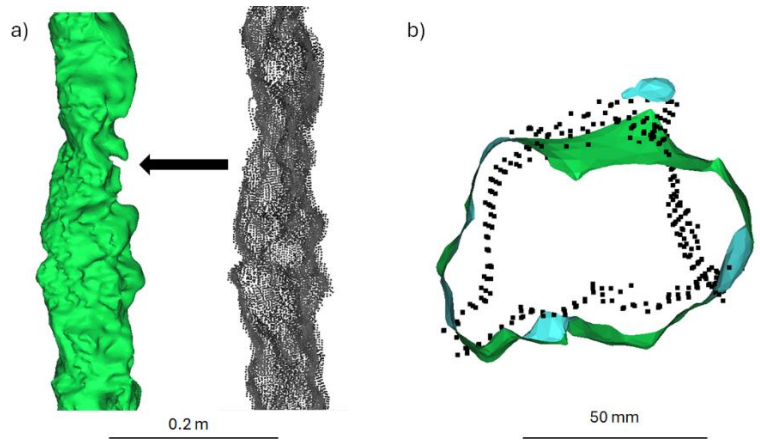

Figure 10

TIN model (2015) and point cloud (2024) at the marker height of 1.61 m, which is regarded as the most vulnerable point of the stalagmite. The point cloud reflects a smoother surface (a), and a lack of the nose-shaped part (b), which might change the outcome of statical simulations on what magnitude earthquake would cause the break of the stalagmite

6. CONCLUSIONS

The main objective of this work was to create a registered point cloud of the highest stalagmite in the cave, Plavecká priepast in the Little Carpathians (Slovakia) using laser scanner data from multiple scan positions. The registration turned out to be challenging as an unusual spatial inconsistency among the transformed point clouds was encountered, which affected mostly the middle part of the stalagmite. Since the misalignment was not systematic, it was fixed by manual translations in height sections. The total height of the stalagmite was measured to 4.28 m. The registered point cloud was compared to a TIN model that had been created from terrestrial laser scanner data nine years before. The co-registration of the two data sets took place using the Iterative Closest Point algorithm, and resulted in a bias of –3 mm, and RMSE of 8 mm. The comparison revealed that the cross-section at the height regarded as the most vulnerable point of the stalagmite has a different shape in the point cloud and in the TIN model. Modification in shape might cause a change in the output of mechanical simulations aiming to estimate the magnitude of earthquakes that cause the break of the stalagmite. In addition, a significant vertical change in the base was

identified, which might indicate natural karst formation over the past nine years. However, neither the data capture nor the registration proved to be accurate enough to detect reasonable temporal change in radial direction.

ACKNOWLEDGMENTS

The authors express their gratitude to the following people: Katalin Gribovszki from Hungarian Research Network (Hun-Ren) initiated this study, organized the field data collection, and supported the authors in the field of seismology. Juraj Littva and Pavel Stanik from the Slovak Museum of Nature Protection and Speleology, and Milan Herz assisted us with the access to the cave. Anton Arpáš, Branislav Balžan and Matej Ruttkay from the Institute of Archaeology of the Slovak Academy of Sciences provided the TIN-model (2015).

This study was supported by GINOP-2.3.3-15-2016-00039, which is highly appreciated.

REFERENCES

Bella, P., Bosák, P., Mikysek, P., Littva, J., Hercman, H., Pawlak, J. (2019a). Multiphased hypogene speleogenesis in a marginal horst structure of the Malé Karpaty Mountains, Slovakia. *International Journal of Speleology*, 48 (2), pp. 203–220. https://doi.org/10.5038/1827-806X.48.2.2265

Bella, P., Bosák, P., Littva, J. (2019b). Hypogénny pôvod jaskyne Pec (Plavecký kras, Malé Kartpaty): tektonická predispozícia a morfologické znaky. *Slovenský kras*, 57 (2), pp. 133–146, https://www.smopaj.sk/sk/documentloader.php?id=2338&filename=kras%2057%20_2%2 0.pdf.

Bella, P., Hercman, H., Kdýr, Š., Mikysek, P., Pruner, P., Littva, J., Minár, J., Gradziński, M., Wróblewski, W., Velšmid, M., Bosák, P. (2022). Sulfuric acid speleogenesis and surface landform evolution along the Vienna Basin Transfer Fault: Plavecký Karst, Slovakia. *International Journal of Speleology*, 51 (2), pp. 105–122, https://doi.org/10.5038/1827-806X.51.2.2420.

Bottelin, P., Baillet, L., Mathy, A., Garnier, L., Cadet, H., Brenguier, O. (2020). Seismic study of soda straws exposed to nearby blasting vibrations. *Journal of Seismology*, 24, pp. 573–593, https://doi.org/10.1007/s10950-020-09922-7.

Girardeau-Montaut, D. (2011). *CloudCompare – 3D point cloud and mesh processing software. Open Source Project.* http://www.cloudcompare.org/.

Gribovszki, K., Paskaleva, I., Kostov, K., Varga, P., Nikolov, G. (2008). Estimating an upper limit on prehistoric peak ground acceleration using the parameters of intact speleothems in caves in southwestern Bulgaria. In: Zaicenco, A., Craifaleanu, I., Paskaleva, I. (eds.). *Harmonization of seismic hazard in Vrancea Zone with special emphasis on seismic risk reduction. NATO Science for Peace and*

Security, series C: environmental security. Dordrecht, Springer, pp. 287–308. https://doi.org/10.1007/978-1-4020-9242-8_17

Gribovszki, K., Kovács, K., Mónus, P., Shen, C. C., Török, Á., Brimich, L. (2013a). Estimation of an upper limit on prehistoric peak ground acceleration using the parameters of intact stalagmites and the mechanical properties of broken stalagmites in Domica cave, Slovakia. *Slovensky kras. Acta Carsologica Slovaca*, 51 (1), pp. 5–14.

Gribovszki, K., Bokelmann, G., Szeidovitz, G., Varga, P., Paskaleva, I., Brimich, L., Kovács, K. (2013b). Comprehensive investigation of intact, vulnerable stalagmites to estimate an upper limit on prehistoric ground acceleration. *Proceedings of the Vienna Congress on Recent Advanced in Earthquake Engineering and Structural Dynamics & 13. DA-CH Tagung*, Vienna, Paper 445, 10 p.

Gribovszki, K., Kovács, K., Mónus, P., Bokelmann, G., Konecny, P., Lednická, M., Moseley, G., Spötl, C., Edwards, R. L., Bednárik, M., Brimich, L., Tóth, L. (2017a). Estimating the upper limit of prehistoric peak ground acceleration using an in situ, intact and vulnerable stalagmite from Plavecka´ priepast cave (Detrekői-zsomboly), Little Carpathians, Slovakia—first results. *Journal of Seismology*, 21 (5), pp. 1111–1130. https://doi.org/10.1007/s10950-017-9655-3

Gribovszki K., Kovács K., Mónus P., Bokelmann, G., Konecny, P., Lednická, M., Moseley, G., Edwards, R. L., Spötl, C., Bednárik, M., Brimich, L., Tóth L., Hegymegi E., Kegyes-Brassai Cs., Szeidovitz Gy. (2017b). Hosszú távú földrengés-veszélyeztetettség becslése a Detrekői-zsomboly (Kis-Kárpátok, Szlovákia) sértetlen állócseppkövének vizsgálatával. *Magyar Geofizika*, 58 (2), pp. 1–16.

Gribovszki, K., Esterhazy, S., Bokelmann, G. (2018). Numerical modeling of stalagmite vibrations. *Pure and Applied Geophysics*, 175, pp. 4501–4514, http://link.springer.com/article/10.1007/s00024-018-1952-4.

Gribovszki, K., Szalai, S., Mónus, P., Kovács, K., Bokelmann, G. (2020). Constraints on long-term seismic hazard from vulnerable stalagmites for the surroundings of Katerloch cave, Austria. *Geosciences and Engineering*, 8 (13), pp. 96–107.

Kovács, M., Takács, F. (1980). Finite element analysis of bending vibrations of a straight-axed beam under consideration of rotary inertia and shear deformation. *Periodica Polytechnica Electrical Engineering*, 24 (1–2), pp. 123–131.

Leica Geosystems (2017). *Leica BLK360 User Manual.* Heerbrugg, Switzerland, Leica Geosystems, 36 p.

Martin, A., Lecocq, T., Hinzen, K. G., Camelbeeck, T., Quinif, Y., Fagel, N. (2020). Characterizing Stalagmites' Eigenfrequencies by Combining In Situ Vibration Measurements and Finite Element Modeling Based on 3D Scans. *Geosciences*, 10 (10), 418. https://doi.org/10.3390/geosciences10100418

Paskaleva, I., Szeidovitz, G., Kostov, K., Koleva, G., Nikolov, G., Gribovszki, K., Czifra, T. (2006). Calculating the peak ground horizontal acceleration generated by paleoearthquakes from failure tensile stress of speleothems. *Proceedings of the International Conference on Civil Engineering Design and Construction*, Varna, Bulgaria, 14. 09. 2006 – 16. 09. 2006, pp. 281–286.

Paskaleva, I., Gribovszki, K., Kostov, K., Varga, P., Nikolov, G. (2008): Assesment of the peak ground acceleration using in-situ tests of intact speleothems in caves situated in NW and SW Bulgaria. *Proceedings of the International Conference on Civil Engineering Design and Construction*, Varna, Bulgaria, 12. 09. 2008 – 14. 09. 2008, pp. 249–263.

Szeidovitz Gy., Leél-Őssy Sz., Surányi G., Czifra T., Gribovszki K. (2005). Paleorengések által gerjesztett maximális horizontális gyorsulásamplitúdók számítása cseppkövek törőszilárdságának ismeretében. *Magyar Geofizika*, 46, pp. 91–101.

Szeidovitz, Gy., Paskaleva, I., Gribovszki, K., Kostov, K., Surányi, G., Varga, Z. (2008a). Estimation of an upper limit on prehistoric peak ground acceleration using the parameters of intact speleothems in caves situated at the western part of Balkan mountain range. *Acta Geodaetica et Geophysica Hungarica*, 43, pp. 249–266. https://doi.org/10.1556/ageod.43.2008.2-3.13

Szeidovitz, Gy., Surányi, G., Gribovszki, K., Bus, Z., Leél-Őssy, Sz., Varga, Z. (2008b). Estimation of an upper limit on prehistoric peak ground acceleration using the parameters of intact speleothems in Hungarian caves. *Journal of Seismology*, 12, pp. 21–33. https://doi.org/10.1007/s10950-007-9068-9

Virág M. (2016). Történeti áttekintés a budai barlangok keletkezéséről – a klasszikus karsztfejlődéstől a hipogén barlangképződésig. *Karszt és Barlang*, 2012–14, pp. 24–46.

Zembaty, Z., Bońkowski, P., Jaworski, M., Gribovszki, K. (2022). Seismic Vulnerability of a Slender Stalagmite – Dataset. *Mendeley Data*, V1. https://doi.org/10.17632/8bzgd3vcsv.1

Zembaty, Z., Bońkowski, P., Jaworski, M., Gribovszki, K. (2023). Seismic Vulnerability of a Slender Stalagmite. *Journal of Earthquake Engineering*, 27 (4), pp. 878–897. https://doi.org/10.1080/13632469.2022.2033356

Tóth, L., Mónus, P., Zsíros, T., Bondár, I., Bus, Z., Kosztyu, Z., Kiszely, M., Wéber, Z., Czifra, T. (1996–2014). *Hungarian Earthquake Bulletin, 1995–2014.* Budapest, MTA GGKI és Georisk Kft.

Zsíros, T. (2000). *The seismicity and earthquake hazard of the Pannonian basin: Hungarian Earthquake Catalog 456–1995.* (in Hungarian) MTA GGKI Szeizmológiai Obszervatórium, 482 p.

Geosciences and Engineering, Vol. 12, No. 2 (2024), pp. 82–92.
https://doi.org/10.33030/geosciences.2024.02.007

ANALYSES OF GRAPHITE-BEARING SCHISTS FROM FERTŐRÁKOS, SOPRON MTS., NW-HUNGARY

LÍVIA LESKÓNÉ MAJOROS[1]*, MÁTÉ ZS. LESKÓ[2], KRISZTIÁN FINTOR[3], DÉLIA BULÁTKÓ-DEBUS[4], FERENC MÓRICZ[5], SÁNDOR SZAKÁLL[6], FERENC KRISTÁLY[7]

[1, 2, 4, 5, 6, 7]*Institute of Exploration Geosciences, University of Miskolc, Hungary*
[3]*Department of Geology, University of Szeged, Hungary*
[1]**livia.leskone@uni-miskolc.hu*
[2]*mate.lesko@uni-miskolc.hu*
[3]*fintor.krisztian@szte.hu*
[4]*delia.bulatko-debus@uni-miskolc.hu*
[5]*ferenc.moricz@uni-miskolc.hu*
[6]*sandor.szakal@uni-miskolc.hu*
[7]*ferenc.kristaly@uni-miskolc.hu*

Abstract: Potential graphite-bearing schists are investigated from Fertőrákos (Sopron Mts., NW-Hungary) with ore microscopy, scanning electron microscopy, Raman spectroscopy, X-ray powder diffraction and X-ray fluorescence spectrometry. Disordered graphite is identified by Raman spectroscopy, which appears as <50 μm sized flakes, and as 50–300 μm sized lens-shaped granular aggregates in the deformed zones of the samples detected by ore and scanning electron microscopy. Using graphite geothermometry on Raman spectra, the average formation temperature of the Fertőrákos samples is ~440 °C (±50 °C).

Keywords: *graphite, Raman spectroscopy, graphite geothermometry, greenschist facies metamorphism, shear zone*

1. INTRODUCTION

Graphite plays an ever-growing role nowadays and is also a critical raw material as included on the List of Critical Raw Materials for the European Union since 2011 (Study on the Critical Raw Materials, 2023). It is worth being aware of potential graphite occurrences in Hungary, and modern analytical techniques (such as Raman spectroscopy) enable detailed examination of graphite and graphitized material.

Recently, graphite occurrences were examined in the NE region of Hungary: Dédestapolcsány from the Uppony Mts. (Majoros, 2019), Meszes (Leskó Majoros et al., 2021) and Szendrőlád (Majoros et al., 2022) from the Szendrő Mts. Generally, the graphite-bearing rocks are siliceous black schists (Dédestapolcsány) or black phyllites (Meszes and Szendrőlád) that have ~1–4 weight% graphite content. Dédestapolcsány samples contain μm sized graphite flakes and 100–300 μm sized grains, Meszes samples have 50–150 μm sized flakes, while Szendrőlád samples contain 20–50 μm sized flakes (Leskóné Majoros et al., 2022).

However, in the NW part of Hungary, graphite exploration was carried out only during the early 1980s. Notably, Kósa and Fazekas (1981) conducted investigations in

the Sopron Mountains. According to their findings, in the Fertőrákos Metamorphic Complex, carbonization-graphitization in the micaschists is a common phenomenon, the degree of carbonization ranges from coal that does not reach the anthracite state to graphite. Based on their observations, the presence of graphite in the assemblage is always related to structurally highly stressed zones and planes; graphite is considered as a tectonite (Kósa and Fazekas, 1981).

Our aim was to collect samples and examine them with several analytical methods (ore microscopy, scanning electron microscopy, Raman spectroscopy, X-ray powder diffraction and X-ray fluorescence spectrometry) to get further detailed information about the graphitized material.

2. MATERIALS AND METHODS

Rock samples were collected from surface outcrops from the southern slope of Újhegy, located 3 km north of the village of Fertőrákos in the Sopron Mountains. The exact coordinates are EOV X_1: 268 936, EOV Y_1: 470 099 (outcrop 1) and EOV X_2: 268 917, EOV Y_2: 470 083 (outcrop 2). The collected graphitic schists belong to the Fertőrákos Metamorphic Complex.

The age of the Complex is early Carboniferous–early Permian, the rocks were affected by greenschist facies metamorphism. Petrologically, it is graphite-bearing phyllite and paragneiss with amphibole schist bodies and frequent pegmatite lenses of high (70–80%) apatite content. Structurally, it is part of the Austroalpine nappe system, overlained by the Sopron Metamorphic Complex with a tectonic boundary (Babinszki et al., 2024). *Figure 1* shows the map of Hungary with Fertőrákos village (Sopron Mts.), the schematic geological map of the investigated area, the surface outcrops and the collected rock samples.

Polished rock slabs were made for ore microscopy (OM), scanning electron microscopy (SEM-EDX) and Raman spectroscopy. The OM examinations were carried out on a Zeiss Axio.Imager A2.m polarizing petrographic and ore microscope with Zeiss AxioCam MRc5 camera. The SEM-EDX measurements were made on a JEOL JXA-8600 Superprobe instrument (in high vacuum at 20 kV, beam current of 20 nA, 60 s dwell time for point analysis). Detection limit of the EDX system for light elements is 0.1 weight%, for heavy elements is 0.05 weight%, the limit of measurement error is 5 relative%. The Raman spectroscopy analyses were carried out on a Thermo Fisher Scientific DXR Raman microscope (532 nm wavelength (green) laser, 2 mW laser power, 3 × 15 s exposure time, ~4 cm^{-1} spectral resolution).

Powder samples were made for X-ray powder diffraction (XRD) and X-ray fluorescence spectrometry (XRF). The XRD measurements were carried out on a Bruker D8 Discover instrument (Cu K-alfa radiation, 40 kV, 40 mA, Bragg-Brentano geometry, LynxEye XE-T PSD detector with 2° opening, 0.007°2θ/24sec counting time). Crystalline phase identification was made in Diffrac*Plus* EVA software by Search/Match algorithm on ICDD PDF2 (2005) database. Rietveld refinement was made with empirical instrument parameterization on NIST SRM640d Si standard in TOPAS4 software, while crystal structure data for calculations were obtained from AMCSD (Downs and Hall-Wallace, 2003) database. The XRF analyses were made

on a Rigaku SuperMini200 WDS instrument (LiF200 / PET / XR25 crystals), with Pd cathode (200 W, 50 kV accelerating voltage, 4 mA beam current) on powder samples pressed into CereOx powder.

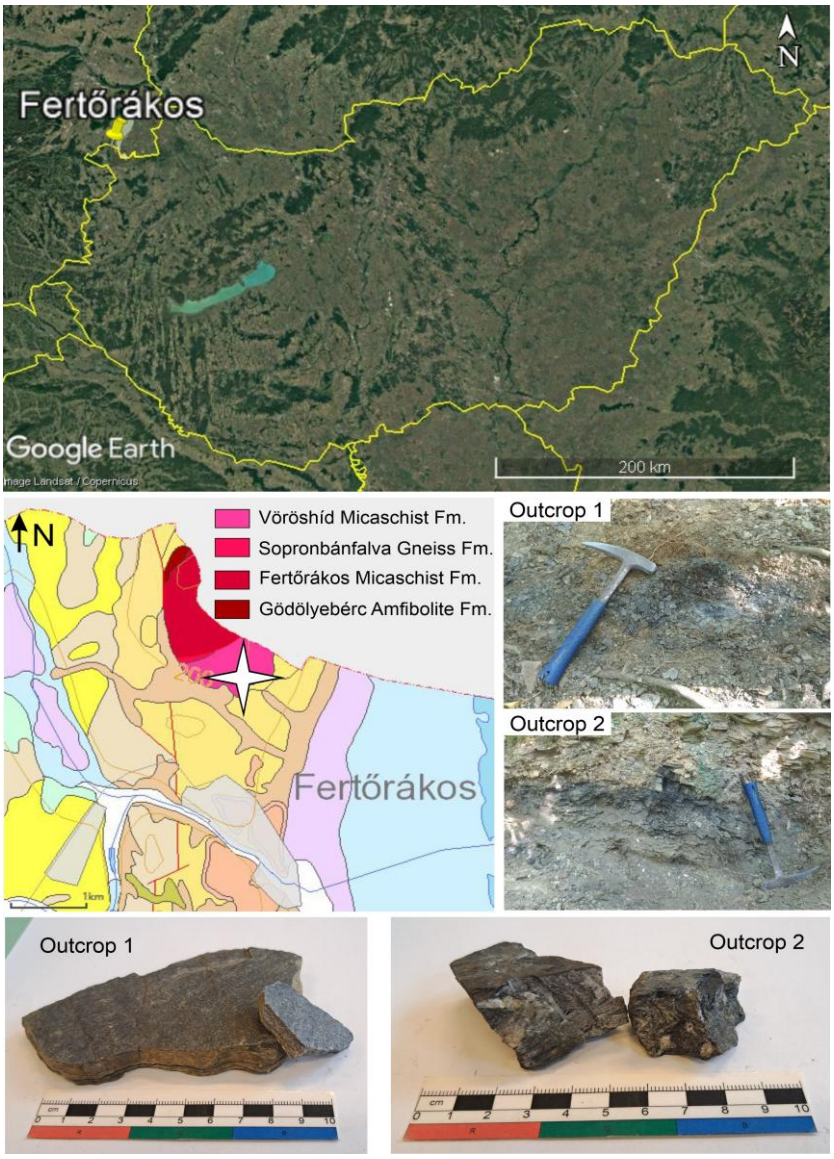

Figure 1

Location map of Fertőrákos village in the Sopron Mts. (top panel). Schematic geological map of the investigated area (online geological map of the Supervisory Authority for Regulatory Affairs, Gyalog and Síkhegyi 2005) (middle left panel). The location of the sample is marked with a white star on the geological map (middle right panel). The surface outcrops and the collected rock samples (bottom panels)

3. RESULTS

3.1. OM and SEM-EDX

Based on OM and SEM-EDX observations, the samples have oriented and highly deformed textures with the marks of shearing deformations, alternating black and white bands. The matrix of the samples consists of 100–300 µm sized quartz grains and 50–100 µm sized phyllosilicate plates (chlorite and muscovite). Muscovite is often paragonitized and fengitized, and a low amount of Ti is also associated according to EDX measurements.

Graphite appears as <50 µm sized flakes, and as 50–300 µm sized granular aggregates, forming lenses *(Figure 2)*. These graphitic aggregates are located in the black bands (particularly in the deformed parts), but some larger aggregates also occur in the white bands. EDX measurements show no sulfur content in the graphitic aggregates.

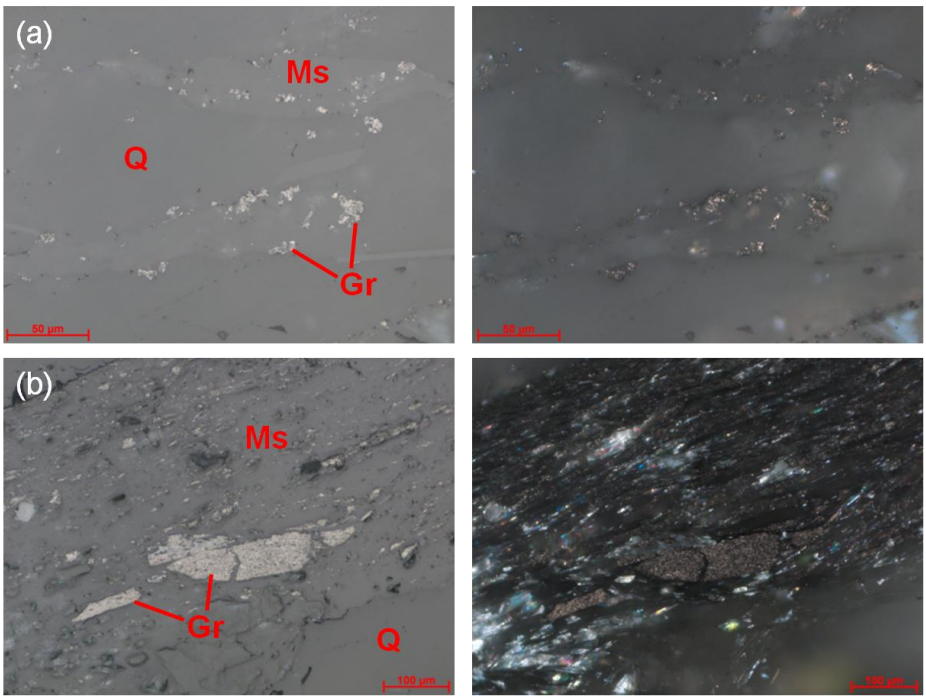

Figure 2

Graphite (Gr) in the quartz (Q) and muscovite (Ms) matrix. Reflected light 1N to the left and XN to the right. (a) Graphite flakes, (b) Graphite flakes and lens-forming graphitic aggregates

The samples contain several accessory minerals. TiO_2 grains with a size of 5–10 µm can be observed scattered in the matrix, and in one place embedded in a fissure-filling smectite. In addition, zircon grains from a few µm to 30 µm in size, monazite-(Ce)

crystals with a size of 10–20 µm, and kaolinite can also be observed in the samples. The monazite-(Ce) grains often have a low Th content based on EDX measurements.

3.2. XRD analysis

The XRD results show quartz rich compositions with trace amounts of muscovite and albite *(Figure 3)*. By XRD, graphite cannot be detected directly on the diffractograms due to its low quantity, nanocrystalline size, preferred orientation and heavy peak overlapping of peak (hkl = 002) between 26°–27°(2θ) with quartz peaks (hkl = 101) and (hkl = 110).

However, by Rietveld refinement, the direct observation and quantification of graphite is possible. *Figure 4* illustrates the calculated quantitative results of the samples.

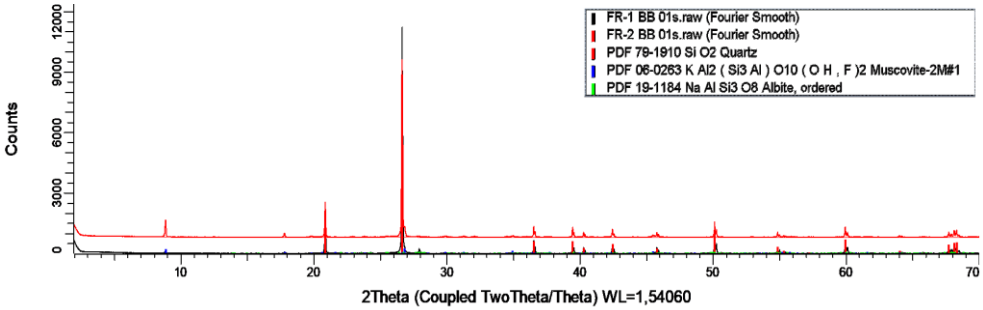

Figure 3
Diffractograms of the Fertőrákos samples

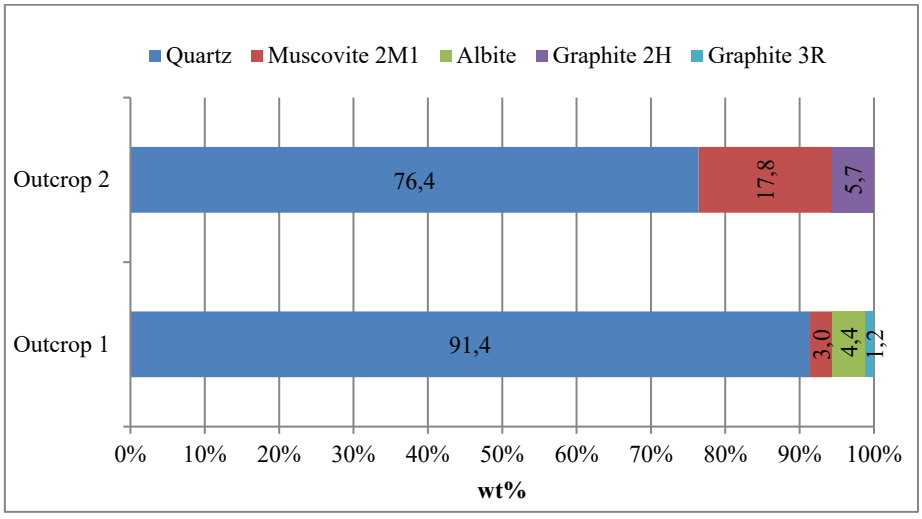

Figure 4
Bar chart of the quantitative results of the Fertőrákos samples by Rietveld refinement (wt%)

3.3. Raman spectroscopy

In the first-order region of the Raman spectrum, two sharp bands can be identified, a higher intensity band at ~1580 cm^{-1} (G band) and a lower intensity band at ~1349 cm^{-1} (D1 band). A low intensity, narrow band at ~1620 cm^{-1} (D2 band) can also be observed as a right shoulder of the G band.

In the second-order region, four bands appear; three bands with low intensity (S1, S3 and S4 bands) and one band with high intensity (S2 band). Furthermore, an initial splitting of the S2 band into two bands (G'_1 and G'_2 bands) can also be observed during the deconvolution. *Figure 5* shows an evaluated Raman spectrum with the first and second-order graphite bands.

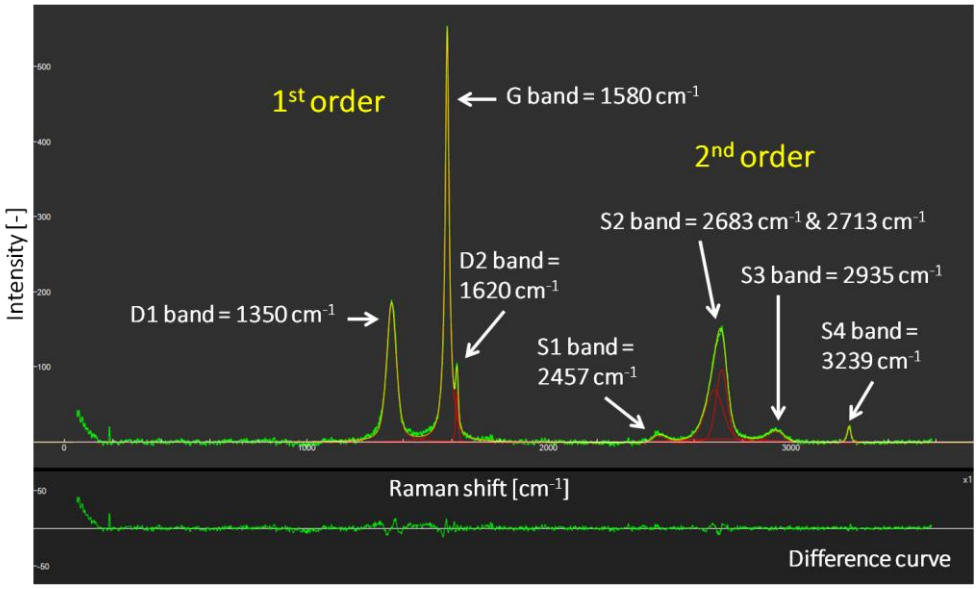

Figure 5

Decomposed Raman spectrum of one measurement point marked with the first and second order bands of graphite

3.4. XRF analysis

By XRF measurements, bulk rock and trace element analysis make it possible to get detailed information about the samples. *Figure 6* shows the major element compositions, while *Figure 7* illustrates the PAAS normalized trace element contents of the samples (PAAS values after Taylor and McLennan 1985). On *Figure 6*, LOI (Loss On Ignition) represents the number of unmeasured elements.

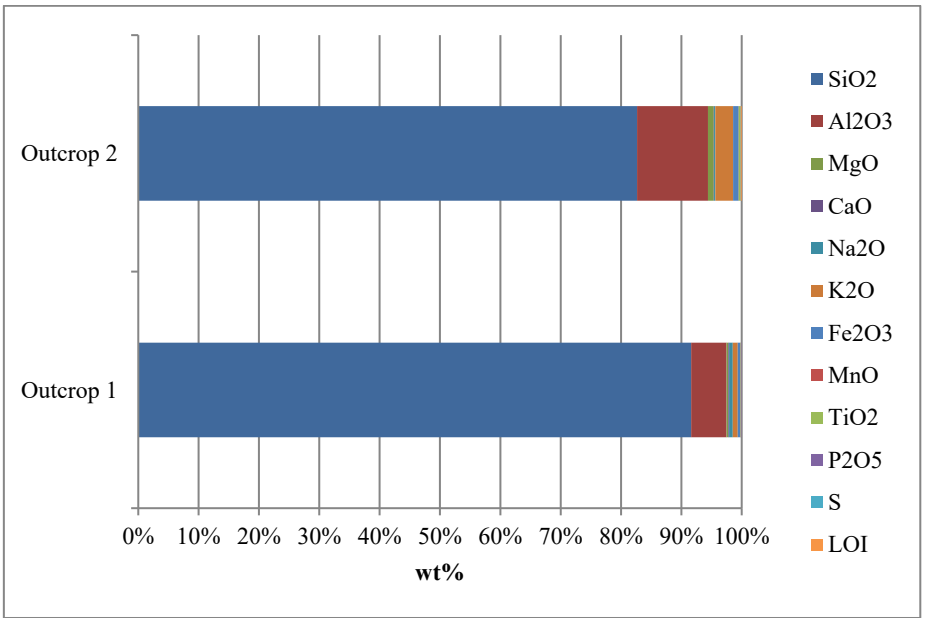

Figure 6
Bar chart of the results of bulk rock analysis by XRF

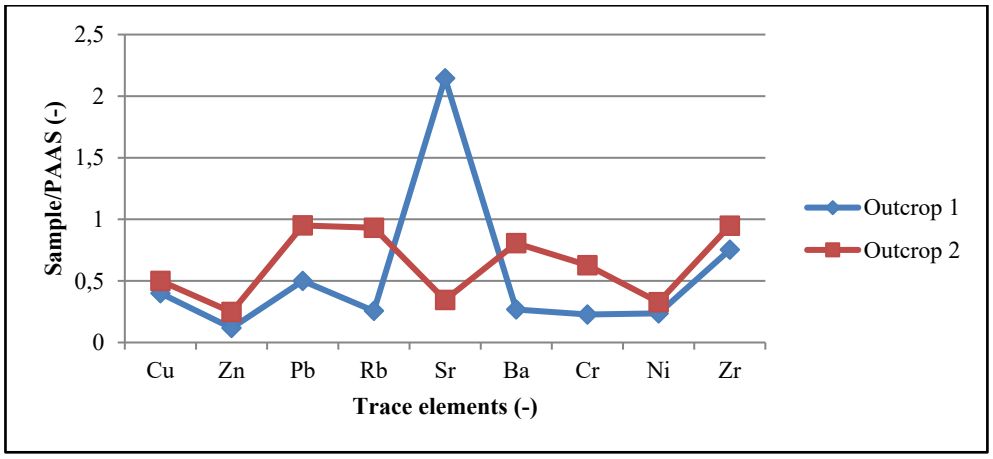

Figure 7
PAAS normalized spider diagram of the results of trace element analysis by XRF
(PAAS values after Taylor and McLennan 1985)

The result of bulk rock analysis by XRF is in accordance with the observations of OM, SEM-EDX and XRD, as it shows quartz rich compositions, the Al, K, Mg, Na and Fe content is related to phyllosilicates (muscovite and chlorite). Ti content is related to TiO_2 and Ti-bearing muscovite, while P content is related to monazite-(Ce). The PAAS normalized trace element analysis by XRF shows a strong positive

Sr anomaly in the sample of outcrop 1, and moderate enrichment of Pb, Rb and Ba in the sample of outcrop 2, and Zr in the samples of both outcrops.

4. DISCUSSION AND CONCLUSIONS

According to our results, graphite cannot be detected directly on diffractograms mainly due to its low quantity and overlapping peaks with quartz peaks. However, its direct quantification is possible by Rietveld refinement; the Fertőrákos samples have 1–5 wt% graphite content. By ore microscopy, graphite flakes and granular aggregates are evidenced in the samples. EDX measurements show no sulfur content in the graphite.

Using Raman spectroscopy, the degree of graphitization of carbonaceous material and the crystallinity of graphite can be identified (Beny-Bassez and Rouzaud, 1985). As both G and D bands appear on the 1st order Raman spectra, and a higher I_G/I_D intensity ratio was detected, the samples contain disordered graphite.

Moreover, Raman spectroscopy is also suitable for determining the peak formation temperature (Henry et al., 2019). One of the parameters required for this is the R2 area ratio value, which can be calculated based on the following equation

$$R2 = D1/(G + D1 + D2), \tag{1}$$

where G is G band area, D1 is D1 band area, D2 is D2 band area.

At first, we used the formula of Beyssac et al. (2002) to calculate the peak formation temperature

$$T(°C) = -445 * R2 + 641\ (\pm 50\ °C) \tag{2}$$

which gives the maximum temperature between 330 and 650 °C. Although *Equation (2)* is developed for graphite formed during regional metamorphism, it uses 514.5 nm laser. However, our measurements were made with 532 nm laser, so we also looked for another equation that also uses 532 nm laser. Thus, we used the formula of Aoya et al. (2010)

$$T(°C) = 221 * (R2)^2 - 637.1 * R2 + 672.3\ (\pm 50\ °C) \tag{3}$$

which is valid between 340 and 655 °C and was developed for contact metamorphic rocks. According to the findings of Aoya et al. (2010), the main effect of using lasers with different wavelengths (514.5 nm and 532 nm) is the systematically greater R2 area ratios obtained with a 532-nm laser. The degree of this effect corresponds to a temperature difference of less than 10 °C. This is in accordance with the findings of Lünsdorf et al. (2014), who investigate all biasing factors to obtain more comparable geothermometric data. Based on their study, three main sources can modify the formation temperature values: spectral curve-fitting procedure, the sample characteristics itself and the Raman system configuration. Taking every biasing factor into account, Lünsdorf et al. (2014) demonstrated that the total difference of all errors is

~10–30 °C, which is below the given error of ±50 °C of Beyssac et al. (2002) and Aoya et al. (2010). Aoya et al. (2010) also concluded that any equation can be used for peak formation temperature calculations (*Equation 2* or *3*) as the error range is ±50 °C. *Table 1* contains the average value of R2 and the formation temperature results calculated using the two formulas.

Table 1

The calculated average R2 area ratio value, the average peak formation temperatures (±50 °C) using the two formulas, and the difference between the calculated temperature values

R2 value [–]	Temperature calculated by the formula of Beyssac et al. (2002) [°C]	Temperature calculated by the formula of Aoya et al. (2010) [°C]	Difference [°C]
0.44	443	434	9

By graphite geothermometry, the average formation temperature of the Fertőrákos samples is ~440 °C (±50 °C), which fits the known geological background of the area, as the Fertőrákos Metamorphic Complex underwent greenschist facies metamorphism (Babinszki et al., 2024).

Due to the metamorphic texture of the samples and the appearance of graphite in the highly deformed zones detected by OM and SEM-EDX, the formation of graphite is connected to shear zones and regional metamorphism.

The high Sr and Ba anomalies, detected by XRF, may indicate fluid-rock interaction. Their enrichment may suggest metasomatic alteration or involvement of a fluid phase during metamorphism (Casillas et al., 2011). The elevated Zr content might suggest the preservation of inherited zircon crystals from the protoliths.

As a conclusion, the joint usage of the applied analytical techniques (ore microscopy, scanning electron microscopy, Raman spectroscopy, X-ray powder diffraction and X-ray fluorescence spectrometry), is a good tool to investigate graphite-bearing samples: texture, mineral paragenesis, crystalline phases, chemical composition, degree of graphitization and peak formation temperature.

REFERENCES

Aoya, M., Kouketsu, Y., Endo, S., Shimizu, H., Mizukami, T., Nakamura, D., Wallis, S. (2010). Extending the applicability of the Raman carbonaceous material geothermometer using data from contact metamorphic rocks. *Journal of Metamorphic Geology*, 28, pp. 895–914. https://doi.org/10.1111/j.1525-1314.2010.00896.x

Babinszki, E., Piros, O., Budai, T., Gyalog, L., Halász, A., Király, E., Koroknai, B., Lukács, R., M. Tóth, T. (eds.) (2024). *Lithostratigraphic units of Hungary I. Pre-Cenozoic formations.* Budapest, Supervisory Authority for Regulatory Affairs.

Beny-Bassez, C., Rouzaud, J. N. (1985). Characterization of carbonaceous materials by correlated electron and optical microscopy and Raman microspectroscopy. *Scanning Electron Microscopy*, 1, pp. 119–132.

Beyssac, O., Goffé, B., Chopin, C., Rouzaud, J. N. (2002). Raman spectra of carbonaceous material in metasediments: a new geothermometer. *Journal of Metamorphic Geology*, 20, pp. 859–871. https://doi.org/10.1046/j.1525-1314.2002.00408.x

Casillas, R., Demény, A., Nagy, G., Ahijado, A., Fernández, C. (2011). Metacarbonatites in the Basal Complex of Fuerteventura (Canary Islands). The role of fluid/rock interactions during contact metamorphism and anatexis. *Lithos*, 125 (1–2), pp. 503–520. https://doi.org/10.1016/j.lithos.2011.03.007

Downs, R. T., Hall-Wallace, M. (2003). The American Mineralogist Crystal Structure Database. *American Mineralogist*, 88, pp. 247–250.

Gyalog, L., Síkhegyi, F. (series editor) (2005). *Geological Map of Hungary, 1:100 000.* Published by the Hungarian National Geological Institute, Budapest. Available online: https://map.hugeo.hu/fdt100/, (accessed on 04 May 2025).

Henry, D. G., Jarvis, I., Gillmore, G., Stephenson, M. (2019). Raman spectroscopy as a tool to determine the thermal maturity of organic matter: Application to sedimentary, metamorphic and structural geology. *Earth-Science Reviews*, 198, 102936, 19 p. https://doi.org/10.1016/j.earscirev.2019.102936

Kósa, L., Fazekas, V. (1981). Geological and petrological structure of the Fertőrákos crystalline schist complex (in Hungarian). *Földtani Közlöny*, 111, pp. 424–452.

Leskóné Majoros, L., Leskó, M. Zs., Szakáll, S., Kristály, F. (2021). Critical minerals and elements in the Szendrő Phyllite Formation (Szendrő Mts., NE-Hungary) (in Hungarian). *Multidisciplinary Sciences*, 11 (1), pp. 90–97. https://doi.org/10.35925/j.multi.2021.1.9

Leskóné Majoros, L., Leskó, M. Zs., Fintor, K., Szakáll, S., Kristály, F. (2022). Graphite occurrences in NE-Hungary. In: Szabó N. P., Virág Z. (eds.). *Új eredmények a műszaki föld- és környezettudományban 2022.* Miskolc-Egyetemváros, Miskolci Egyetem, Műszaki Földtudományi Kar, pp. 49–56.

Lünsdorf, N. K., Dunkl, I., Schmidt, B. C., Rantitsch, G., von Eynatten, H. (2014). Towards a Higher Comparability of Geothermometric Data obtained by Raman Spectroscopy of Carbonaceous Material. Part I: Evaluation of Biasing Factors. *Geostandards and Geoanalytical Research*, 38 (1), pp. 73–94. https://doi.org/10.1111/j.1751-908X.2013.12011.x.

Majoros, L. (2019). *Mineralogical and petrographical examinations of graphitic materials in black schists from Uppony Mts and Szendrő Mts and their Carpathian connections* (in Hungarian). University of Miskolc, Institute of Mineralogy and Geology, MSc diploma thesis, 102 p.

Majoros, L., Fintor, K., Koós, T., Szakáll, S., Kristály, F. (2022). Metamorphic graphite from Szendrőlád (Szendrő Mts., NE-Hungary) detected by simultaneous DTA-TG. *Journal of Thermal Analysis and Calorimetry*, 147, 3417–3425. https://doi.org/10.1007/s10973-021-10713-6

Study on the Critical Raw Materials for the EU 2023. Final Report. European Commission. https://doi.org/10.2873/725585

Taylor, S. R., McLennan, S. M. (1985). *The Continental Crust: Its Composition and Evolution.* Oxford, UK, Blackwell.

Geosciences and Engineering, Vol. 12, No. 2 (2024), pp. 93–108.
https://doi.org/10.33030/geosciences.2024.02.008

MITIGATING METAL LOSS IN WASTE PRINTED CIRCUIT BOARDS REVERSE FLOTATION: THE CRITICAL ROLE OF PARTICLE DISPERSION

ALAA ABBADI[1*], LJUDMILLA BOKÁNYI[2]
[1, 2]*Institute of Raw Material Preparation and Environmental Processing, University of Miskolc, Hungary*
[1*]*abbadi.alaa.imad@uni-miskolc.hu*
[2]*ljudmilla.bokanyi@uni-miskolc.hu*
[1]*https://orcid.gov/0009-0003-9533-7078*
[2]*https://orcid.gov/0000-0003-2038-6556*

Abstract: Froth flotation is emerging as a key technique in Waste Printed Circuit Board (WPCB) recycling, but its efficiency is hindered by the spontaneous aggregation of hydrophobic non-metallic particles, which entrap metals and promote foam formation. This study investigates particle aggregation during pulping and evaluates intense agitation as a pretreatment strategy, focusing on the effect of agitation energy on particle dispersion and its direct impact on flotation. Results showed that aggregation decreased with increasing agitation, reaching optimal dispersion with an Aggregation Index (AI) of 6.6% ±2.5% at 1500 rpm; however, higher energy (2000 rpm) led to foam formation and worsened dispersion (AI = 39.8% ±6.3%), with significant metal entrapment. Flotation outcomes correlated directly with dispersion: increasing stirring speed from 500 to 1500 rpm raised underflow metal recovery from 51.71% to 79.34%. These findings establish a quantitative link between agitation energy, dispersion, and flotation performance, providing a practical pathway through optimized intense agitation pretreatment to facilitate pulping, reduce metal losses, and enhance WPCB reverse flotation efficiency.

Keywords: *WPCBs, Flotation, Dispersion, Aggregation*

1. INTRODUCTION

A major bottleneck in the reverse flotation of waste printed circuit boards (WPCBs) is the poor dispersion of particles within the flotation pulp, primarily due to the aggregation of hydrophobic non-metallic particles (Dai et al., 2021; Das et al., 2021; Han et al., 2018; He and Duan, 2017; Vidyadhar and Das, 2013). This aggregation disrupts selective bubble-particle attachment, which is fundamental to flotation efficiency (Sajjad and Otsuki, 2022; Yang et al., 2023). While the impact of interfacial forces on dispersion and flotation performance is well-established in mineral processing, their role in WPCB systems remains insufficiently investigated. This gap limits the optimization of flotation performance, as unresolved particle aggregation directly contributes to metal loss and poor separation efficiency.

Current research has explored various strategies to improve dispersion in WPCB flotation systems, but most remain limited to lab-scale applications with poor

scalability. Pulping methods involving paste formation followed by dilution have been used to overcome particle floating tendencies upon adding to water, yet offer no viable path for industrial application (Ogunniyi, 2009). Ultrasonic treatment shows potential for enhancing dispersion during pulping or aeration stages (Chen et al., 2023; Wang et al., 2021), but its industrial implementation is constrained by high energy demands and operational complexity (Jeldres et al., 2019). More commonly, intense agitation pretreatment has been employed (Burat et al., 2023; Keleş et al., 2024; Zhu, Ni et al., 2020; Zhu, Zhang et al., 2020), drawing from coal flotation studies where it breaks aggregates, cleans surfaces, and improves flotation performance (Yu et al., 2017). However, in the context of WPCBs, the role of agitation energy input during pretreatment remains largely overlooked, despite its known effects on slurry rheology, reagent interaction, and particle aggregation dynamics (Yang et al., 2023).

This study conducts a systematic investigation into dispersion challenges in WPCB flotation by first characterizing particle aggregation during pulping and identifying the mechanisms that contribute to metal loss at flotation initiation. It then assesses intense agitation as a dispersion strategy, using stirring speed as a proxy for energy input during pretreatment. A quantitative approach is introduced to measure the extent of dispersion achieved. Finally, flotation performance is evaluated across agitation intensities to establish the link between energy input, particle dispersion, and metal recovery.

The novelty of this work lies in isolating and quantifying the effect of agitation energy input on particle dispersion and its direct impact on flotation performance in WPCB systems—an area previously overlooked. By clarifying how aggregation dynamics drive metal loss, this study offers a practical framework for controlling dispersion to improve metal recovery and enhance the overall efficiency of WPCB reverse flotation.

2. MATERIALS AND METHODS

2.1. Sample preparation

A feed sample of 30 kg of depopulated WPCBs was obtained from an e-waste facility for this study, comprising mixed-value boards sourced from PCs, servers, switchboards, and various household appliances. The sample predominantly consisted of multilayer and double-sided boards, with a smaller proportion of single-sided types. The preparation of WPCB flotation feed involved a two-stage comminution process followed by mechanical separation *(Figure 1)*.

In the first comminution stage, an axial gap rotary shear with low circumferential speed rotors performed the initial size reduction, cutting WPCB panels to sizes suitable for the hammer shredder's feeding opening. The rotary shear has 10 mm thick discs with a 20 mm front knife depth. The axial and radial gaps were 0.2 mm and 8 mm, respectively. A modified hammer shredder, converted from a mineral crusher, featured a straight anvil, reinforced sieve, and heavier hammers, operating

with an 18 mm screen. The second stage utilized a high-speed impact mill with a tip speed of 80 m/s and a 2 mm internal screen, further reducing particle size.

Mechanical separation of the comminuted material was carried out in three stages. First, a cross belt magnetic separator (350 mm sender belt width, 20–140 mm adjustable gap, 200 × 310 mm magnet dimensions, 0.5 Tesla flux density, 1.1 kW drive motor, 1 m/s max belt speed) removed ferromagnetic particles. Next, an Eriez HDECS eddy current separator, featuring 7 pairs of rare-earth metal magnets, separated non-ferrous metals. For this study, the eddy current separator operated at 1600 rpm drum revolution and 0.5 m/s belt speed. The final stage utilized an Eriez Magnetics electrostatic drum separator, operated at a drum speed of 30 rpm and an applied voltage of 20 kV. The electrode was positioned 50 mm from the drum, and the separation splitter was set at an angle of approximately 80°.

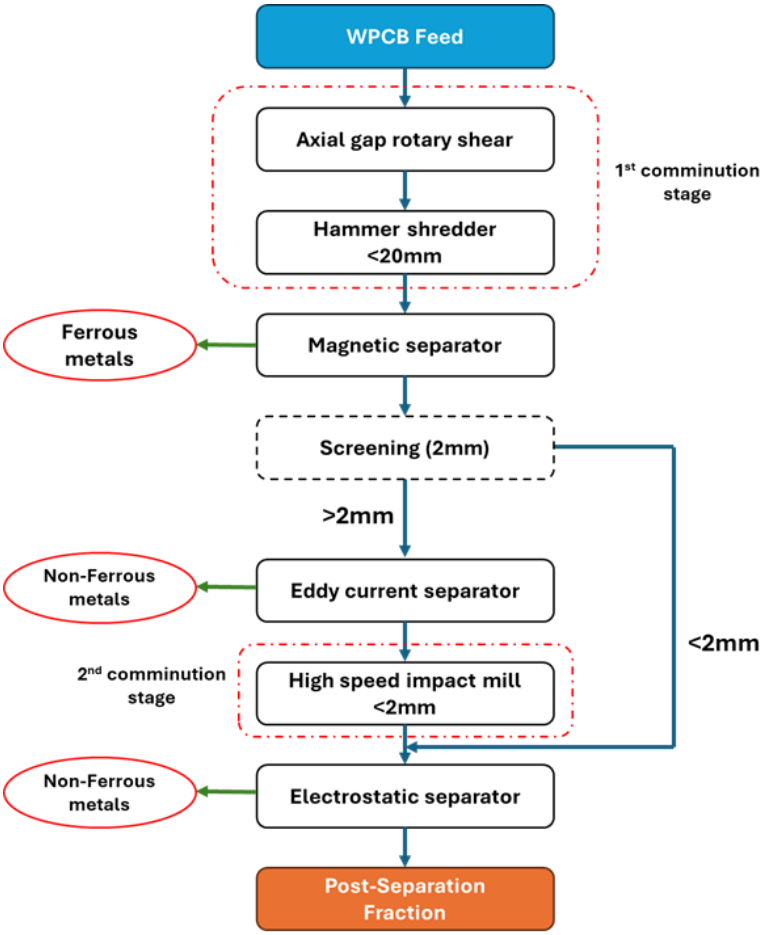

Figure 1

Flowchart of preparation stages for WPCB prior to flotation

2.2. Grinding

Grinding tests were conducted in a laboratory-scale tumbling mill, measuring 19 cm in diameter and 18 cm in length. The experiments used alloy steel balls as the grinding media, with a density of 7.62 g/cm^3. The total mass of the grinding balls was 6.1 kg, achieving a 26.16% fill rate of the mill's volume. A 220 g sample of feed material was used, corresponding to a fractional powder filling of 9.15%. The ball mill operated continuously for 60 minutes. The product was then screened at 0.25 mm, and the fraction below this size was chosen as the feed material for the flotation process.

2.3. Flotation Process

The flotation tests were carried out using a 1L KHD Humboldt Wedag lab mechanical flotation cell. The conditioning strategy tested in this study is illustrated in *Figure 2*. For intense agitation pretreatment, the sample was dispersed in deionized water at 10 wt.% solids and stirred at four different stirring speeds: 500 rpm (1.3 m/s), 1000 rpm (2.6 m/s tip speed), 1500 rpm (3.9 m/s) and 2000 rpm (5.2 m/s). This setup consisted of a four-baffle agitated tank with a four-bladed radial impeller. The 50 mm diameter impeller was positioned 30 mm from the tank bottom. After 15 minutes of stirring, the slurry was transferred to the flotation cell, where the frother was added and conditioned for 2 minutes.

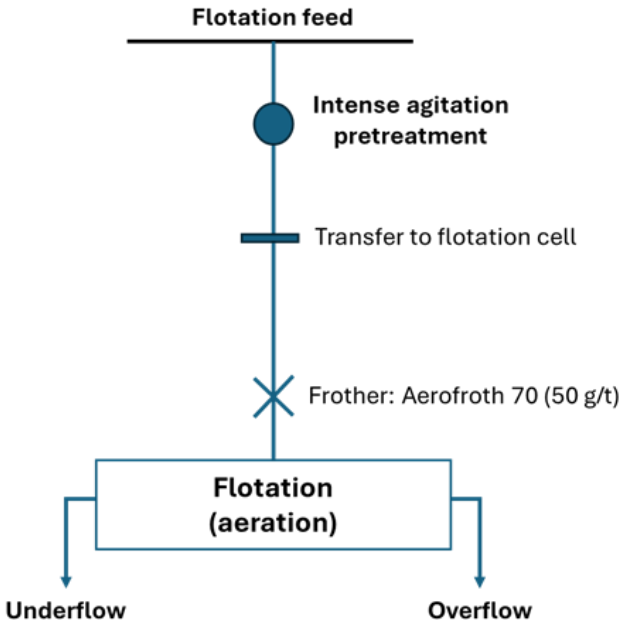

Figure 2
The flowsheets for the flotation experiments

The reagent dosage, impeller speed, and airflow rate were consistent across all flotation experiments, set at 50 g/t frother, 1375 rpm impeller speed, and 2 L/min airflow rate. After each flotation experiment, the overflow and underflow products were collected and dried in an oven for 24 hours at 105 °C. Finally, representative dry samples were prepared for chemical analysis to calculate grades and recovery.

2.4. Characterization

Characterization of WPCP components was conducted using a digital optical microscope (ZEISS Axio Imager). Chemical analyses were carried out at Kisanalitika Ltd., Sajóbábony by ICP-OES method.

To analyze the effect of the conditioning strategy on particle size distribution (PSD), a sample was taken immediately after the agitation step for each conditioning strategy and analyzed by wet sieving. Wet sieving measurements were conducted in triplicate to assess aggregation behavior and the effectiveness of different dispersion methods. To quantify deviations from the dry-basis PSD, the AI was calculated by comparing the PSDs obtained from wet sieving after each conditioning stage to the PSD from dry sieving measurement. The AI, defined by *Equation (1)*, provides a numerical representation of the degree of aggregation

$$\mathrm{AI} = \frac{1}{n}\sum_{i=1}^{n}\left|\frac{\mathrm{wet}_i - \mathrm{dry}_i}{\mathrm{dry}_i}\right| \times 100 \quad (1)$$

where n is the number of size fractions, wet i is the percentage distribution for a given conditioning strategy based on wet sieving, and dry i is the percentage distribution from dry sieving. Lower AI values indicate better performance, signifying a closer match to the dry distribution and, consequently, better dispersion of WPCB particles in water.

3. RESULTS AND DISCUSSION

3.1. Flotation feed characterization

The chemical analysis of the WPCB flotation feed, summarized in Table 1, reveals the concentration of valuable metals.

Table 1

Metal content of WPCB flotation feed

Element	Cu	Fe	Ni	Pb	Zn	Ag	Au
Content (wt.%)	2.3	0.53	0.24	0.10	0.43	0.02	0.006

Figure 3 shows the yield of size fractions and the corresponding metal distribution. The finest fraction (<0.075 mm) had the highest yield (47.6%), consistent with the breakage of brittle polymers and ceramics (Nekouei et al., 2018).

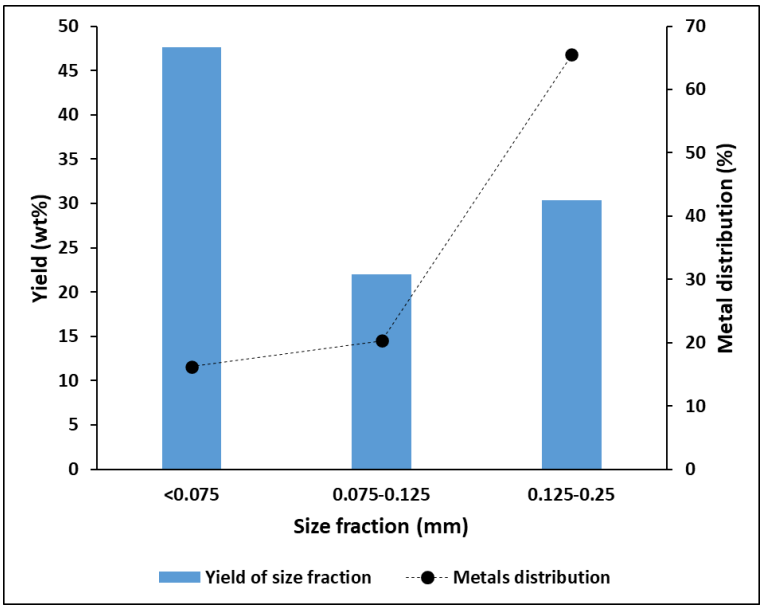

Figure 3
Yield and metals distribution (%) with various size fractions below 0.25 mm used for flotation

In contrast, metal distribution was concentrated in coarser fractions, with 65% of metals found in the 0.125–0.25 mm range, dropping to 16% in the <0.075 mm product. This confirms that metallic components preferentially report to larger size fractions due to their elastic-plastic breakage behavior under mechanical stress, which limits their fragmentation during grinding.

3.2. Aggregation

The initial observation indicates that despite the true density of the WPCB flotation feed being 1.7 g/cm³, the introduction of the WPCB sample into the water for flotation pulp preparation was hindered by the aggregation phenomenon. This resulted in the formation of both completely dry aggregates and partially wetted surface aggregates where the inner particles remained dry. Consequently, their low bulk density caused them to float on the pulp surface *(Figure 4)*.

The immediate formation of dry and partially wetted aggregates upon adding WPCB sample to water can be primarily attributed to the hydrophobic nature of the non-metallic components of WPCBs. Zeta potential measurements as a function of pH *(Figure 5)* revealed that the non-metal particles have a negatively charged surface in a neutral solution, resulting in repulsive forces between them. This rules out electrostatic attraction as a mechanism for non-metal aggregation. Therefore, the predominant forces causing aggregation are the hydrophobic attraction forces (Han et al., 2018). The hydrophobic attraction between particles immersed in water is an effective interaction that arises from the high free energy of cohesion among

surrounding water molecules – particularly the hydrogen-bonding network. When nonpolar surfaces approach each other, structured water at the interface is displaced, reducing the system's free energy and resulting in an apparent attractive force (Van Oss, 2003).

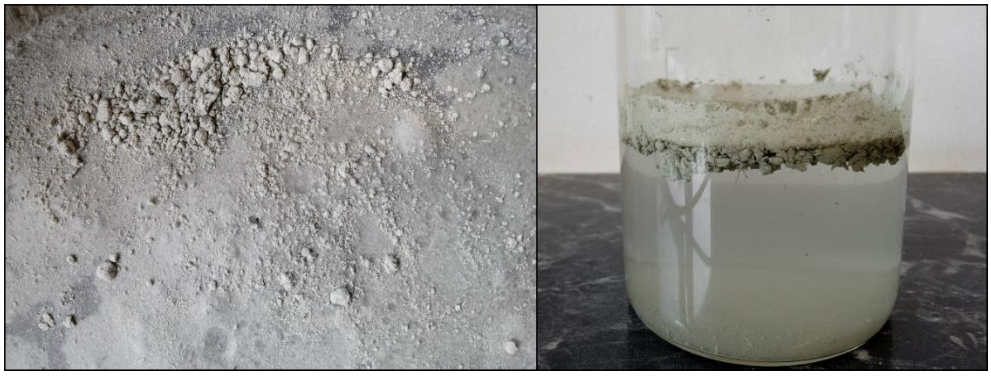

Figure 4
Immediate formation of dry and wet aggregates after adding dry powder of WPCBs to water

The hydrophobicity of WPCB non-metals stems from the organic resins used in WPCB manufacturing (Nie et al., 2023). During production, fiberglass is impregnated with these resins, which are difficult to remove completely by comminution (Kumar et al., 2015). Consequently, the residual resin influences the surface characteristics of both the resin particles and the impregnated fiberglass (Kumar et al., 2020). The WPCB non-polar hydrophobic surfaces tend to minimize their contact area with water, leading to an induced attractive force that causes aggregation.

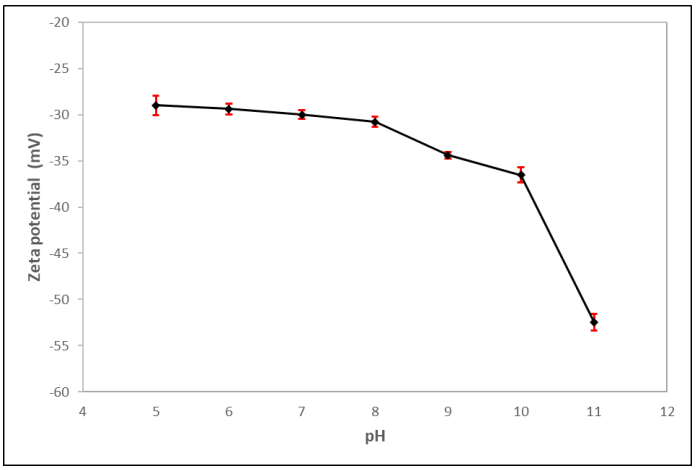

Figure 5
Zeta potential of WPCB non-metal in different pH aqueous solutions

The formation of non-metal aggregates, where they can unselectively entrap metallic particles, poses a significant challenge in the flotation process, as inadequate dispersion may allow these aggregates to persist throughout the conditioning stage and remain within the pulp. This persistence increases the likelihood of their transfer to the froth zone upon flotation initiation.

3.3. Assessment of conditioning

To analyze the aggregation behavior of the WPCB flotation feed and evaluate the effect of intense agitation on dispersion, dry and wet particle size distributions were determined using sieve analysis. While sieve analysis presents limitations due to the energy applied, which may disrupt pre-existing aggregates, it enables the evaluation of the entire batch of samples. Several assumptions underpin this approach: dry sieving approximates a dispersed state due to the absence of water-mediated interactions; particle aggregation manifests as an upward shift in size distribution to coarser fractions (>0.125 mm); and in the absence of aggregation, wet sieving results should closely align with dry sieving. Therefore, deviations from dry sieving baselines are interpreted as aggregation indicators.

Figure 6 presents the size distribution of the suspension under different stirring speeds following the agitation stage. The deviations observed between the dry and wet size distributions highlight the influence of stirring speed as a proxy for energy input in the system.

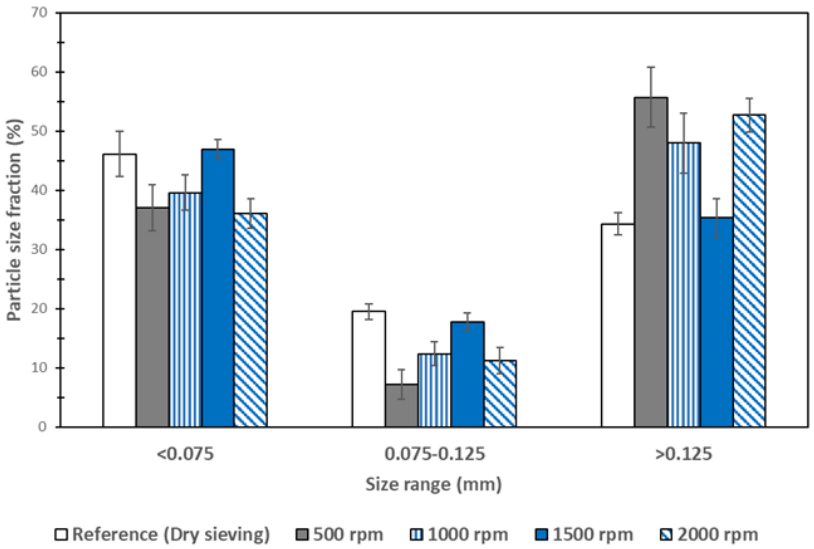

Figure 6
Particle size distribution of WPCB particles after intense agitation at different stirring speeds

Following intense agitation at 500 rpm, a significant shift in particle distribution is observed. The coarse fraction (>0.125 mm) increases markedly to 55.7% ±5.1%, while the intermediate (0.075–0.125 mm) and fine (<0.075 mm) fractions decrease to 7.2% ±2.5% and 37.1% ±3.9%, respectively.

This contrasts with the dry sieving reference, where these fractions were 34.3% ±3.8%, 19.5% ±2.0%, and 46.2% ±1.8%, respectively. The observed increase in coarse fraction and reduction in fine fractions indicate poor dispersion and aggregation within the pulp.

While aggregation persists across all stirring speeds, its extent diminishes with increasing energy input up to an optimal point. This trend is quantified by AI as depicted in *Figure 7*. At 1500 rpm, the lowest AI value of 6.6% ±2.5% is achieved, indicating the most effective dispersion. In contrast, 500 and 1000 rpm exhibit severe aggregation, with AI values of 48.5% ±10.4% and 30.4% ±10.7%, respectively. The substantial difference in AI values underscores the critical role of energy input in destabilizing hydrophobic aggregates, as supported by literature on shear flocculation in mineral processing (Shen and Zhang, 2022).

Higher stirring speeds generate intense shear that disrupts metastable hydrophobic aggregates. The applied mechanical energy overcomes the cohesive interfacial forces that exclude water from particle contact zones. This action forces water infiltration and breaks air pockets within the aggregates, reducing hydrophobic contact and enabling more uniform dispersion throughout the pulp. However, beyond the optimal stirring speed, excessive energy input may not yield further improvements and can even degrade dispersion. This is evident at 2000 rpm, where dispersion deteriorates despite the high energy input.

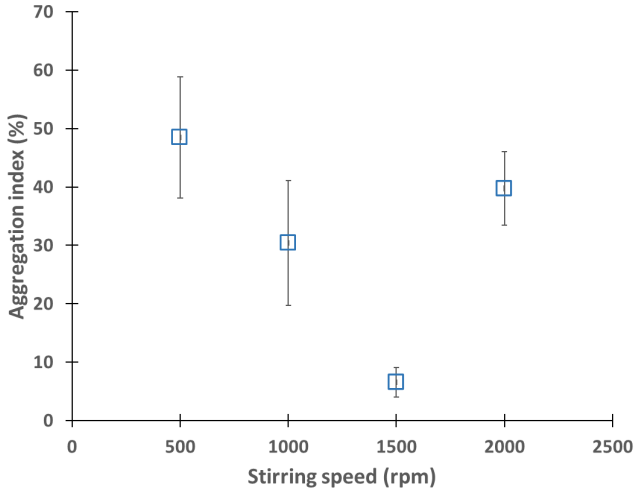

Figure 7

Effect of stirring speed on aggregation index following intense agitation pretreatment

Notably, while 500 and 1000 rpm did not achieve effective dispersion, they also avoided foam layer formation, a phenomenon discussed in detail next. In contrast, the 1500 rpm stirring speed not only achieved the best dispersion but also minimized foam formation, contributing to the slight deviation from the reference PSD. This suggests that 1500 rpm operates within the optimal energy range, providing sufficient energy to disrupt hydrophobic interactions without inducing adverse effects.

At a stirring speed of 2000 rpm, the WPCB suspension exhibited higher aggregation and poorer dispersion compared to 1500 rpm, despite the increased energy input. This is reflected in the AI, which reached 39.8%± 6.3%, indicating a significant reversal in dispersion efficiency. This unexpected trend is primarily attributed to the formation of a stable foam layer at the pulp-air interface *(Figure 8)*, where WPCB non-metallic particles adhere to air bubbles introduced through increased turbulence. A similar phenomenon was reported with flaky graphite particle systems (Yangshuai et al., 2017).

Figure 8

Stable foam layer at the pulp-air interface formed solely by high-speed agitation at 2000 rpm (no aeration or frother addition)

The formation of this layer at the pulp-air interface results from a complex interplay between WPCB particle characteristics and hydrodynamic conditions. Previous research has established that WPCB pulp can generate a stable froth phase upon aeration in surfactant-free conditions, through particle-mediated mechanisms (Ogunniyi and Vermaak, 2009). While conventional two-phase froth systems typically require reduced surface tension, three-phase systems can achieve stabilization through fine particles without necessitating such reductions in surface tension.

The hydrodynamic conditions generated at 2000 rpm play a pivotal role in this phenomenon. Increased turbulence at this high stirring speed introduces a significant quantity of air into the system, while the abundance of fine particles provides a large surface area for stabilizing bubble walls. This dynamic stabilization closely

resembles froth formation, where fine particle flocculation strengthens bubble interstices, maintaining foam integrity even without surfactants.

The foam layer was collected and subjected to PSD, SEM, and chemical analyses. The PSD results confirmed that 86% of the particles in the foam were finer than 0.075 mm, while a combined 14% were coarser. This finding aligns with the proposed mechanism, where fine particles contribute to stabilization while coarser particles may be entrapped as aggregates or individual particles. More critically, microscopic images provided direct evidence of metallic particle presence within the foam layer, as shown in *Figure 9*.

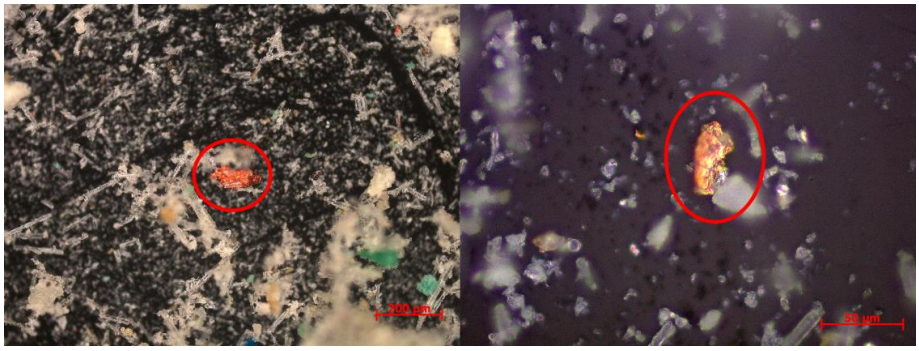

Figure 9

Microscopic evidence of metallic particle entrapment within the foam layer

Chemical analysis further quantified the extent of metal entrapment in the foam, revealing notable metal concentrations: 5.7 g/kg copper, 2.2 g/kg zinc, 0.5 g/kg lead, 1 g/kg nickel, 10 g/kg iron, 212 mg/kg silver, and 22.6 mg/kg gold. These findings indicate that the foam layer can serve as a significant pathway for unintended metal losses during flotation. The persistence of this foam layer at 2000 rpm suggests that beyond an optimal stirring speed, further energy input not only fails to improve dispersion but also exacerbates metal losses by promoting the entrapment of metals within stabilized foam structures.

3.4. Flotation Results

As shown in *Figure 10*, variations in stirring speed significantly influenced both the overflow yield and the underflow metal recovery. Increasing the stirring speed from 500 to 1500 rpm resulted in a decline in overflow yield from 81.62% to 75.91%, while underflow metal recovery improved from 51.71% to 79.34%. These trends can be directly linked to the extent of aggregation formed during the intense agitation pretreatment.

A clear relationship emerges between the degree of aggregation and flotation performance. Higher aggregation levels, such as those observed at 500 rpm, contributed to increased overflow yield, while the lowest aggregation level at 1500 rpm corresponded to the lowest overflow yield. The aggregation increases the apparent particle size with low bulk density, as non-metallic hydrophobic clusters

entrap air pockets, forming larger, low-density structures. These aggregates exhibited enhanced buoyancy, persisting at the pulp-air interface and easily reporting to the overflow upon aeration.

Furthermore, aggregation also impacted underflow metal recovery. The unselective nature of these aggregates, which entrap metallic particles, explains the trend in underflow metal recovery. As dispersion improves with increased stirring speed, metal entrapment within aggregates diminishes, leading to a more selective flotation process and higher metal recovery in the underflow. A similar effect of WPCB particle aggregation on flotation selectivity has been reported, where optimal dispersion conditions yielded the highest metal recovery (Chen et al., 2023). The findings support the relevance of the aggregation index as a comparative tool, with its trend closely reflecting the observed flotation performance.

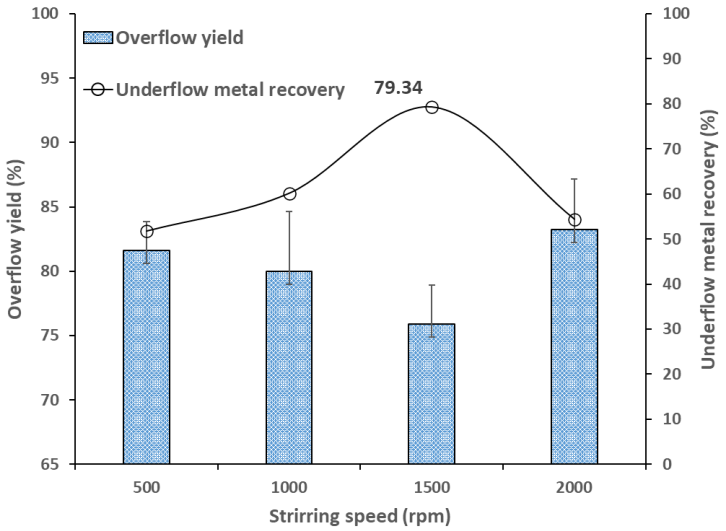

Figure 10
Effect of stirring speed during intense agitation pretreatment on flotation performance

The flotation behavior following intense agitation at 2000 rpm deviates from the previously observed trends. Here, the dominant factor is not aggregation but rather the formation of a stable foam layer at the pulp-air interface, a phenomenon unique to the highest turbulence condition. Upon aeration, this foam layer reports directly to the overflow, significantly increasing the overflow yield to 83.25%. Additionally, the foam layer's ability to entrap metallic particles exacerbates metal losses, as it creates a physical barrier that prevents metals from settling into the underflow. Consequently, flotation after 2000 rpm agitation pretreatment results in low underflow metal recovery at 54.36%.

4. CONCLUSIONS

The inherent hydrophobicity of WPCB non-metallic particles resulting from residual organic resins used in manufacturing, drives complex behaviors in aqueous systems. These non-polar surfaces minimize contact with water, leading to hydrophobic attraction forces that manifest in two key pathways detrimental to flotation performance. First, spontaneous aggregation during pulp preparation forms buoyant clusters that entrap metallic particles and hinder selective separation. Second, fine hydrophobic particles stabilize air bubbles introduced by turbulence, generating a persistent, metal-laden foam layer at the pulp-air interface.

Intense agitation was investigated as a pretreatment strategy to enhance dispersion, with stirring speed being a critical factor. The application of intense agitation effectively and irreversibly broke up aggregates, releasing entrapped metals and significantly improving particle dispersion. This was consistently observed as enhanced metal recovery in reverse flotation, particularly following the optimized stirring speed. However, when the stirring speed exceeded this optimal range, excessive turbulence promoted the foam formation at the pulp-air interface. This foam layer, stabilized by fine hydrophobic particles, acted as a secondary site for metal entrapment and contributed to increased losses to the overflow.

Future work will focus on the distinct flotation behaviors of individual metals, which are obscured when recovery is assessed in bulk. Despite optimized pretreatment, significant and variable losses of specific metals to the overflow were observed under uniform flotation conditions. This highlights the need to shift toward metal-specific analysis, considering how factors such as liberation, morphology, and composition influence recovery. Such an approach is essential for developing targeted strategies that maximize economic value rather than bulk recovery.

ACKNOWLEDGMENTS

The authors would like to express their gratitude to István Balika from Metalex 2001 Kft. for providing the waste printed circuit board samples used in this study. We also thank Kisanalitika Ltd., Sajóbábony for conducting the chemical analysis of the flotation samples.

REFERENCES

Burat, F., Dinç, N. İ., Dursun, H. N., Ulusoy, U. (2023). The Role of Particle Size and Shape on the Recovery of Copper from Different Electrical and Electronic Equipment Waste. *Minerals*, 13 (7). https://doi.org/10.3390/min13070847

Chen, L., He, J., Zhu, L., Yao, Q., Sun, Y., Guo, C., Chen, H., Yang, B. (2023). Efficient recovery of valuable metals from waste printed circuit boards via ultrasound-enhanced flotation. *Process Safety and Environmental Protection*, 169 (September 2022), pp. 869–878. https://doi.org/10.1016/j.psep.2022.11.046

Dai, G., Han, J., Duan, C., Tang, L., Peng, Y., Chen, Y., Jiang, H., Zhu, Z. (2021). Enhanced flotation efficiency of metal from waste printed circuit boards modified by alkaline immersion. *Waste Management*, 120, pp. 795–804. https://doi.org/10.1016/j.wasman.2020.11.002

Das, S. K., Ellamparuthy, G., Kundu, T., Ghosh, M. K., Angadi, S. I. (2021). Critical analysis of metallic and non-metallic fractions in the flotation of waste printed circuit boards. *Powder Technology*, 389, pp. 450–459. https://doi.org/10.1016/j.powtec.2021.05.061

Gouvêa Junior, J. T., Chipakwe, V., de Salles Leal Filho, L., Chehreh Chelgani, S. (2023). Biodegradable ether amines for reverse cationic flotation separation of ultrafine quartz from magnetite. *Scientific Reports*, 13 (1), pp. 1–16. https://doi.org/10.1038/s41598-023-47807-0

Han, J., Duan, C., Li, G., Huang, L., Chai, X., Wang, D. (2018). The influence of waste printed circuit boards characteristics and nonmetal surface energy regulation on flotation. *Waste Management*, 80, pp. 81–88. https://doi.org/10.1016/j.wasman.2018.09.002

He, J., Duan, C. (2017). Recovery of metallic concentrations from waste printed circuit boards via reverse floatation. *Waste Management*, 60, pp. 618–628. https://doi.org/10.1016/j.wasman.2016.11.019

Jeldres, R. I., Uribe, L., Cisternas, L. A., Gutierrez, L., Leiva, W. H., Valenzuela, J. (2019). The effect of clay minerals on the process of flotation of copper ores – A critical review. *Applied Clay Science*, 170 (January), pp. 57–69. https://doi.org/10.1016/j.clay.2019.01.013

Kar, U., Nili, S., Mends, E., Vahidi, E., Chu, P. (2025). A review and environmental impact analysis on the current state of froth flotation on recycling of e-wastes. *Resources, Conservation and Recycling*, 212 (June 2024). https://doi.org/10.1016/j.resconrec.2024.107967

Keleş, B., İlkyaz Dinç, N., Nur Dursun, H., Burat, F., Ulusoy, U. (2024). The effect of particle geometry (size & shape) on the recovery of gold and copper metallic particles from end-of-life random access memory cards by flotation. *Waste Management*, 179 (February), pp. 66–76. https://doi.org/10.1016/j.wasman.2024.03.008

Kumar, A., Holuszko, M. E., Janke, T. 2020. Examining the surface properties of waste printed circuit boards rejects using inverse gas chromatography. *Resources, Conservation and Recycling*, 163 (August), 105093. https://doi.org/10.1016/j.resconrec.2020.105093

Kumar, V., chun Lee, J., Jeong, J., Jha, M. K., su Kim, B., Singh, R. (2015). Recycling of printed circuit boards (PCBs) to generate enriched rare metal concentrate. *Journal of Industrial and Engineering Chemistry*, 21, pp. 805–813. https://doi.org/10.1016/j.jiec.2014.04.016

Nekouei, R. K., Pahlevani, F., Rajarao, R., Golmohammadzadeh, R., Sahajwalla, V. (2018). Two-step pre-processing enrichment of waste printed circuit boards: Mechanical milling and physical separation. *Journal of Cleaner Production*, 184, pp. 1113–1124. https://doi.org/10.1016/j.jclepro.2018.02.250

Nie, C. chen, Jiang, S. qi, Li, X. guang, Lyu, X. jun, Zhang, Y. qing, Zhu, X. nan. (2023). Surface characteristic driven in waste printed circuit boards flotation: Floatability mechanism of resin and glass fiber in non-metallic component. *Process Safety and Environmental Protection*, 178 (August), pp. 360–369. https://doi.org/10.1016/j.psep.2023.08.024

Ogunniyi, I. O. (2009). *Investigation into Froth Flotation for The Beneficiation of Printed Circuit Board Comminution Fines* (Issue September). University of Pretoria.

Ogunniyi, I. O., Vermaak, M. K. G. (2009). Investigation of froth flotation for beneficiation of printed circuit board comminution fines. *Minerals Engineering*, 22 (4), pp. 378–385. https://doi.org/10.1016/j.mineng.2008.10.007

Otsuki, A., Bryant, G. (2015). Characterization of the interactions within fine particle mixtures in highly concentrated suspensions for advanced particle processing. *Advances in Colloid and Interface Science*, 226, pp. 37–43. https://doi.org/10.1016/j.cis.2015.07.005

Sajjad, M., Otsuki, A. (2022). Correlation between Flotation and Rheology of Fine Particle Suspensions. *Metals*, 12 (2), pp. 1–31. https://doi.org/10.3390/met12020270

Shen, Z., Zhang, Q. (2022). Hydrophobic agglomeration behavior of rhodochrosite fines Co-induced by oleic acid and shearing. *Separation and Purification Technology*, 282 (PB), 120115. https://doi.org/10.1016/j.seppur.2021.120115

Van Oss, C. J. (2003). Long-range and short-range mechanisms of hydrophobic attraction and hydrophilic repulsion in specific and aspecific interactions. *Journal of Molecular Recognition*, 16 (4), pp. 177–190. https://doi.org/10.1002/jmr.618

Vidyadhar, A., Das, A. (2013). Enrichment implication of froth flotation kinetics in the separation and recovery of metal values from printed circuit boards. *Separation and Purification Technology*, 118, pp. 305–312. https://doi.org/10.1016/j.seppur.2013.07.027

Wang, C., Sun, R., Xing, B. (2021). Copper recovery from waste printed circuit boards by the flotation-leaching process optimized using response surface methodology. *Journal of the Air and Waste Management Association*, 71 (12), pp. 1483–1491. https://doi.org/10.1080/10962247.2021.1874568

Yang, S., Wu, Y., Chai, W., Cao, Y. (2023). Effect of energy input on surface properties and dispersion of diaspore and kaolinite in flotation process. *Chemical Engineering and Processing – Process Intensification*, 192 (June), 109518. https://doi.org/10.1016/j.cep.2023.109518

Yangshuai, Q., Yongfu, Y., Lingyan, Z., Weijun, P., Yupeng, Q. (2017). Dispersion and agglomeration mechanism of flaky graphite particles in aqueous solution. *Journal of Dispersion Science and Technology*, 38 (6), pp. 796–800. https://doi.org/10.1080/01932691.2016.1198703

Yao, Y., Bai, Q., He, J., Zhu, L., Zhou, K., Zhao, Y. (2020). Reverse flotation efficiency and mechanism of various collectors for recycling waste printed circuit boards. *Waste Management*, 103, pp. 218–227. https://doi.org/10.1016/j.wasman.2019.12.030

Yu, Y., Cheng, G., Ma, L., Huang, G., Wu, L., Xu, H. (2017). Effect of agitation on the interaction of coal and kaolinite in flotation. *Powder Technology*, 313, pp. 122–128. https://doi.org/10.1016/j.powtec.2017.03.002

Zhu, X. nan, Ni, Y., Wang, D. zhang, Zhang, T., Qu, S. juan, Qiao, F. ming, Ren, Y. guang, Nie, C. chen, Lyu, X. jun, Qiu, J., Li, L. (2020). Effect of dissociation size on flotation behavior of waste printed circuit boards. *Journal of Cleaner Production*, 265, 121840. https://doi.org/10.1016/j.jclepro.2020.121840

Zhu, X. nan, Zhang, L. ye, Dong, S. ling, Kou, W. jia, Nie, C. chen, Lyu, X. jun, Qiu, J., Li, L., Liu, Z. xue, Wu, P. 2020. Mechanical activation to enhance the natural floatability of waste printed circuit boards. *Waste Management*, 109, pp. 222–230. https://doi.org/10.1016/j.wasman.2020.05.008

Geosciences and Engineering, Vol. 12, No.2 (2024), pp. 109–127.
https://doi.org/10.33030/geosciences.2024.02.009

COMPARATIVE ANALYSIS OF MULTI-CRITERIA DECISION-MAKING TECHNIQUES FOR GROUNDWATER POTENTIAL MAPPING IN HIGHLAND OF ERITREA

KABRAL MOGOS ASGHEDE[1, 2]*, JÁNOS VÁGÓ[3]
[1]**Institute of Geography and Geoinformatics, University of Miskolc, Hungary;*
kabralmogos@gmail.com
[2]*Department of Civil Engineering,*
Mai-Nefhi College of Engineering and Technology, Eritrea
[3]*Institute of Geography and Geoinformatics, University of Miskolc, Hungary*
janos.vago@uni-miskolc.hu
[1]https://orcid.org/0009-0001-4846-6788
[2]https://orcid.org/0000-0001-6811-6649

Abstract: This study employs an approach that integrates geospatial techniques with the Analytical Hierarchy Process (AHP) and Fuzzy-AHP to identify groundwater potential zones in Debarwa. Seven environmental parameters significantly influencing groundwater potential were selected for analysis: geology, soil, lineament density, rainfall, land use/land cover, drainage density, and slope. A comparative study between the two methods was employed using Geographic Information System (GIS) and Remote Sensing (RS) tools. The thematic layers for each parameter were created and subsequently weighed through pairwise comparisons based on the AHP and Fuzzy-AHP methodology. Consistency tests were conducted to ensure the reliability of the assigned weights. The final weighted overlay map classified the groundwater potential into four categories: poor, good, very good, and excellent. The spatial distribution of the area coverage for the potential zone of AHP and Fuzzy-AHP fall under the good and very good zones. The results for good and very good use of AHP are 74.68% and 24.88%, respectively, with 80.12% and 19.87% for Fuzzy-AHP. While both methods produce comparable results, Fuzzy-AHP exhibits a slight advantage in refining classification accuracy by incorporating degrees of membership rather than rigid classifications. For future work the research recommends incorporating other methods to validate the accuracy and robustness of the outcome. Finally, the preliminary resulting outcome provides a valuable tool for Eritrea water resource department to prioritize areas for detailed groundwater exploration and management.

Keywords: *Groundwater potential, Analytical Hierarchy Process (AHP), Fuzzy-AHP, Geographic Information System (GIS), Water resource management, Eritrea*

1. INTRODUCTION

Groundwater, a vital global water resource, is stored within soil and rock pores following rainwater infiltration through permeable zones (Upwanshi et al., 2023). Unlike surface water, groundwater is often less vulnerable to environmental contamination. It is a crucial source, contributing to 34% of the world's water supply, particularly for agricultural and industrial purposes (Verma and Patel, 2021), with approximately 2.5 billion people worldwide depending on groundwater (Swarnim et al., 2023). Its

significance cannot be overstated, especially in arid and semi-arid regions where low rainfall and climate change exacerbate demand (Tegegne et al., 2024). Therefore, assessing this precious resource is essential in coping with the world's high demand.

The objective of this research is to identify groundwater potential zones in the central region of Eritrea around Debarwa city. However, identifying groundwater recharge zones poses challenges due to temporal and spatial variations in recharge rates (Moeck et al., 2020). Consequently, a comprehensive understanding of groundwater dynamics is essential for accurate potential zone mapping. While various exploration methods exist, including geophysical, remote sensing, and geological techniques (AL Deep et al., 2021; Araffa et al., 2023; El-Sayed and Elgendy, 2024), their application may be limited by time and cost considerations, particularly in low-income countries (Agogue Feujio et al., 2024). To address this, researchers have increasingly turned to integrated approaches combining Geographical Information Systems (GIS), Remote Sensing (RS), AHP and Fuzzy-AHP approaches for rapid and accurate assessments (Y. Liu et al., 2020; Sajil Kumar et al., 2022; Shelar et al., 2023; Swarnim et al., 2023). These approaches are also widely used in other disciplines to delineate dam sites and landslides (Bastola et al., 2024; Ksantini et al., 2024; Y. Liu et al., 2020). GIS has become a suitable mapping tool due to its capability to integrate, visualize, model, and manage large amounts of data. Combining data layers in GIS and analyzing them with RS-derived information allows potential recharge zones to be mapped effectively (Kpiebaya et al., 2022).

This study focuses on delineating Groundwater Potential Zones (GWPZ) in the Debarwa catchment area using RS, geospatial, AHP, and Fuzzy-AHP approaches. Where this method is tested for the first time in the study area that will fill the existing traditional exploration methods. Integrating these methodologies with hydrological, topographical, and geological parameters has yielded promising results in various regions (Gidafie et al., 2024; Mohammed et al., 2024). For instance, in the Murredu watershed in India, AHP combined with Fuzzy-AHP found higher area potential with a moderate zone of 73.53% for AHP and 76.55% for Fuzzy-AHP (Raja Shekar and Mathew, 2023). Similarly, in Tunisia's Regueb region, the AHP approach, alongside literature-derived weights, produced comparable results (Hassini et al., 2023). Furthermore, integrating Fuzzy-AHP with GIS-RS mapping in Sevathur region in Tamil Nadu, India, proves good technique for potential groundwater exploration (Prapanchan et al., 2024). Therefore, this method has sound acceptance worldwide.

The urgency of this research came from the critical need for proper groundwater management in Debarwa catchment area. Overexploitation, variable rainfall patterns, and geological factors have led to rapid groundwater depletion, impacting the socio-economic livelihoods of communities reliant on groundwater use for agriculture. Moreover, the study area has a knowledge gap for the scientific assessment of groundwater potential. Therefore, the gap is believed to be solved by employing such research. Seven environmental features have been selected for investigation: geology, soil, lineament density, land use/land cover, rainfall, drainage density, and slope. The outcome of this study produces a map showing different potential groundwater zones. These maps are expected to show preliminary information on the potential zones to the decision-making bodies and water resource

departments. In addition, the approach of the scientific result will contribute to overcoming the challenges of groundwater exploration.

2. STUDY AREA

The study area encompasses Debarwa, situated within the administrative zone of the Southern region (Debub local name) in Eritrea *(Figure 1)*.

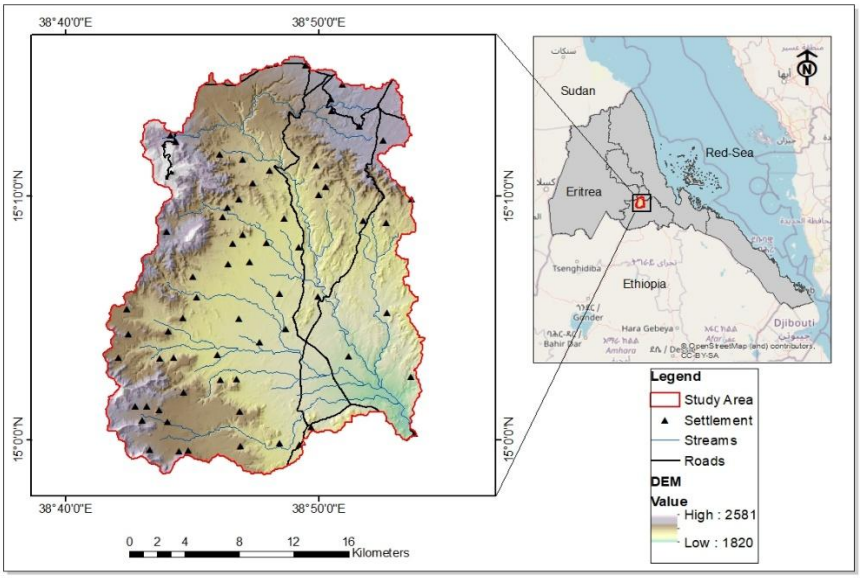

Figure 1
Location map of the study area in Eritrea

It is located 25 km south of Asmara, the capital city of Eritrea at a geographic coordinate of $38^{0}50$'E and $15^{0}10$'N. The study area has a total of 506 km^2 area coverage with an elevation of 1926 m above mean sea level. Debarwa experiences distinct climatic conditions, with July marking the wettest month and December the driest, whereas January typically emerges as the coldest month. The region exhibits a variable rainfall pattern, with an average annual precipitation of 53.36 mm and a mean temperature of 23.21 °C (https://weatherandclimate.com/eritrea/debub#t1). The area geology comprises deeply eroded/weathered and strongly lateritized Neoproterozoic low-grade volcanic units underlying tertiary flood basalts and granite-type rocks (Teklay, 2006). The occurrence and movement of groundwater in the area are primarily controlled by nature, spatial distribution, orientation, and penetration depth of secondary permeability, which are tension or shear fractures (Solomon and Quiel, 2006). Recharge may occur to the groundwater system directly from rainfall and indirectly from surface flows over the area drained by the Mereb River drainage system. Most of the wells in the area are protected and inaccessible except for some privately owned agricultural wells. Thus, measuring the well's water level in the field site is difficult.

As a historic market town in central Eritrea, Debarwa boasts a population of approximately 25,000 residents. The local economy predominantly revolves around agriculture, with residents cultivating crops such as teff, finger millet, maize, and barley. However, the agricultural sector faces significant challenges due to climate change impacts and the overexploitation of groundwater resources, leading to water scarcity issues. These challenges underscore the critical importance of effective water resource management strategies in sustaining agricultural production and livelihoods within the region.

3. MATERIALS AND METHODS

There are different methods for assessing groundwater potential mapping (GWPM), but none have been used in the study area. Therefore, this research focused on a comparative analysis of AHP and Fuzzy-AHP in combination with GIS and RS for the assessment of GWPM. These methods can integrate expert judgment with quantitative data and handle subjective decisions (Burayu et al., 2025). The study area, the Debarwa catchment, has a complex geological and environmental factor that requires expert analysis judgment. Where the three experts who have participated in the judgment have a sound knowledge of the study area with geological and hydrogeological background. The methodology for identifying groundwater potential zones involves significant steps in both methods. These include the selection of parameters influencing groundwater recharge processing and layer analysis in GIS environment (Kouaied et al., 2025). Then, a pairwise comparison between selected parameters using the AHP and Fuzzy-AHP. Finally, the weighted overlay method produces the groundwater potential zone map. Based on the available data, the critical influential groundwater controlling parameters selected in this study are geology, soil, lineament density, rainfall, land use/land cover, slope and drainage density. All those parameters have a direct and major contributing factor for groundwater recharge which is categorized as a main input figures in many similar studies.

The selected environmental parameters were processed using the ArcGIS Pro software and reclassified based on classes within the catchment area. All selected environmental parameters with 30-meter resolution were projected to the WGS 1984 UTM Zone 37N coordinate system to align with the local coordinate. Parameters derived from DEM are drainage density, lineament density, and slope, and were classified into five distinct classes based on expert judgment. Geology, rainfall, and soil classifications were based on the specific characteristics of the study area. The land-use and land cover data were downloaded from Sentinel-2 10 m land use/land cover time series. This systematic classification ensures that each parameter is appropriately represented and standardized for subsequent analysis, facilitating the accurate delineation of groundwater potential zones within the Debarwa catchment area.

The data were collected from different sources as discussed below. Geological data were obtained from the Ministry of Mining and Energy in Asmara, Eritrea, at a spatial resolution of 30 m in shapefile format. Soil is another important parameter used to contribute to groundwater occurrence where its data is brought from Asmara Agricultural Department. The lineament is traced manually from the digital elevation

model (DEM) hillshade from Shuttle Radar Topographic Mission (SRTM) and generates new map (Asghede et al., 2025). The data was downloaded from Earth Explorer website (https://earthexplorer.usgs.gov/) and converted to line density to make it raster. The Asmara International Airport meteorological station collected rainfall for the period of 1992 to 2022, where the average rainfall data of this period is used in this research.

Many hydrological processes are regulated by land use and land cover, where their importance is crucial (Bhadran et al., 2022). Based on Sentinel-2 satellite imagery classification scheme there are seven classes within the study area. Moreover, the slope map is generated from DEM which was downloaded from the Earth Explorer website. The drainage density parameter has an inversely proportional relationship with the permeability of the underlying rocks (Ifediegwu, 2022). It is generated by creating fill, flow direction, and flow accumulation using the hydrogeological tools in the ArcGIS environment. Then, from the flow accumulation stream order and stream to feature were created. Finally, to convert to raster line density was prepared. By integrating data from these diverse sources and making a comparison between the methods, the study ensures reasonable information for groundwater potential assessment, facilitating good analysis for decision-making processes.

AHP is a widely adopted method across various disciplines worldwide (Arefin, 2020; Kassa et al., 2023). The AHP facilitates calculating each criterion's weight or rank based on priority by pairwise comparisons of the datasets (Saaty and Katz, 1990). These comparisons are made using the Saaty scale, which ranges from 1 to 9 *(Table 1)*, allowing for a systematic assessment of the relative importance of each parameter in the groundwater potential analysis. The selected environmental control parameters were compared through expert judgment and literature review. The consistency test was conducted to ensure the judgment matrix, as recommended by previous studies (Ozegin et al., 2024; Zenande et al., 2024). Following Saaty's principle, the consistency ratio was calculated using the ratio of the consistency index and random index [Equation (2)]

$$CI = \frac{(\lambda - n)}{(n-1)} \tag{1}$$

$$CR = \frac{CI}{RI} \tag{2}$$

where CI is the consistency index, CR is the consistency ratio, RI is the random index, λ is the maximum principal eigenvalue, and n is the number of compared elements or parameters. The values depend on the number of selected parameters *(Table 2)*. In this study, seven factors were chosen as groundwater control parameters. According to Saaty's guideline, for a parameter with seven factors, the consistency ratio should ideally be less than 0.1 (Agogue Feujio et al., 2024). *Equation (1)* was employed to verify this criterion. Subsequently, the weight of each factor was generated, serving as a basis for prioritizing parameters in the development of the groundwater potential map.

Table 1

Saaty's scale for relative importance (Saaty and Katz, 1990)

Range of importance	Description
1	Equal importance
3	Moderate importance
5	Essential
7	Very strong importance
9	Extreme importance
2, 4, 6, 8	Intermediate values between adjacent scale values

Subclass ranking was assigned based on percolation rates to contribute water to underground storage, drawing insights from various literature reviews and expert judgments (Popalzai et al., 2023; Sharma and Singh, 2025). The final weight was determined by multiplying each subclass's rank by the feature's weight. The weighted overlay tool from the spatial analysis toolbox of ArcGIS Pro was utilized to sum all the weighted features and generate the required groundwater potential map. Ensuring uniformity in cell size and projection systems across all layers is imperative to facilitate a smooth analysis process (Thanh et al., 2022).

Table 2

Saaty's ratio index for different n values

N	3	4	5	6	7	8
RI	0.58	0.89	1.12	1.24	1.32	1.41

Fuzzy-AHP method is an extension of the traditional AHP that incorporates fuzzy logic to the expert judgment to handle uncertainty and subjectivity in decision-making (Liu et al., 2020). Based on the expert surveys and literature reviews, pairwise comparisons of parameters were made based on their relative importance. Then, pairwise comparisons of values were converted to fuzzy triangular numbers to account for uncertainty in expert opinions. Using fuzzy logic operations, the fuzzy weight of each parameter is computed. The final weight of each parameter is found by converting the fuzzy weights to crisp values, that is the defuzzification process (Githinji et al., 2022). Finally, criterion weights are obtained after ensuring the consistency ratio. This weight is integrated into the spatial layer of each parameter to generate a groundwater potential map.

4. RESULTS AND DISCUSSION

Both AHP and Fuzzy approaches' results revealed that all the selected environmental parameters have almost similar outcomes *(Tables 3, 4)*. The weights of the parameters are determined in the following descending order based on the expert judgment: geology, soil, lineament density, rainfall, land use/land cover (LULC), slope, and drainage density. The first four parameters contribute more than ten percent of the total weight *(Table 5)*.

Table 3

AHP Pairwise comparison matrix

Parameter	Slope	DD	LD	LU/ LC	Soil	Rainfall	Geology	Normalized principal eigenvector	AHP Weight
Geology	4.0	4.0	2.0	3.0	2	3.0	1	29.3%	0.29
Soil	3.0	4.0	2.0	3.0	1	2.0	0.50	21.8%	0.22
LD	3.0	4.0	1	3.0	0.5	2.0	0.50	17.8%	0.18
Rainfall	3	3	0.5	2	0.5	1	0.33	12.4%	0.12
LULC	2	2	0.33	1	0.3	0.50	0.33	8.1%	0.08
Slope	1	2.0	0.33	0.5	0.3	0.33	0.25	6.1%	0.06
Drainage density	0.50	1	0.25	0.5	0.25	0.33	0.25	4.6%	0.05

Table 4

Fuzzy-AHP Pairwise comparison matrix

Classes	Soil			LD			Rainfall			LULC			Slope			DD			Geology			Weight %
Geology	1	2	3	1	2	3	2	3	4	2	3	4	3	4	5	3	4	5	1	1	1	27.95
Soil	1	1	1	1	2	3	1	2	3	2	3	4	2	3	4	3	4	5	0.3	0.5	1	21.53
LD	0.3	0.5	1	1	1	1	1	2	3	2	3	4	2	3	4	3	4	5	0.3	0.5	1	18.19
Rainfall	0.3	0.5	1	0.3	0.5	1	1	1	1	1	2	3	2	3	4	2	3	4	0.3	0.3	0.5	12.95
LULC	0.25	0.3	0.5	0.25	0.3	0.5	0.3	0.5	1	1	1	1	1	2	3	1	2	3	0.3	0.3	0.5	8.38
Slope	0.25	0.3	0.5	0.25	0.3	0.5	0.25	0.3	0.5	0.3	0.5	1	1	1	1	1	2	3	0.2	0.3	0.3	6.22
DD	0.2	0.25	0.3	0.2	0.25	0.3	0.25	0.3	0.5	0.3	0.5	1	0.3	0.5	1	1	1	1	0.2	0.3	0.3	4.76

The result of the two methods revealed that geology has the highest weight comprising 29.3% for AHP and 27.95% for Fuzzy-AHP of the total weight *(Tables 3, 4)*. The geological classification encompasses four subclasses *(Figure 2a)*: low-grade metamorphic rocks, very low-grade metamorphic rocks, trap series plateau basalt, and granite-type rocks. These geological features are crucial in groundwater recharge dynamics (Moon et al., 2024). Following geology, the soil is ranked as the second-highest contributing factor, weighing 21.8% and 21.53% for AHP and Fuzzy-AHP methods, respectively. The classification includes loam and light clay soils *(Figure 2b)*, indicating favorable conditions for water infiltration and seepage to the saturated zone with minimal hindrance.

Lineament density is another significant factor, weighing 17.8% and 18.19% for AHP and Fuzzy, respectively. The cracks and fissures in the rocks facilitate water percolation, further aiding in aquifer recharge (Daher et al., 2011). These structural features are classified into five categories ranging from 1.53 to 7.67 km per km^2 to standardize and simplify the analysis for use in the multi-criteria evaluation models

(Figure 3a), which enhances groundwater recharge by providing pathways for water movement through the subsurface. Furthermore, rainfall intensity emerges as a critical determinant, particularly in arid and semi-arid regions like the study area. With spatially and temporally limited distribution, the area experiences relatively low average annual rainfall, ranging from 34.3 to 47.3 mm (Figure 3b), based on readings from national meteorological stations. Consequently, rainfall variability is categorized as the fourth contributing factor, representing 12.4% and 12.95% for AHP and Fuzzy-AHP, respectively *(Table 5)*.

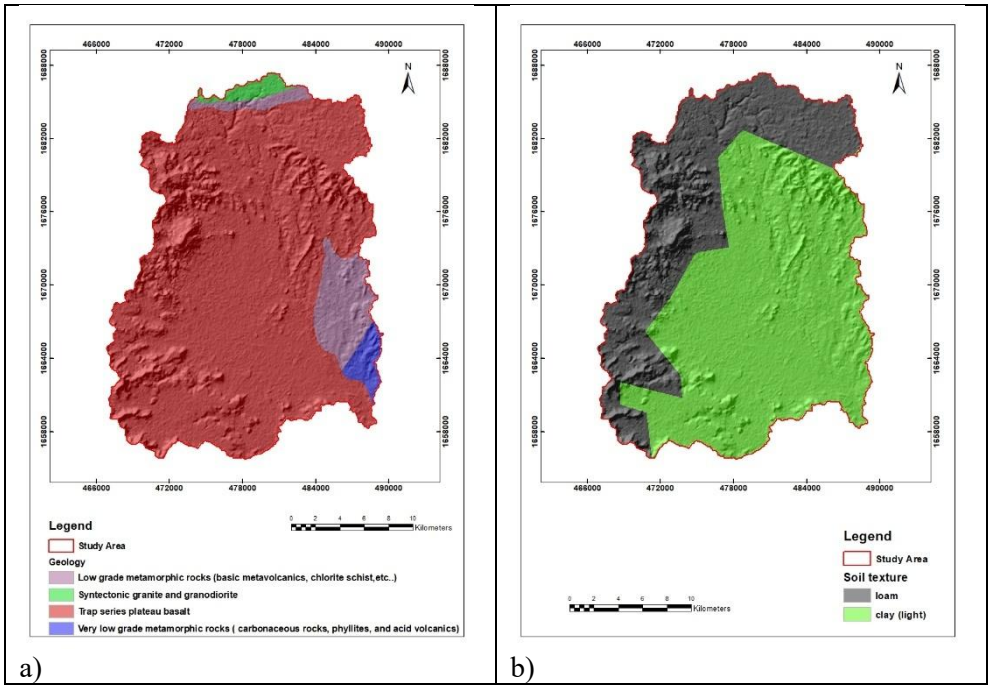

Figure 2

Geology setting (a) and soil map of the study area (b)

LULC is categorized into seven classes based on Sentinal-2 classification scheme: water, trees, rangeland, flooded vegetation, crops, built-in areas, and bare grounds *(Figure 4a)*. LULC collectively contributes 8.1% and 8.38% for AHP and Fuzzy-AHP to the total weight of the parameters influencing groundwater potential. Slope variation is identified as another crucial controlling factor for groundwater recharge *(Figure 4b)*. With slope degrees ranging from 4.15 to 62.2, steep slopes contribute to high runoff, limiting water infiltration into the aquifer (Kaliraj et al., 2014). In this study, the slope weight is determined to be nearly 6% for both approaches.

Similarly, drainage density, derived from the DEM using a flow accumulation threshold of 500 cells as the Critical Source Area (CSA), plays a significant role in

the groundwater potential analysis. Higher drainage density is generally associated with reduced groundwater recharge, as it promotes surface runoff and limits the infiltration of water into the subsurface (Oikonomidis et al., 2015). The weight assigned to drainage density is found to be 4.6% and 4.76% for AHP and Fuzzy-AHP, with subclass classifications ranging from 0.645 to 3.22 km per km^2 using the natural breaks classification methods which identifies best arrangement values *(Figure 5a)*. The collective influence of these environmental parameters underscores their cumulative effect on the potential groundwater resources of the study area. The overall result for the good groundwater potential zone using AHP and Fuzzy-AHP is 74.68% and 80.12% respectively. The second significant areal coverage is for a very good zone with 24.88% for AHP and 19.87% for Fuzzy-AHP *(Figure 5b)*. The two extreme zones show below 1% results in both methods. As shown in *Figure 6*, the overall groundwater potential zone map coverage area falls under the good zone and some parts of the western and northern parts show very good potential.

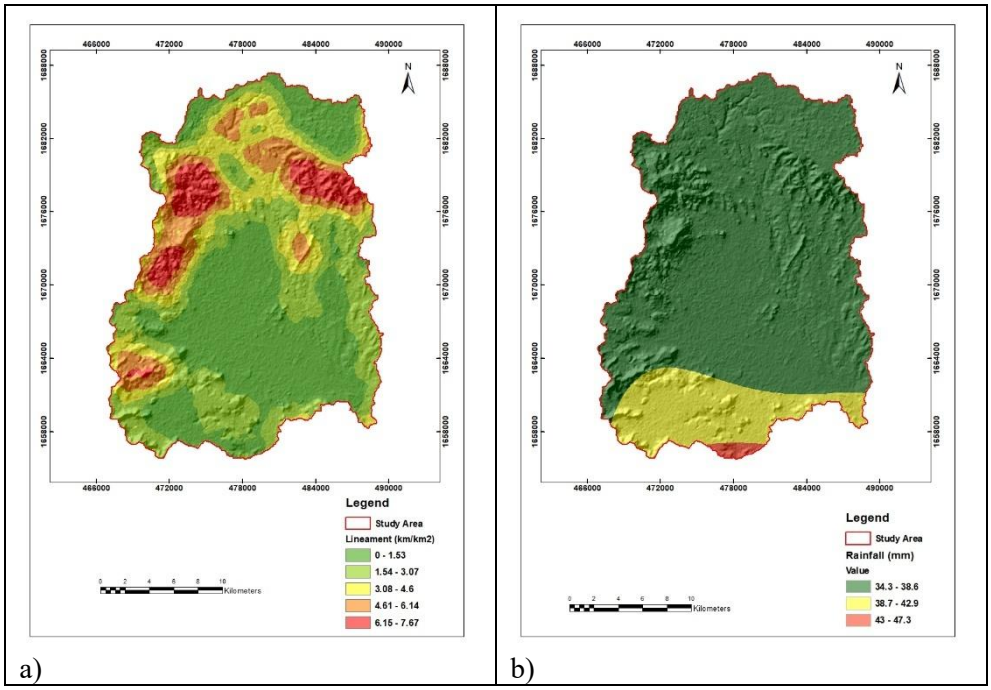

Figure 3
Lineament density map (a) and rainfall map (b)

For future use to allocate resources accurately, it is essential to map the groundwater potential zone (Sarkar et al., 2024). The Debarwa catchment study area encompasses many villages that largely depend on agricultural practices. Identification of groundwater potential zone maps using AHP and Fuzzy-AHP methods will solve the

traditional groundwater exploration techniques. The comparative analysis of the AHP and Fuzzy-AHP methods for groundwater potential mapping demonstrates that both approaches yield highly similar results in terms of weight factor distribution and areal coverage classification. Geology emerges as the most influential factor in both methods, with AHP assigning it a weight of 29.3% and Fuzzy-AHP slightly lower at 27.95%. Similarly, soil holds the second-highest weight in both methods, at 21.8% and 21.53% for AHP and Fuzzy-AHP, respectively. The least influential parameter, drainage density, exhibits a negligible difference between the two methods, with values of 4.6% for AHP and 4.76% for Fuzzy-AHP. Both methods rely on pairwise comparisons and expert judgment to determine the relative importance of parameters, where due to this reason could be the weighted factors are closely aligned.

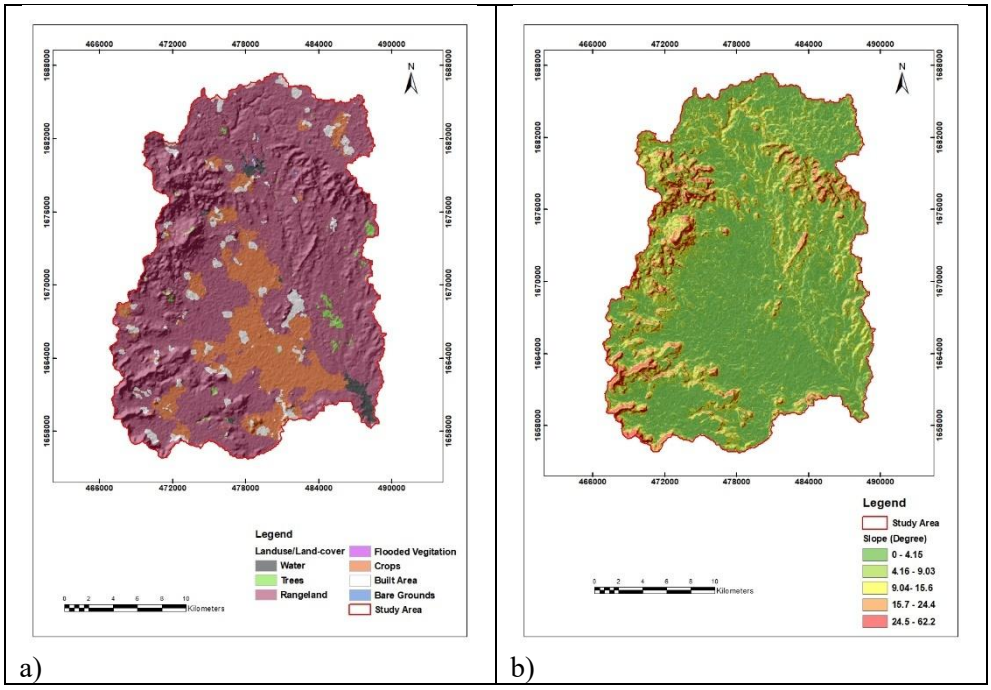

Figure 4

Landuse/Landcover map (a) and slope map (b)

AHP results show that the "good" and "very good" potential zones cover 74.68% and 24.88%, respectively, while Fuzzy-AHP assigns 80.12% to "good" and 19.87% to "very good". Notably, the percentage of areas classified as "poor" and "excellent" is extremely low in both methods, with Fuzzy-AHP producing slightly more refined classifications. The higher percentage of "good" zones in the Fuzzy-AHP approach suggests that this method provides a smoother and more continuous representation of groundwater potential, reducing abrupt transitions between zones. This could be

attributed to the ability of fuzzy logic to handle uncertainty and ambiguity more effectively than the crisp decision-making process in AHP. Similar works were observed in different research activities that predict accurate groundwater potential results (Tiwari et al., 2024; Zewdie et al., 2024). For future work, the result of this research can be cross-checked with machine learning and other methods upon having enough ground data as it was tested for the same task accurately in different research areas (Das and Saha, 2022; Lee et al., 2020; R. Liu et al., 2022; Nguyen et al., 2024). Additionally, the concentration of the result around the good potential zone map can open further discussion of research, which can validate its reality with ground truth data for future work. While both methods produce comparable results, Fuzzy-AHP exhibits a slight advantage in refining classification accuracy by incorporating degrees of membership rather than rigid classifications. These findings underscore the importance of the AHP and Fuzzy AHP methods in optimizing groundwater exploration. By utilizing these advanced techniques, decision-makers can significantly shorten the exploration process compared to traditional methods, which are often time-consuming and less efficient. AHP and Fuzzy AHP provide a systematic and data-driven approach, improving accuracy in identifying potential groundwater sources and reducing uncertainties in the exploration phase.

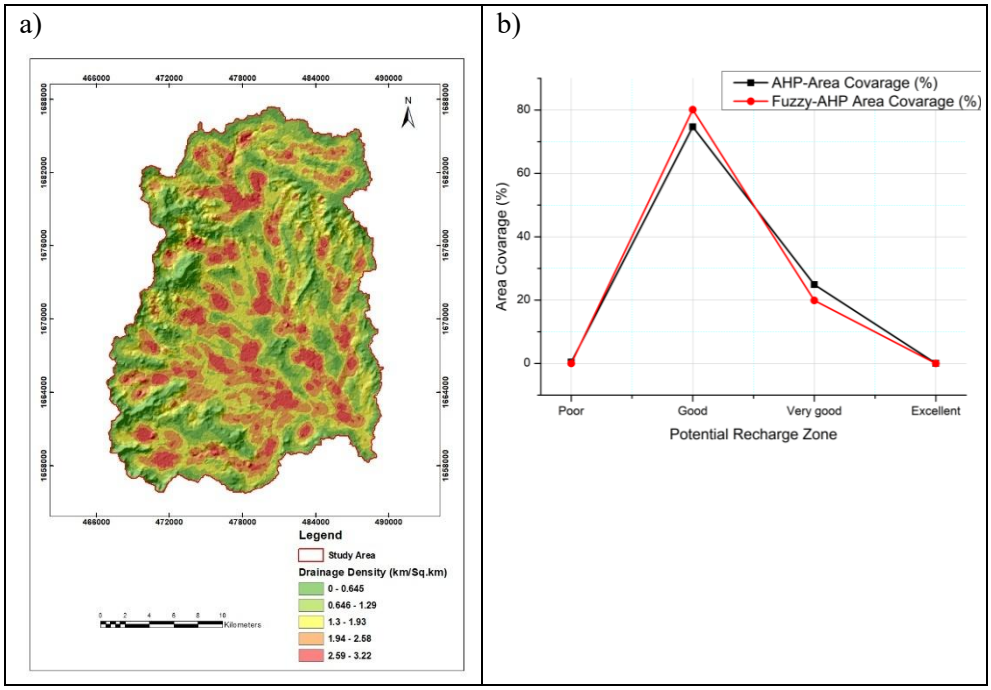

Figure 5

Drainage density map (a) and graphical comparison between AHP and Fuzzy-AHP results (b)

Table 5

The groundwater parameters are ranked in descending order

Factor	Weight (%) AHP	Weight(%) Fuzzy-AHP	Rank
Geology	29.3	27.95	1st
Low grade metamorphic rocks (basic metavolcanics, chlorite schist, etc..)			4
Very low-grade metamorphic rocks (carbonaceous rocks, phyllites, and acid volcanics)			3
Trap series plateau basalt			2
Syntectonic granite and granodiorite			1
Soil	21.8	21.53	2nd
Loam			2
Clay (light)			1
Lineament density (km/km^2)	17.8	18.19	3rd
(6.15–7.67)			5
(4.61–6.14)			4
(3.08–4.6)			3
(1.54–3.07)			2
(0–1.53)			1
Rainfall (mm)	12.4	12.95	4th
(43–47.3)			3
(38.7–42.9)			2
(34.3–38.6)			1
Landuse/landcover	8.1	8.38	5th
Water			7
Trees			6
Rangeland			5
Flooded vegitation			4
Crops			3
Built area			2
Bare grounds			1
Slope (degree)	6.1	6.22	6th
(0–4.15)			5
(4.16–9.03)			4
(9.04–15.6)			3
(15.7–24.4)			2
(24.5–62.2)			1
Drainage density (km/km^2)	4.6	4.76	7th
(0–0.645)			5
(0.646–1.29)			4
(1.3–1.93)			3
(1.94–2.58)			2
(2.59–3.22)			1

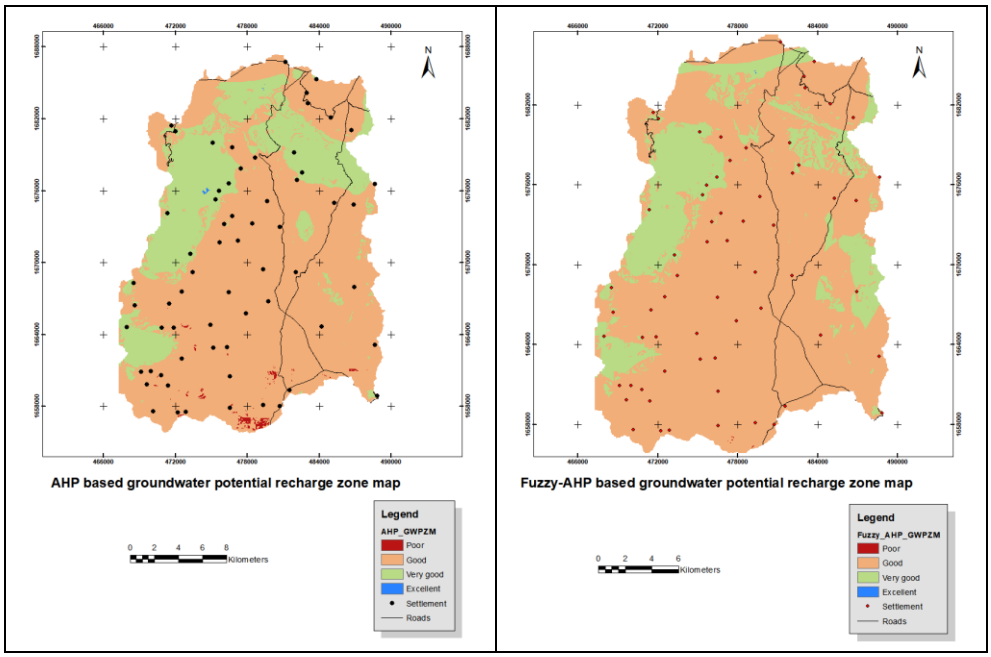

Figure 6

Groundwater classification maps: AHP (a) Fuzzy-AHP (b)

5. CONCLUSIONS

The research addresses a comparative analysis between AHP and Fuzzy-AHP approaches for groundwater potential mapping in the study area. The primary objective was to delineate the groundwater potential zone in the Debarwa catchment area. This delineation will assist in a better groundwater management strategy for the water resource department in Eritrea. The comparative evaluation of AHP and Fuzzy-AHP for groundwater potential mapping indicates that both methods provide nearly identical weight factor distributions and classification outputs, demonstrating their reliability in groundwater assessment. The similarity in results is likely due to the structured nature of AHP, the well-defined relationships among environmental parameters, and the dominant influence of geology and soil. While Fuzzy-AHP provides a more refined transition between classes, the overall impact of fuzzification remains minimal in this study. Despite the close agreement, Fuzzy-AHP slightly enhances classification precision by better handling uncertainties, making it preferable in studies where data ambiguity is a concern. On the other hand, AHP remains a viable and computationally efficient alternative, particularly in cases where a straightforward decision-making process is sufficient. Ultimately, the choice between AHP and Fuzzy-AHP depends on the specific study requirements. The results have some limitations such as a lack of validation, subjective expert input, and potential for bias in parameter weighting. With the availability of enough ground truth data, further research is recommended using other techniques such as frequency

ratio and machine learning approaches to fill these gabs. Finally, by providing a comprehensive understanding of groundwater potential zones, this study facilitates informed decision-making and sustainable management practices to optimize groundwater resources within the Debarwa catchment area.

ACKNOWLEDGMENTS

The authors express their sincere gratitude to the Eritrean Mapping and Information Center (EMIC), the Asmara Water Resources Department, Asmara Ministry of Agriculture, Asmara airport metrological station and Ministry of Energy and Mines Eritrea for their support in facilitating the collection of necessary data.

REFERENCES

Agogue Feujio, D. H., Aretouyap, Z., Tchato, S. C., Ngog II Legrand, C., Djomdi, E., Nague Madadjeu, N., Nguimfack Nguimgo, C., and Ndinchout Kpoumie, A. (2024). Application of analytical hierarchy process to assess groundwater potential for a sustainable management in the Menoua Division. *Heliyon*, 10 (2). https://doi.org/10.1016/j.heliyon.2024.e24310

AL Deep, M., Araffa, S. A. S., Mansour, S. A., Taha, A. I., Mohamed, A., and Othman, A. (2021). Geophysics and remote sensing applications for groundwater exploration in fractured basement: A case study from Abha area, Saudi Arabia. *Journal of African Earth Sciences*, 184. https://doi.org/10.1016/j.jafrearsci.2021.104368

Araffa, S. A. S., Hamed, H. G., Nayef, A., Sabet, H. S., AbuBakr, M. M., and Mebed, M. El. (2023). Assessment of groundwater aquifer using geophysical and remote sensing data on the area of Central Sinai, Egypt. *Scientific Reports*, 13 (1). https://doi.org/10.1038/s41598-023-44737-9

Arefin, R. (2020). Groundwater potential zone identification at Plio-Pleistocene elevated tract, Bangladesh: AHP-GIS and remote sensing approach. *Groundwater for Sustainable Development*, 10. https://doi.org/10.1016/j.gsd.2020.100340

Asghede, K. M., Vágó, J., & Pecsmány, P. (2025). Integrated approach for lineament extraction in assessing groundwater potential: a case study in the highlands of Eritrea. *Acta Geographica Debrecina Landscape & Environment Series*, 19 (1), https://doi.org/10.21120/LE/19/1/1

Bastola, S., Shakya, B., Seong, Y., Kim, B., and Jung, Y. (2024). AHP and FAHP-based multi-criteria analysis for suitable dam location analysis: a case study of the Bagmati Basin, Nepal. *Stochastic Environmental Research and Risk Assessment.* https://doi.org/10.1007/s00477-024-02799-9

Bhadran, A., Girishbai, D., Jesiya, N. P., Gopinath, G., Krishnan, R. G., and Vijesh, V. K. (2022). A GIS based Fuzzy-AHP for delineating groundwater potential zones in tropical river basin, southern part of India. *Geosystems and Geoenvironment*, 1, 93. https://doi.org/10.1016/j.geogeo.2022.10

Burayu, D. G., Karuppannan, S., and Shuniye, G. (2025). Geospatial mapping of groundwater potential zones using multi-criteria decision analysis and GIS fuzzy logic in Dabus Sub-Basin, western Ethiopia. *Quaternary Science Advances*, 18, 100275. https://doi.org/10.1016/j.qsa.2025.100275

Daher, W., Pistre, S., Kneppers, A., Bakalowicz, M., and Najem, W. (2011). Karst and artificial recharge: Theoretical and practical problems. A preliminary approach to artificial recharge assessment. *Journal of Hydrology*, 408(3–4), 189–202. https://doi.org/10.1016/j.jhydrol.2011.07.017

Das, R., and Saha, S. (2022). Spatial mapping of groundwater potentiality applying ensemble of computational intelligence and machine learning approaches. *Groundwater for Sustainable Development*, 18. https://doi.org/10.1016/j.gsd.2022.100778

El-Sayed, H. M., and Elgendy, A. R. (2024). Geospatial and geophysical insights for groundwater potential zones mapping and aquifer evaluation at Wadi Abu Marzouk in El-Nagila, Egypt. *Egyptian Journal of Aquatic Research.* https://doi.org/10.1016/j.ejar.2023.12.008

Gidafie, D., Nedaw, D., and Azagegn, T. (2024). Integrated remote sensing and geographic information system overlay analysis for groundwater potential evaluation using AHP and fuzzy AHP: Southern sections of the western Afar rift margin and associated rift floor. *Groundwater for Sustainable Development*, 26. https://doi.org/10.1016/j.gsd.2024.101310

Githinji, T. W., Dindi, E. W., Kuria, Z. N., and Olago, D. O. (2022). Application of analytical hierarchy process and integrated fuzzy-analytical hierarchy process for mapping potential groundwater recharge zone using GIS in the arid areas of Ewaso Ng'iro – Lagh Dera Basin, Kenya. *HydroResearch*, 5, 22–34. https://doi.org/10.1016/j.hydres.2021.11.001

Hassini, E., Hassini, S., Hamdi, M., and Hamed, Y. (2023). Satellite remote sensing and GIS-based multi-criteria analysis for assessing the groundwater recharge potential zones in the Regueb basin (central Tunisia). Applied Geomatics, 15 (1), 29–43. https://doi.org/10.1007/s12518-022-00478-4

Ifediegwu, S. I. (2022). Assessment of groundwater potential zones using GIS and AHP techniques: a case study of the Lafia district, Nasarawa State, Nigeria. *Applied Water Science*, 12(1). https://doi.org/10.1007/s13201-021-01556-5

Kaliraj, S., Chandrasekar, N., and Magesh, N. S. (2014). Identification of potential groundwater recharge zones in Vaigai upper basin, Tamil Nadu, using GIS-based analytical hierarchical process (AHP) technique. *Arabian Journal of Geosciences, 7(4), 1385–1401.* https://doi.org/10.1007/s12517-013-0849-x

Kassa, A. K., Tessema, N., Habtamu, A., Girma, B., and Adane, Z. (2023). Identifying groundwater recharge potential zone using analytical hierarchy process (AHP) in the semi-arid Shinile watershed, Eastern Ethiopia. *Water Practice and Technology*, 18(11), 2834–2850. https://doi.org/10.2166/wpt.2023.168

Kouaied, A., Msaddek, M. H., Zghibi, A., Barrek, A., Pistre, S., and Chenini, I. (2025). Groundwater recharge zone mapping in a coastal mediterranean aquifer applying fuzzy and analytical hierarchy process and frequency ratio: A case study of northeast Tunisia. *In Journal of African Earth Sciences* (Vol. 224). Elsevier Ltd. https://doi.org/10.1016/j.jafrearsci.2025.105537

Kpiebaya, P., Amuah, E. E. Y., Shaibu, A. G., Baatuuwie, B. N., Avornyo, V. K., and Dekongmen, B. W. (2022). Spatial assessment of groundwater potential using Quantum GIS and multi-criteria decision analysis (QGIS-AHP) in the Sawla-Tuna-Kalba district of Ghana. *Journal of Hydrology: Regional Studies*, 43. https://doi.org/10.1016/j.ejrh.2022.101197

Ksantini, F., Sdiri, A., Aydi, A., Almeida-Ñauñay, A. F., Achour, H., and Tarquis, A. M. (2024). A comparative study based on AHP and fuzzy logic approaches for landslide susceptibility zoning using a GIS-based multi-criteria decision analysis. *Euro-Mediterranean Journal for Environmental Integration.* https://doi.org/10.1007/s41207-024-00552-w

Lee, S., Hyun, Y., Lee, S., and Lee, M. J. (2020). Groundwater potential mapping using remote sensing and GIS-based machine learning techniques. *Remote Sensing*, 12 (7). https://doi.org/10.3390/rs12071200

Liu, R., Li, G., Wei, L., Xu, Y., Gou, X., Luo, S., and Yang, X. (2022). Spatial prediction of groundwater potentiality using machine learning methods with Grey Wolf and Sparrow Search Algorithms. *Journal of Hydrology*, 610. https://doi.org/10.1016/j.jhydrol.2022.127977

Liu, Y., Eckert, C. M., and Earl, C. (2020). A review of fuzzy AHP methods for decision-making with subjective judgements. *In Expert Systems with Applications*, Vol. 161. https://doi.org/10.1016/j.eswa.2020.113738

Moeck, C., Grech-Cumbo, N., Podgorski, J., Bretzler, A., Gurdak, J. J., Berg, M., and Schirmer, M. (2020). A global-scale dataset of direct natural groundwater recharge rates: A review of variables, processes and relationships. *Science of the Total Environment*, 717. https://doi.org/10.1016/j.scitotenv.2020.137042

Mohammed, M. A. A., Mohammed, S. H., Szabó, N. P., and Szűcs, P. (2024). Geospatial modeling for groundwater potential zoning using a multi-parameter analytical hierarchy process supported by geophysical data. *Discover Applied Sciences*, 6(3). https://doi.org/10.1007/s42452-024-05769-6

Moon, S. H., Park, C., Kim, H. C., Kim, Y., Kee, W. S., Lee, C. M., and Kim, S. (2024). Groundwater productivity analysis with geology in the Geumgang River region, Korea. *Geosciences Journal.* https://doi.org/10.1007/s12303-024-0047-8

Nguyen, H. D., Nguyen, Q. H., Dang, D. K., Nguyen, T. G., Truong, Q. H., Nguyen, V. H., Bretcan, P., Șerban, G., Bui, Q. T., and Petrisor, A. I. (2024). Integrated machine learning and remote sensing for groundwater potential mapping in the Mekong Delta in Vietnam. *Acta Geophysica.* https://doi.org/10.1007/s11600-024-01331-5

Oikonomidis, D., Dimogianni, S., Kazakis, N., and Voudouris, K. (2015). A GIS/ Remote Sensing-based methodology for groundwater potentiality assessment in Tirnavos area, Greece. *Journal of Hydrology*, 525, 197–208. https://doi.org/10.1016/j.jhydrol.2015.03.056

Ozegin, K. O., Ilugbo, S. O., and Akande, O. N. (2024). Leveraging geospatial technology and AHP for groundwater potential zonation in parts of South and North-Central Nigeria. *Sustainable Water Resources Management*, 10(4). https://doi.org/10.1007/s40899-024-01124-0

Popalzai, A., Ahmadi, H., Rahmani, A. B., and Pekkan, E. (2023). Delineation of Groundwater Potential Zones Using Multi-Criteria Decision Analysis: *The Case of Balkh Province, Northern Afghanistan*, 41. https://doi.org/10.3390/iecg2022-14817

Pourghasemi, H. R., Sadhasivam, N., Yousefi, S., Tavangar, S., Ghaffari Nazarlou, H., and Santosh, M. (2020). Using machine learning algorithms to map the groundwater recharge potential zones. *Journal of Environmental Management*, 265. https://doi.org/10.1016/j.jenvman.2020.110525

Prapanchan, V. N., Subramani, T., and Karunanidhi, D. (2024). GIS and fuzzy analytical hierarchy process to delineate groundwater potential zones in southern parts of India. *Groundwater for Sustainable Development*, 25. https://doi.org/10.1016/j.gsd.2024.101110

Prasad, P., Loveson, V. J., Kotha, M., and Yadav, R. (2020). Application of machine learning techniques in groundwater potential mapping along the west coast of India. *GIScience and Remote Sensing*, 735–752. https://doi.org/10.1080/15481603.2020.1794104

Raja Shekar, P., and Mathew, A. (2023). Assessing groundwater potential zones and artificial recharge sites in the monsoon-fed Murredu river basin, India: An integrated approach using GIS, AHP, and Fuzzy-AHP. *Groundwater for Sustainable Development*, 23. https://doi.org/10.1016/j.gsd.2023.100994

Saaty, T. L., and Katz, J. M. (1990). How to make a decision: The Analytic Hierarchy Process. *European Journal of Operational Research*, Vol. 48.

Sajil Kumar, P. J., Elango, L., and Schneider, M. (2022). GIS and AHP Based Groundwater Potential Zones Delineation in Chennai River Basin (CRB), India. *Sustainability (Switzerland)*, 14(3). https://doi.org/10.3390/su14031830

Sarkar, S. K., Alshehri, F., Shahfahad, Rahman, A., Pradhan, B., and Shahab, M. (2024). Mapping groundwater potentiality by using hybrid machine learning models under the scenario of climate variability: a national level study of Bangladesh. *Environment, Development and Sustainability.* https://doi.org/10.1007/s10668-024-04687-2

Sharma, A., and Singh, K. (2025). Determining prospective zones for groundwater recharge using remote sensing, GIS, and AHP modelling techniques: an investigation of the Mandi district in Himachal Pradesh, India. *Environmental Earth Sciences*, 84(5). https://doi.org/10.1007/s12665-025-12137-z

Sharma, B., and Pandey, A. A. (2023). Application of geospatial techniques and analytic hierarchy process in delineating ground water potential zones: a case study from the Southeastern part of Bihar, India. *International Journal of Energy and Water Resources.* https://doi.org/10.1007/s42108-023-00260-1

Shelar, R. S., Nandgude, S. B., Pande, C. B., Costache, R., El-Hiti, G. A., Tolche, A. D., Son, C. T., and Yadav, K. K. (2023). Unlocking the hidden potential: groundwater zone mapping using AHP, remote sensing and GIS techniques. *Geomatics, Natural Hazards and Risk*, 14(1). https://doi.org/10.1080/19475705.2023.2264458

Solomon, S., and Quiel, F. (2006). Groundwater study using remote sensing and geographic information systems (GIS) in the central highlands of Eritrea. *Hydrogeology Journal*, 14 (5), pp. 729–741. https://doi.org/10.1007/s10040-005-0477-y

Swarnim, Tripathi, J. N., Sonker, I., and Tiwari, S. P. (2023). Groundwater potential mapping in Trans Yamuna Region, Prayagraj, using combination of geospatial technologies and AHP method. *Environmental Monitoring and Assessment*, 195 (11). https://doi.org/10.1007/s10661-023-11934-y

Tegegne, A. M., Lohani, T. K., and Eshete, A. A. (2024). Groundwater potential delineation using geodetector based convolutional neural network in the Gunabay watershed of Ethiopia. *Environmental Research*, 242. https://doi.org/10.1016/j.envres.2023.117790

Teklay, M. (2006). Neoproterozoic arc-back-arc system analog to modern arc-back-arc systems: Evidence from tholeiite-boninite association, serpentinite mudflows and across-arc geochemical trends in Eritrea, southern Arabian-Nubian shield. *Precambrian Research*, 145 (1–2), pp. 81–92. https://doi.org/10.1016/j.precamres.2005.11.015

Thanh, N. N., Chotpantarat, S., Trung, N. H., Ngu, N. H., and Muoi, L. Van. (2022). Mapping groundwater potential zones in Kanchanaburi Province, Thailand by integrating of analytic hierarchy process, frequency ratio, and random forest. *Ecological Indicators*, 145. https://doi.org/10.1016/j.ecolind.2022.109591

Tiwari, R. N., Kushwaha, V. K., and Sharma, B. (2024). Delineation of suitable sites for water conservation structures and groundwater potential zones using integration of remote sensing and GIS: a case study of Central India. *Arabian Journal of Geosciences*, 17 (5). https://doi.org/10.1007/s12517-024-11949-w

Upwanshi, M., Damry, K., Pathak, D., Tikle, S., and Das, S. (2023). Delineation of potential groundwater recharge zones using remote sensing, GIS, and AHP approaches. *Urban Climate*, 48. https://doi.org/10.1016/j.uclim.2023.101415

Verma, N., and Patel, R. K. (2021). Delineation of groundwater potential zones in lower Rihand River Basin, India using geospatial techniques and AHP. *Egyptian Journal of Remote Sensing and Space Science*, 24 (3), pp. 559–570. https://doi.org/10.1016/j.ejrs.2021.03.005

Yousif, M., Sabet, H. S., Ghoubachi, S. Y., and Aziz, A. (2018). Utilizing the geological data and remote sensing applications for investigation of groundwater occurrences, West El Minia, Western Desert of Egypt. *NRIAG Journal of Astronomy and Geophysics*, 7 (2), pp. 318–333. https://doi.org/10.1016/j.nrjag.2018.07.002

Zenande, N., Adesola, G. O., Madi, K., and Gwavava, O. (2024). Groundwater potential assessment in the Eastern Cape, South Africa, using analytical hierarchical process (AHP) technique. *Sustainable Water Resources Management*, 10 (6). https://doi.org/10.1007/s40899-024-01166-4

Zewdie, M. M., Kasie, L. A., and Bogale, S. (2024). Groundwater potential zones delineation using GIS and AHP techniques in upper parts of Chemoga watershed, Ethiopia. *Applied Water Science*, 14 (4). https://doi.org/10.1007/s13201-024-02119-0

Geosciences and Engineering, Vol. 12, No. 2 (2024), pp. 128–138.
https://doi.org/10.33030/geosciences.2024.02.010

THE INFLUENCE OF GYPSUM QUALITY, AUTOCLAVING TIME AND GRINDING ON THE SETTING TIME OF α--HEMIHYDRATE

ÁRON FÖLDESI[1]*, JÓZSEF FAITLI[2]
[1]**Faculty of Earth and Environmental Sciences and Engineering, University of Miskolc*
aron.foldesi@baumit.hu
[2]*Faculty of Earth and Environmental Sciences and Engineering, University of Miskolc*
jozsef.faitli@uni-miskolc.hu

Abstract: The aim of this work is to model the influence of grinding and gypsum quality on the setting time of α-hemihydrate using the design of experiments (DoE) method. The setting time of the gypsum binder is an important property determined by the particle size distribution of hemihydrate crystals. In this study, the change in particle size and setting time of hemihydrate was observed by varying the particle size and crystal water content of raw flue gas desulfurization (FGD) gypsum, duration of autoclaving and grinding intensity as model parameters.

Keywords: *gypsum, setting time, hemihydrate, particle size, design of experiments*

1. INTRODUCTION

Gypsum is a type of mineral that belongs to the group of hydrous sulfate minerals, the dihydrate of calcium sulfate (DH, $CaSO_4 \cdot 2H_2O$). Calcium and sulfate ions are bound together in ring-shaped units whose three-dimensional arrangement results in tubular structures. The water molecules of the crystal water are incorporated into these tubes. This water is only loosely bound by adsorption, dehydration is possible in all stoichiometric ratios (Feldmann and Demopoulos, 2012).

When gypsum is heat-treated at a temperature of over 90 °C a calcium sulfate-hemihydrate is formed, with the following reaction (Van Diessche et al. 2016):

$$CaSO_4 + 2H_2O + dQ = CaSO_4 + \frac{1}{2}H_2O + \frac{3}{2}H_2O \quad (1)$$

According to the above equation, calcium sulfate hemihydrate is formed in crystalline form by removing three-quarters of the gypsum crystal water.

β-hemihydrate, which is produced by a dry process (e.g. calcination), is a fine crystalline form resulting from the rapid transformation of the dihydrate. The α-hemihydrate (α-HH), the fully formed hexagonal crystal form, is produced by wet heat treatment (e.g. autoclaving) with steam (Yin and Yang, 2020; Guan et al., 2021). The dehydration process can be divided into two phases: the first is the induction period

of α-hemihydrate, in which the crystal water content of the sample changes only slightly, and the second is the crystal growth of α-HH, in which the crystal water content decreases significantly (Fu et al., 2018; Singh et al., 2007). Upon solidification, the α-hemihydrate can form a stronger crystal structure than the β-form, which is why it is mainly used as a raw material for gypsum binders and floor leveling compounds (Levry and Williamson, 1994).

Due to the hydraulic properties of the hemihydrate, rehydration occurs when it is mixed with water, which is the opposite of the previous equation:

$$CaSO_4\frac{1}{2}H_2O + \frac{3}{2}H_2O = CaSO_4 + 2H_2O + dQ \quad (2)$$

The hydration of hemihydrate is a three step process of solving of hemihydrate, dihydrate seed crystal formation and growing of dihydrate beside inner hydration. The hemihydrate dissolves moderately in water (0.65 g/100 ml) and quickly reaches saturation. The solubility of the dihydrate (0.24 g/100 ml) is only a fraction of the solubility of the hemihydrate, but they form crystallization nuclei during the binding reaction, then precipitate and grow rapidly into an interlocking crystalline mass, significantly accelerating the setting time (Levry and Williamson, 1994).

The influence of the particle size of the α-hemihydrate is also important for the setting time. According to the literature, most authors agree that fine gypsum binders with a higher specific surface area set faster (Baohong et al., 2010; Pan et al. 2007).

2. MATERIAL AND METHODS

2.1. Preparation of hemihydrate

During the model experiments, the gypsum binder samples were prepared in a pilot laboratory equipped for the production and testing of α-hemihydrate. The equipment of the experimental laboratory is identical to the production technology for industrial α-hemihydrate, the steps of the process are presented in *Figure 1*.

During test preparation, the gypsum is treated with water, press adhesive (ground α-hemihydrate) and crystal-forming additives in such a way that molded bodies with a defined density for the autoclaving process are produced by pressing, which survive the autoclaving process undamaged. During production, two additives are added to the mixture to promote the formation of α-hemihydrate crystals under hydrothermal conditions.

The technological advantage of the α-gypsum production process lies in the production of raw gypsum blocks with a certain press density. During pressing, test blocks with a weight of ~6.5 kg are produced.

From a crystallographic point of view, the central technological step in the production of hemihydrate from flue gas desulfurization (FGD) gypsum is the pressurized heat treatment in the autoclave, in which the energy required to remove the water of crystallization is provided by the condensation heat of the steam. The α-hemihydrate, which consists of large, dense crystals, can only be produced in the hydrothermal reaction by controlling the temperature and pressure correctly. The

conversion must be carried out in such a way that complete recrystallization takes place in the solution phase. During the experiments, the recrystallization of the hemihydrate was carried out in a Systec D90 autoclave modified for this purpose.

The process objective of drying α-hemihydrate gypsum is to reduce the water physically present in the molded parts to less than 0.5% by weight at the end of the hydrothermal heat treatment. The air temperature is above 110 °C during the entire drying period; however, the surface temperature of the gypsum blocks remains below 100 °C, even though the air temperature is above 100 °C. During the test, the bricks were dried in a Memmert UF110PLUSZ programmable laboratory dryer.

The aim of grinding is to produce a stable and homogeneous α-hemihydrate with a granulometrically defined particle size distribution (PSD) and specific surface area. Grinding was carried out in a Retsch ZM200 centrifugal mill, in which the grinding intensity can be adjusted by setting the rotor speed between 8000 and 18000 rpm.

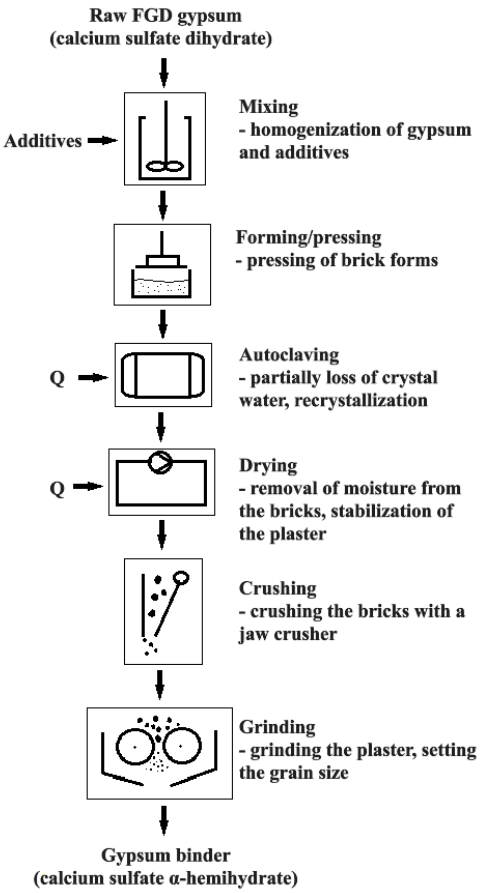

Figure 1
Experimental technology of α-hemihydrate production

2.2. Design of Experiments

The starting material for the model tests was FGD gypsum from the Mátra power plant. The data of the samples used are shown in *Table 1*.

Table 1

Characteristics of the selected gypsum samples

Quality Class	Test No.	Gypsum crystal water [%]	PSD d10 [µm]	PSD d50 [µm]	PSD d90 [µm]	Spec. surface area [cm^2/g]
Poor Crystal Water content between 19.5–19.8%	1	19.58	18.26	47.08	77.94	1205
	2	19.64	18.45	47.21	77.97	1185
	3	19.69	18.24	47.11	77.94	1219
	4	19.54	17.86	46.59	77.33	1233
	5	19.59	18.08	46.35	77.71	1218
	6	19.45	18.29	46.47	77.25	1214
	7	19.59	18.24	47.11	77.94	1219
Medium Crystal Water content between 19.9–20.2%	8	20.14	22.65	48.04	77.54	1178
	9	20.12	22.22	47.88	77.07	1324
	10	19.99	22.53	47.97	77.96	1152
	11	20.08	22.52	48.31	77.92	1199
	12	20.10	22.64	48.29	77.89	1230
	13	20.04	22.69	47.81	77.46	1169
	14	20.05	23.15	48.92	78.55	1283
	15	20.12	22.69	47.81	77.46	1169
High Crystal Water content between 20.3–20.6%	16	20.40	21.42	47.12	75.09	1362
	17	20.36	21.65	47.67	75.69	1356
	18	20.31	21.14	46.7	74.75	1253
	19	20.35	21.17	47.62	75.68	1362
	20	20.42	21.87	47.56	75.39	1355
	21	20.35	21.29	47.57	75.67	1330
	22	20.47	21.17	47.62	75.68	1362

As it can be seen from the table, low-grade gypsum is characterized by a low crystal water content, which is due to the high proportion of inert constituents and the low dihydrate content. These samples also typically exhibited a heterogeneous, broad particle size distribution, with more fine and larger particles. High-quality gypsum, on the other hand, is characterized by high crystal water content and a more homogeneous particle size distribution.

In the DoE study, the particle size distribution (PSD) and the setting time of the α-hemihydrate binder were observed by varying three model parameters in three

stages. The selected parameters were the crystal water content of the raw gypsum, the autoclaving time as independent variables and the grinding intensity (mill speed) as a dependent variable.

The first important step in the design phase was to determine the three levels, as these determine whether the variables have a significant influence on the target values. If the repeatability of these measurements is poor, the error within one experimental set-up will be greater than between two experimental set-ups. If there is no significant difference between the experimental setups compared to the target values, then we cannot say anything about the effect of these input variables. To create the model, a total of 9 experimental setups were defined, with each run repeated once and 4 runs repeated three times to create accurate model equations.

After all the experiments have been carried out, a linear mathematical model is fitted to the target values as a function of the three parameters. The model equation was as follows:

$$y = a_0 + a_1 * x_1 + a_2 * x_2 + a_3 * x_3 \tag{3}$$

The evaluation started by checking the significance of the changes in the model to determine whether they are meaningful changes or just the noise of our measurements. The average variance of the two sets of replicates was taken and used in two-sample t-tests to verify if there was a significant difference between the results. The aim was to perform the regression calculations and determine the best fit using the analytical solution. It had an analytical solution given by the equation below:

$$a_i = (X^T * X)^{-1} * X^T * y \tag{4}$$

X was the matrix of input parameters and y the target values. The calculations provide the values b and a_i of the model equation for the respective target variable. These steps were then repeated with the next target variable. After calculating the values b and a_i, a prediction could be made for each run. Based on the predicted values and the measured values, the performance of the model could be determined. By calculating the values for the total, external and internal variance (residual error), the coefficient of determination (CoD.) and coefficient of correlation (CoC.) of the model could also be determined. The proportion of the total variance that could be explained by the regression was calculated using the explained variance (external variance/total variance).

2.3. Measurement Methods

During the measurements, the crystal morphology of the recrystallized bricks examined with SEM images so that the relationships obtained from the model equations could be better interpreted. A Phenom ProX scanning electron microscope was used to make the images. Since both the raw gypsum and the α-hemihydrate binders were fine powders, the particle size distribution (PSD) and specific surface area were determined using laser diffraction. The setting times were determined using the

standard Vicat method. The Vicat needle is cylindrical and moves in a vertical, scaled guide, penetrating a plaster mass located in a mold. The start of setting time is defined as the time at which the needle penetrates no further than a certain distance (20 mm) from the top of the sample. The end of setting time is defined as the time at which the needle no longer penetrates at all (EN 13279-2:2014; Sleiman et al., 2010).

3. RESULTS

The parameters used in the model and the measured results of the settings are summarized in *Table 2*.

Table 2

Parameters (settings) and measured PSD and setting time values of the model

	Model parameters (Settings)			**Target values (Measured values)**				
Exp. No.	**Gypsum crystal water [%]**	**Auto-claving time [hours]**	**Grinding intensity [10^3rpm]**	**PSD d10 [µm]**	**PSD d50 [µm]**	**PSD d90 [µm]**	**Set. Start [min]**	**Set. End [min]**
1	19.58	6.5	16	2.62	13.60	37.06	4.6	6.6
2	19.64	6.5	16	2.51	13.40	35.21	3.9	5.8
3	19.69	6.5	16	2.37	11.88	31.93	3.9	6.1
4	19.54	7.5	12	2.97	17.00	47.98	6.2	8.4
5	19.59	7.5	12	3.30	17.53	49.15	7.1	8.5
6	19.45	8.5	8	3.70	23.36	59.03	7.08	9.82
7	19.59	8.5	8	3.54	21.55	55.87	6.7	9.5
8	20.14	6.5	12	3.01	16.18	40.48	4.7	6.5
9	20.12	6.5	12	2.95	15.09	39.55	5.0	6.9
10	19.99	6.5	12	2.94	15.62	43.50	4.8	7
11	20.08	7.5	12	2.99	15.47	41.76	5.2	7.4
12	20.10	7.5	12	3.02	14.38	37.32	4.8	6.9
13	20.04	8.5	12	3.09	15.77	41.76	4.8	7.6
14	20.05	8.5	12	3.03	16.53	42.28	4.6	7.5
15	20.12	8.5	12	2.97	17.30	40.25	4.8	6.9
16	20.40	6.5	8	3.51	21.63	49.69	5.3	8.1
17	20.36	6.5	8	3.44	21.33	50.64	5.0	7.9
18	20.31	7.5	12	3.01	16.13	42.76	5.1	7.5
19	20.35	7.5	12	3.00	16.49	42.87	5.1	7.1
20	20.42	8.5	16	2.64	13.09	33.06	3.8	5.6
21	20.35	8.5	16	2.39	12.33	30.31	3.5	4.8
22	20.47	8.5	16	2.41	12.24	30.50	3.3	4.7

The model equations of PSD values and setting time were determined using the measurement results (target values) and model parameters (settings), and then the predicted values were calculated using these equations. The measured and predicted values are summarized in *Table 3*.

Table 3

Measurement and predicted PSD and setting time values

	Measured values					Predicted values				
Exp. No.	**PSD d10 [µm]**	**PSD d50 [µm]**	**PSD d90 [µm]**	**Set. Start [min]**	**Set. End [min]**	**PSD d10 [µm]**	**PSD d50 [µm]**	**PSD d90 [µm]**	**Set. Start [min]**	**Set. End [min]**
1	2.62	13.60	37.06	4.6	6.6	2.52	12.55	35.59	4.6	6.3
2	2.51	13.40	35.21	3.9	5.8	2.51	12.47	35.13	4.5	6.2
3	2.37	11.88	31.93	3.9	6.1	2.51	12.41	34.74	4.4	6.1
4	2.97	17.00	47.98	6.2	8.4	3.08	17.29	46.53	5.9	8.1
5	3.30	17.53	49.15	7.1	8.5	3.08	17.23	46.15	5.8	8.0
6	3.70	23.36	59.03	7.08	9.82	3.65	22.10	57.85	7.2	10.0
7	3.54	21.55	55.87	6.7	9.5	3.63	21.91	56.78	7.0	9.8
8	3.01	16.18	40.48	4.7	6.5	2.97	16.25	41.34	4.7	6.9
9	2.95	15.09	39.55	5.0	6.9	2.98	16.28	41.49	4.8	6,9
10	2.94	15.62	43.50	4.8	7	2.99	16.44	42.49	5.0	7.2
11	2.99	15.47	41.76	5.2	7.4	3.01	16.59	42.38	5.0	7.2
12	3.02	14.38	37.32	4.8	6.9	3.01	16.56	42.23	5.0	7.1
13	3.09	15.77	41.76	4.8	7.6	3.05	16.90	43.28	5.2	7.4
14	3.03	16.53	42.28	4.6	7.5	3.05	16.89	43.20	5.2	7.4
15	2.97	17.30	40.25	4.8	6.9	3.04	16.80	42.66	5.1	7.3
16	3.51	21.63	49.69	5.3	8.1	3.47	20.34	49.39	5.4	8.0
17	3.44	21.33	50.64	5.0	7.9	3.47	20.39	49.70	5.5	8.1
18	3.01	16.13	42.76	5.1	7.5	2.98	16.29	40.62	4.6	6.8
19	3.00	16.49	42.87	5.1	7.1	2.98	16.24	40.31	4.5	6.7
20	2.64	13.09	33.06	3.8	5.6	2.47	11.98	30.31	3.5	5.1
21	2.39	12.33	30.31	3.5	4.8	2.48	12.07	30.85	3.6	5.3
22	2.41	12.24	30.50	3.3	4.7	2.47	11.92	29.93	3.4	5.1

After grinding the experimental hemihydrate bricks, the particle size distribution of the hemihydrate correlates well (coefficient of correlation (CoC.) between 91.8% and 96.7%) with the grinding intensity, and the influence of raw material gypsum quality was also significant. In the experiments, the autoclaving time had no significant influence on the particle distribution values. The model equations defined for the PSD values were as follows:

$$y_{d10} = 6.96 - 0.13 * x_{\text{cw gypsum}} - 0.13 * x_{\text{grinding intensity}} \quad (5)$$

$$y_{d50} = 54.02 - 1.30 * x_{\text{cw gypsum}} - 1.11 * x_{\text{grinding intensity}} \quad (6)$$

$$y_{d90} = 222.24 - 7.67 * x_{\text{cw gypsum}} - 2.52 * x_{\text{grinding intensity}} \quad (7)$$

The equation states that the higher the crystal water content of the gypsum and the higher the grinding intensity, the more widely dispersed the values obtained, i.e. the finer the material. In the equation, the d10 and d90 particle size values of the hemihydrate samples, where the raw material gypsum was of a higher quality class, decreased compared to the results of the lower quality with low crystal water content. Since the specific surface area of the three selected raw gypsums increased with quality, this observation supports the results of Fu et al. (2018). According to their study, the gypsum samples with smaller particle sizes generally had a higher proportion of smaller hemihydrate crystals. The induction time of recrystallization was significantly reduced as the smaller gypsum crystals offer a larger relative specific surface area and more nucleation sites.

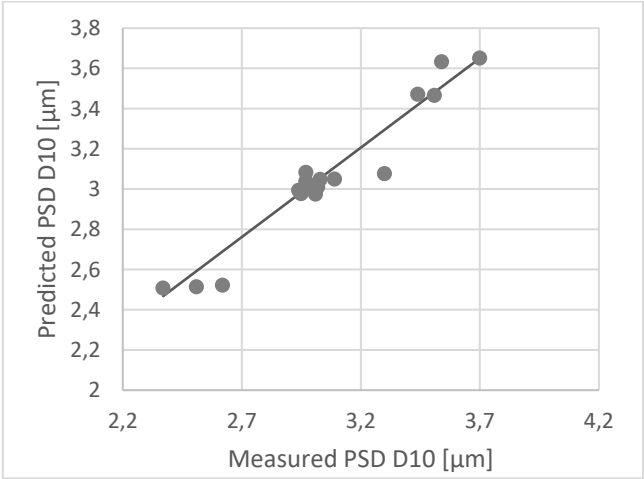

Figure 2
Performance of the d10 model (CoD. = 94.7%, CoC. = 97.3%)

The equation of the d50 model showed an interesting picture, as the median of PSD (d50) increased with increasing crystal water and gypsum quality. The probable reason for this was that the size distribution of the low-quality gypsum had the smallest d10 values and the largest d90 values, so this feature could also influence the particle size of the resulting hemihydrate due to the wide distribution. This was also confirmed by the SEM images of the crystal morphology of the hemihydrate. As can be seen in the images, the hemihydrate produced from low-quality FGD gypsum was a heterogeneous system consisting of needle-like and larger crystals, while the α-

hemihydrate produced from gypsum with a high crystal water content formed a more homogeneous system consisting mainly of developed crystals. Therefore, the particle size of the hemihydrate was more uniform and the size consistency better when it was produced from high-quality gypsum with a higher amount of crystal water.

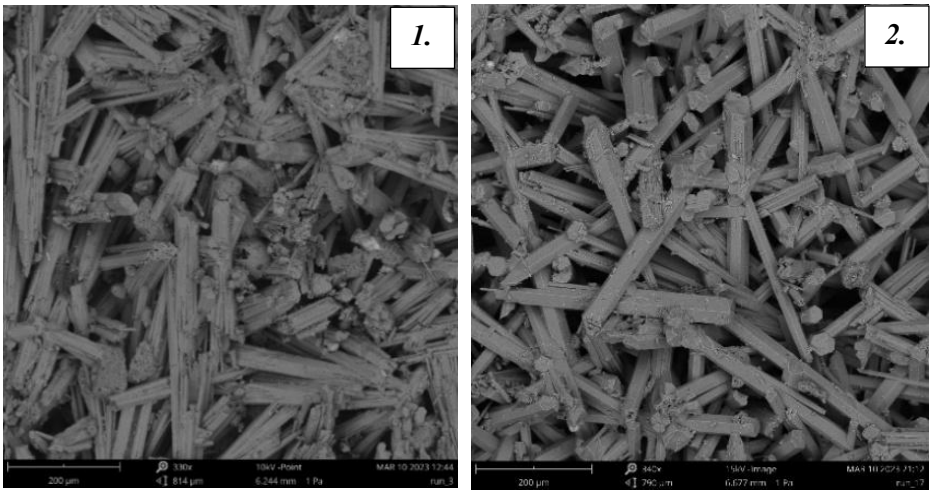

Figure 3
SEM Pictures of HH, 1. from low-quality; 2. from high-quality gypsum

The results of the setting time model show that the setting times are accelerated if we increase the mill speed (rpm) and thereby increase the specific surface area of the α-hemihydrate. The crystal water content of the FGD gypsum was also significant; the effect was negative according to the model, i.e. increasing it accelerated the setting time. The equation for the start and end of the setting time was as follows:

$$y_{set.\ time\ start} = 39.66 - 1.62 * x_{\text{cw gypsum}} - 0.27 * x_{\text{grinding intesity}} \quad (8)$$

$$y_{set.\ time\ end} = 45.83 - 1.74 * x_{\text{cw gypsum}} - 0.40 * x_{\text{grinding intesity}} \quad (9)$$

For this reason, according to the model, hemihydrate from a higher quality class leads to faster setting. In addition, the model showed that an inferior α-hemihydrate with low crystal water content and a larger particle size range generally sets more slowly.

4. DISCUSSION AND CONCLUSIONS

As part of the DoE, a total of 9 settings were defined to create the model and a total of 22 repeat tests were carried out. The equations were set up reliably and with good performance.

According to the equations, the quality of the raw material and the grinding intensity (grinding speed) significantly influence the particle size distribution (PSD). Hemihydrate made from high-quality gypsum had a finer and more uniform particle

size consistency (steeper PSD). The autoclaving time had no significant influence on the particle size values at these setting levels.

In the second part of the study, we were able to model the setting time in good correlation (CoC. between 90.5% and 96.0%) with the crystal water content of the raw gypsum and grinding intensity. The model equation for the setting time showed that the crystal water content of the α-hemihydrate has the greatest influence, but the grinding intensity also plays an important role. Hemihydrate binders with higher water content, which are produced at a higher mill speed, generally have faster setting times.

Due to the closure of power plants in the course of decarbonization, the availability and affordability of FGD gypsum are continuously decreasing. As FGD gypsum is one of the main raw materials for gypsum binders, the industry might be forced to use lower-quality gypsum. The α-hemihydrate is one of the materials most affected by this problem in the gypsum industry, as one of the basic requirements for sufficient and controllable recrystallization in autoclaves is high gypsum quality and thus the lowest possible inert content. The aim of this study is to investigate that this limitation can unfortunately affect important gypsum binder properties such as setting time and particle size. Eliminating such effects and maintaining a stable binder quality could therefore be one of the most important technical challenges for the gypsum industry in the future.

REFERENCES

Van Driessche, A , Stawski, M. , Benning, L. and Kellermeier M. (2016). Calcium Sulfate Precipitation Throughout Its Phase Diagram. *New Perspectives on Mineral Nucleation and Growth, Springer*, pp. 227–231. https://doi.org/10.1007/978-3-319-45669-0_12

Lewry, A. J. and Williamson, J. (1994). The setting of gypsum plaster Part I The hydration of calcium sulphate hemihydrate. The setting of gypsum plaster Part III. The effect of additives and impurities. *Journal of Materials Science*, 29, pp. 5279–5284, 6085–6090. https://doi.org610.1007/BF01171536

Yin, S. and Yang, L. (2020). α or β?-hemihydrates transformed from dihydrate calcium sulfate in a saltmediated glycerol–water solution. *Journal of Crystal Growth*, 5050, 125885. https://doi.org/10.1016/j.jcrysgro.2020.1258855050

Baohong, G., Qingqing, Y., Zhongbiao, B., Wenbin, L. and Liuchun, Y. (2010). Analysis of the relationship between particle size distribution of α-calcium sulfate hemihydrate and compressive strength of set plaster- Using grey model. *Powder Technology*, 200, pp. 136–143. https://doi.org/10.1016/j.powtec.2010.02.015

Pan, H., Deng-xing, L., Peng-sheng, W. and Zhi-ming, T (2019). Effect of Particle Size Ratios on the Physical and Chemical Properties of Surgical-Grade Calcium Sulfate Hemihydrate. *Orthopaedic Surgery Volume*, 12, pp. 1–7. https://doi.org/10.1111/os.12569

Singh, N. B and Middendorf, B. (2007). Calcium sulphate hemihydrate hydration leading to gypsum crystallization. *Progress in Crystal Growth and Characterization of Materials*, 53, pp. 57–77. https://doi.org/10.1016/j.pcrysgrow.2007.01.002

Sleiman, H., Perrot, A., and Amziane, S. (2010). A new look at the measurement of cementitious paste setting by Vicat test. *Cement and Concrete Research*, 40, pp. 681–686. https://doi.org/10.1016/j.cemconres.2009.12.001

Guan, Q., Sui, Y., Zhang, F., Yu, W., Bo, Y., Wang, P., Peng, W., and Jin, J. (2021). Preparation of α-calcium sulfate hemihydrate from industrial byproduct gypsum: a review. *Physicochemical Problems of Mineral Processing*, 57, pp. 168–181. https://doi.org/10.37190/ppmp/130795

Feldmann, T. and Demopoulos, G.P. (2012). Phase transformation kinetics of calcium sulfate phases in strong CaCl2-HCl solutions, Hydrometallurgy, 129, pp. 126–134. https://doi.org/10.1016/j.hydromet.2012.08.015

Fu, H., Jia, C., Chenb, Q., Caoa, X. and Zhang X. (2018) Effect of particle size on the transformation kinetics of flue gas desulfurization gypsum to α-calcium sulfate hemihydrate under hydrothermal conditions. *Particuology*, 1084, pp. 1–7. https://doi.org/10.1016/j.partic.2017.10.004

EN 13279-2:2014. *Gypsum binders and gypsum plasters - Part 2: Test methods.*

Responsible: Prof. dr. Péter Szűcs Vice-Rector
Published by the Miskolc University Press under leadership of Beáta Szabóné Kovács
Responsible for duplication: Erzsébet Pásztor
Technical editor: Csilla Gramantik
Proofreader: Zoltán Juhász
Number of copies printed:
Number of permission: MERT-2025- 178 -ME
HU ISSN 2063-6997